Study on Spin Transport Properties in Single-layer Graphene by Using Magnetization Dynamics

ZHENYAO

SEPTEMBER 2013

Study on Spin Transport Properties in Single-layer Graphene by Using Magnetization Dynamics

A dissertation submitted to

THE GRADUATE SCHOOL OF ENGINEERING SCIENCE

OSAKA UNIVERSITY

in partial fulfillment of the requirements for the degree of

DOCTOR OF PHILOSOPHY IN ENGINEERING

BY

ZHENYAO TANG

SEPTEMBER 2013

ABSTRACT OF THE DISSERATATION

Study on Spin Transport Properties in Single-layer Graphene by Using Magnetization Dynamics

by

ZHENYAO TANG

In this thesis, I summarized my study in doctoral research investigating spin transport in SLG by using a magnetization dynamics and the temperature dependence of spin Hall angle of Pd.

In the field of graphene spintronics, I investigated spin transport properties in SLG by using a magnetization dynamics method, which is totally different with electrical method. I successfully demonstrated the generation of spin current in SLG at room temperature by dynamical spin injection, which enables transferring spins from FM to NM free from electrical conductance mismatch. The spin coherence length of CVD-grown SLG was 1.36 μm and it agrees with previous reports. This achievement provides a method for discussing spin transport physics in SLG from a new viewpoint. Secondly, I proposed temperature dependence of spin coherence in SLG and in order to carry out this research, the investigation of temperature dependence of spin Hall angle of Pd is carried out. It decreased with increasing temperature from 0.02 at 130 K to 0.01 at 300 K. Finally, I explored the temperature dependence of spin coherence in SLG by dynamical spin injection method. The spin coherence of SLG was almost independent of temperature by using spin pumping method.

By these studies, a new platform for the investigation of spin coherence in SLG was successfully established. It provided more perspective for the investigation of spin transport and spin relaxation mechanism for future research in graphene.

Table of Contents

Chapter 1

Introduction

Abstract

In this section, I briefly introduce the history of spintronics. Then, graphene and the band structure of graphene are presented. Next, recent progress in graphene spintronics is reviewed. Finally, I point out the purpose of this study, and outline the contents of this thesis.

1.1 Spintronics

Spintronics is a research field utilizing both an electrical charge and the spin of the electron. The operation of spintronic devices is intimately related to magnetic phenomena and to the manipulation of spin-polarized currents. There are several concepts exploiting the electron spin for the development of novel devices, and spintronics is indeed an interesting field for preparing the next generation of micro- and nano-electronics [1-5].

Figure 1-1 shows the spin-dependent density of states (DOS) for non-magnetic and FM metals in the presence of a magnetic field. The asymmetry of the spin-dependent DOS allows FM to inject, detect and manipulate spins. Furthermore, spin is derived from quantum mechanics when combing it with special relativity, as Dirac did in the 1920's. One of the consequences is the requirement of an internal property that is known as spin in solving the Dirac equation. Because of its intrinsically quantum mechanical origin, it should be of little surprise that the electron spin has very unusual properties. For example, its value along any particular axis (the z-axis) can only take on two values that are called "spin up" and "spin down", $\left|\uparrow\right\rangle$ and $\left|\downarrow\right\rangle$, or $\left|m_s=\frac{1}{2}\right\rangle$ and $\left|m_s=-\frac{1}{2}\right\rangle$. It also obeys the Heisenberg uncertainty principle, where the three components of spin (S_x, S_y, S_z) cannot be measured simultaneously. Most importantly from the point of view of computing applications, the spin can be in a quantum superposition state, such as $A\left|\uparrow\right\rangle+B\left|\downarrow\right\rangle$. If we think about digital electronics as being built on bits that can have two states "0" or "1", we can think about spin as a "quantum bit" which can be in states $\left|\uparrow\right\rangle,\left|\downarrow\right\rangle$, or in a superposition state $A\left|\uparrow\right\rangle+B\left|\downarrow\right\rangle$, where $|A|^2$ is the probability of finding the spin in the $\left|\uparrow\right\rangle$ state and $|B|^2$ is the probability of finding the spin in the $\left|\downarrow\right\rangle$ state. The quantum bit, or "qubit", lies at the heart of a new type of computer, known as a quantum computer, which could in principle perform some tasks such as factorizing numbers or performing searches much more efficiently than

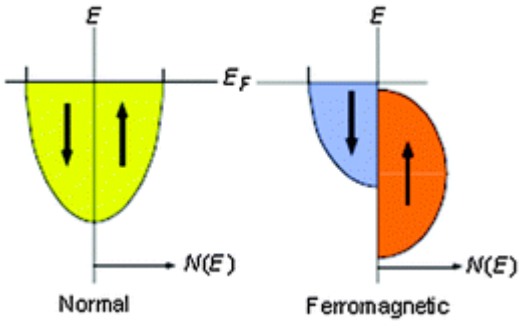

Figure 1-1. The DOS for a non-magnetic material and a ferromagnetic material.

normal digital computers. There are many schemes proposed for quantum computing (with most of them being

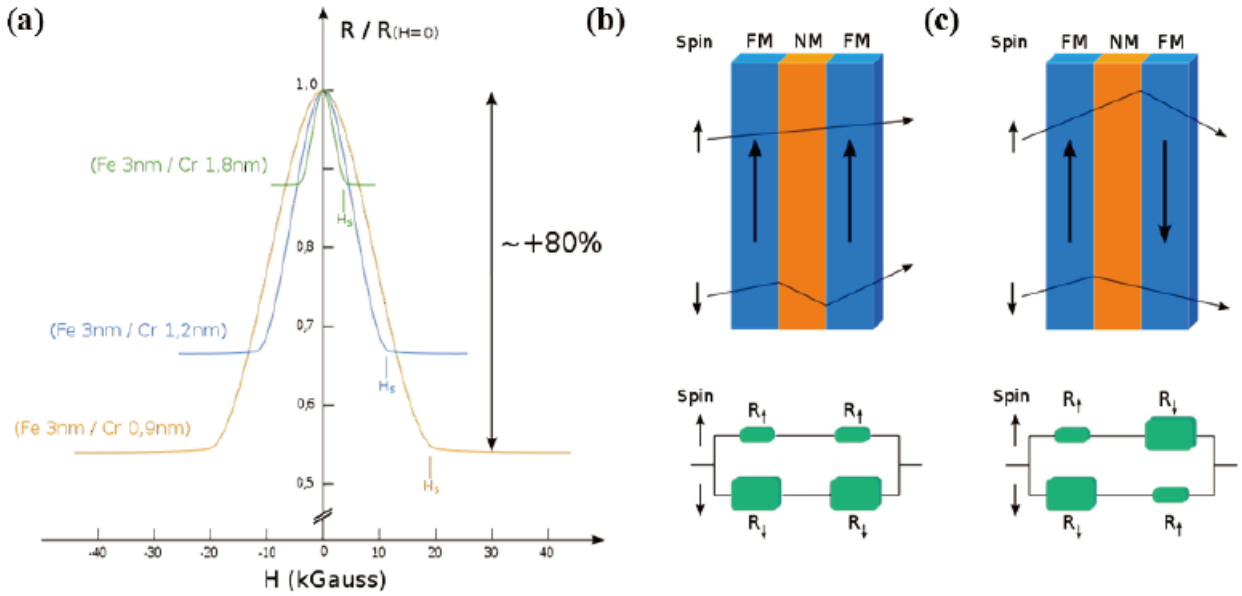

Figure 1-2. Giant magetoresistance effect observed in thin-film structures. From Ref. [7].

unrelated to electron spin) but there is a debate about whether a scalable quantum computer will ever be realized [6].

The history of spintronics can be traced back to the 1970s - 1980s. The giant magnetoresistance (GMR) effect in in multilayer FM thin metallic films was discovered independently by the Fert group and the Grünberg group [7, 8]. Tunneling experiments were successfully performed and explained by Moodera and Miyazaki [14, 15]. Figure 1-2(a) shows the GMR effect discovered in Fe/Cr multilayers by the group of Albert Fert. When the Cr layer is very thin (around 1nm), the RKKY (Ruderman and Kittel [11], Kasuya [12] and Yosida [13]) coupling

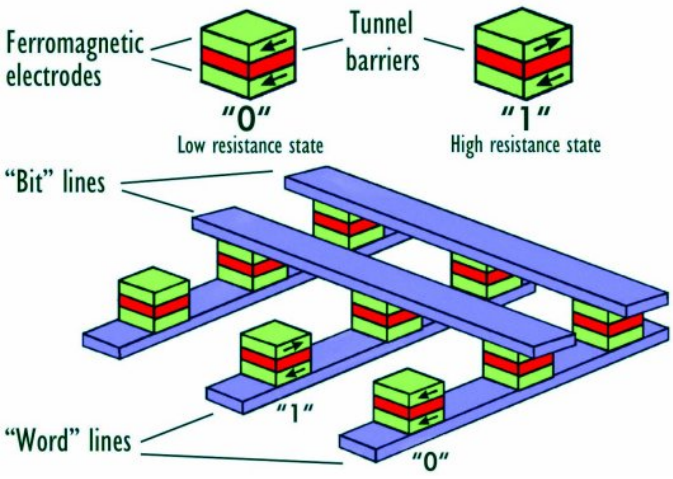

Figure 1-3. Principle of a MRAM device. This figure comes from internet.

between adjacent Fe layers becomes anti-ferromagnetic, making it energetically preferable to align in the anti-parallel configuration, which gives a high resistance (R_{AP}). A magnetic field is able to align the magnetization of Fe films so that they become parallel, which yields a low resistance (R_P). Figures 1-2 (b)(c) show a simple two-resistance model (spin-up channel and spin-down channel) to explain the GMR effect. When the two FM layers both exhibit spin up magnetization, the total resistance will be equal to a high resistance. On the other hand, if the two FM layers are anti-parallel to each other, the total resistance will be low. This effect will usually lead to two levels of resistance: a higher resistance of R_{AP} and a lower resistance of R_P. In 2007, Albert Fert and Peter Grünberg were awarded the Nobel Prize in Physics for their discovery of the GMR effects, which has been widely used in sensitive read-out heads for compact hard disks. "0" corresponds to a low resistance when the magnetizations are parallel, while "1" corresponds to a high resistance when the magnetizations are anti-parallel. The tunneling experiments lead to the discovery of tunneling magnetoresistance (TMR), which is the basis of a new type of non-volatile memory, called magnetoresistive random access memory (MRAM). TMR occurs in magnetic tunnel junctions (MTJ), which consist of two FM films separated by a thin insulator. Due to the spin polarized density of states, there will be a low resistance when the magnetizations are parallel ("0" in MRAM, Fig. 1-3) and a high resistance when the magnetizations are anti-parallel ("1" in MRAM, Fig. 1- 3). In the early 1990s, Miyazaki and Moodera independently observed room temperature TMR (~10%) across an amorphous aluminum oxide insulator [14, 15]. Later in 2004, much higher TMRs due to the spin-filtering effect based on wave function symmetry [16-18] were observed in MgO-based MTJs by the Parkin group and Yuasa group. Currently, the record for room temperature TMR is 600% in Fe/Co/MgO/Co/Fe MTJs grown by molecular

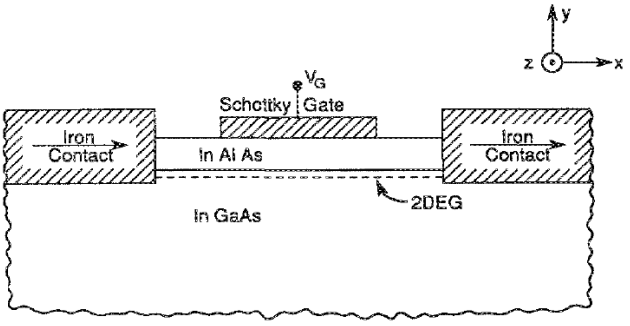

Figure 1-4. A proposed electron wave analog of the electro-optic modulator. From Ref. [20]

beam epitaxy [19].

Whereas the above history of spintronics is that of metallic spintronics, spintronics using inorganic semiconductors (GaAs, Si and so on) has also been vigorously investigated. Among these inorganic semiconductors, GaAs could be used to realize spin transistors as proposed by Das and Datta [20], as shown in Fig. 1-4, where injected spins into GaAs are rotated by an applied gate voltage because of the existence of a strong spin–orbit interaction. On the contrary, Si is a comparably light element and has lattice inversion symmetry, and therefore spin MOS field effect transistors (FETs) can to be realized. Currently, several research groups are intensively investigating spin injection and spin transport [21]. This field is known as the second pillar of spintronics, namely semiconductor spintronics. Since 1999, a third pillar of spintronics has been attracting much attention from spintronics and molecular electronics researchers; this field is, molecular spintronics. A molecule exhibits a comparably smaller spin–orbit interaction. A spin–orbit interaction is known as the interaction which induces loss of spin coherence; thus, a material with a small spin–orbit interaction is needed to realize quantum computation systems and the so-called Sugahara–Tanaka type spin MOSFETs [22]. Currently, nano-carbonaceous molecules (graphene, carbon nanotube and fullerene) and organic molecules are intensively investigated for further progress in this research field, and a number important and attractive results have been obtained [23, 24].

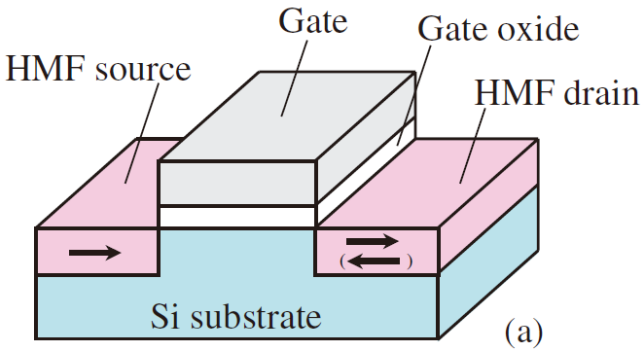

Figure 1-5. Schematic device structure of a spin MOSFET using half metallic-ferromagnet (HMF) contacts for the source and drain. From Ref. [22].

Organic semiconductors are interesting to the spintronics community due to long spin life times, chemical flexibility and optoelectronic properties. In 2004, Xiong et al studied a spin valve based on Alq3 (8-hydroxy-quinoline aluminium) with LSMO and Co as the FM electrodes (see Fig. 1-6) [25]. In 2007 and

2008, Santos et al and Dediu et al independently achieved room temperature spin transport by inserting a thin Al_2O_3 between Co and Alq_3 [26, 27]. In 2009, Sun et al used a large Co nanoparticle between Co electrodes and Alq_3 to block the diffusion of Co growth inside Alq_3 in order to form a conductance path, and observed large MR [28].

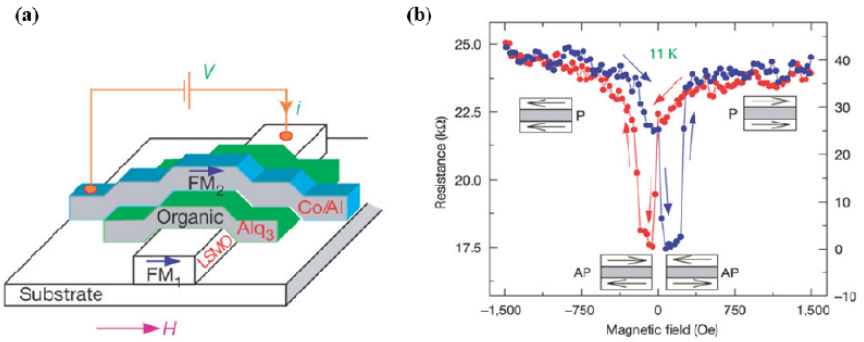

Figure 1-6. Organic semiconductor spin valves. (a) Alq3 device geometry. One FM electrode is LSMO, and the other FM electrode is Co. (b) MR loop measured at 11 K with a negative MR of 40%. From Ref. [25].

Raman et al studied the effect of molecular ordering on spin injection in rubrene, while Yoo et al observed giant MR in the LSMO/LAO/rubrene/Fe junction [29, 30]. In 2010, Yoo et al studied the spin valve effect on rubrene with an organic-based magnetic semiconductor named vanadium [31]. Carbon based materials (carbon nanotubes, C_{60}, graphene) have attracted considerable interest because they are expected to have long spin lifetimes due to their intrinsically low spin orbit couplings and hyperfine couplings [32, 33]. Carbon nanotubes (CNTs) spin valve devices were first reported by Tsukagoshi and his co-workers (see Fig. 1-7) in 1999 [34]. After this study, several groups reported MR studied on single wall and multi wall CNTs [35, 36]. In 2006-2007, two important milestones in CNT spintronics were achieved. The first one was the

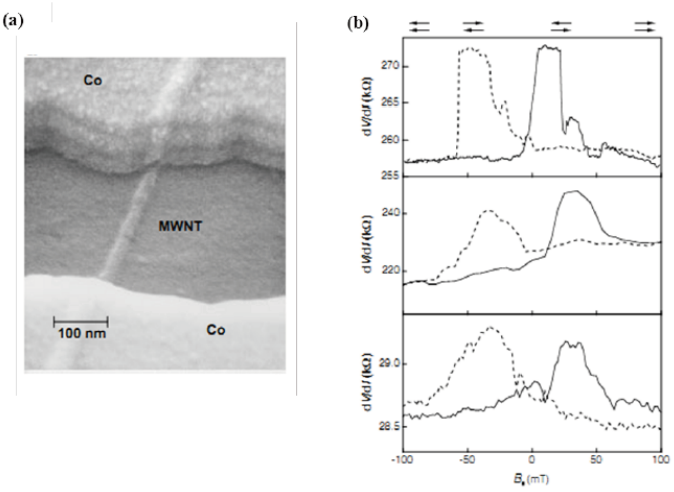

Figure 1-7. Electrical spin transport in carbon nanotube spin valve. (a) Carbon nanotube spin valve geometry. MWNT is connected to two FM Co leads. (b) Local MR measurements for 3 devices. From Tsukagoshi et al, [34].

detection of a pure spin current using the nonlocal technique of Tombros et al [37]. They studied the spin transport in a single wall nanotube using both local and nonlocal techniques; their results showed that the local MR was about 30 times larger than the nonlocal MR. This was contrary to the theoretical predictions (local MR is equal to 2 times of nonlocal MR) and pointed out that nonlocal MR was more reliable than the local MR to prove spin injection. The other important milestone was the observation of very large MR ratio in CNT spin valves using half metallic LSMO electrodes [38].

Compared to carbon nanotubes, graphene, a single atomic layer of graphitic carbon, has drawn more attention in spintronics due to its tunable carrier concentration and conductivity, ultra high mobility, and sensitive surfaces, etc. In the next subsection, I will introduce the properties of graphene and the research carried on graphene spintronics so far.

1.2 Graphene

Andre Geim and Konstantin Novoselov were awarded the 2010 Nobel Prize for their breakthrough experiments with graphene [39, 40]. Currently, several methods to make graphene have been developed. The conventional called “mechanical exfoliation” (by scotch tape), was invented by the Geim group [39]. Additionally, other methods such as epitaxial growth by SiC decomposition at ultrahigh temperatures to fabricate wafer-size graphene [41], and growing graphene by chemical vaper deposition (CVD) on metal substrates, such as Ni, Ir, etc [42], are also available for fabricating large-sized pieces of graphene. However, the quality of graphene from this method is not good due to residue of the reduction functional groups. Recently, there has been a major breakthrough made by the Ruoff group, which succeeded in growing a large piece of high quality single layer graphene on copper using the CVD method [43]. The graphene samples used in this thesis were provided by the Ago group at Kyushu Univ. They can synthesize large-scale, high quality single-layer graphene by CVD method [44].

1.2.1 Band structure of graphene

Graphene is a single sheet made up of carbon atoms arranged in the well known honeycomb structure. The lattice of graphene is shown in Fig. 1-8. Carbon has four valence electrons, of which three are used for the sp^2 bonds. Researchers refer to this band as the π band. There are two such electrons per unit-cell. Hence, there will be two π -bands (the π and π^* bands) as shown in Fig. 1-8. The even number of electrons per unit-cell makes this example very interesting because we do not know a priori whether the material will be metallic or semiconducting. The first tight-binding description of graphene was given by Wallace in 1947 [45]. Carbon atom ($^6C=1s^22s^22p^2$, group IV) has four unpaired electrons, 2*s*, $2p_x$, $2p_y$ and $2p_z$ orbitals, which can mix with each other. Although they consist of the same atomic ingredient, namely carbon, the 3D graphite and diamond crystals are physically different. Graphite, as described above, is a very soft material due to its layered structure, whereas diamond is one of the hardest natural materials because all bonds are covalent σ bonds. The fact that all four valence electrons in the outer atomic shell are used in the formation of the σ bonds is also the reason for diamond being an insulator with a large band gap of 5.47 eV. In contrast to insulating diamond, the electrons in the weaker π bonds in graphite are delocalized, and thus, have good electronic conduction properties.

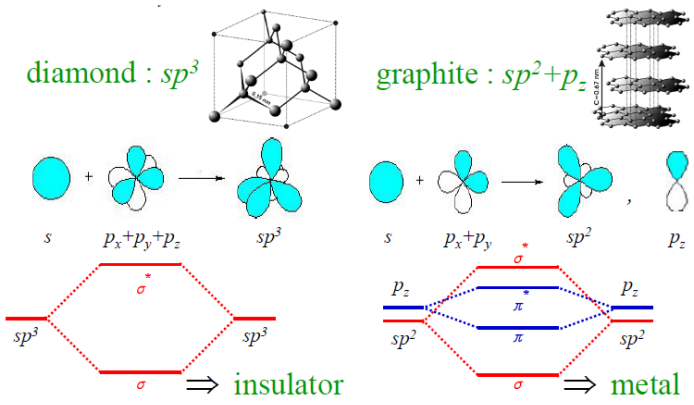

Figure 1-8. Hybrization of carbon

The band structure of graphene can be calculated by tight-binding approximation. As mentioned above, the carbon atoms in graphene

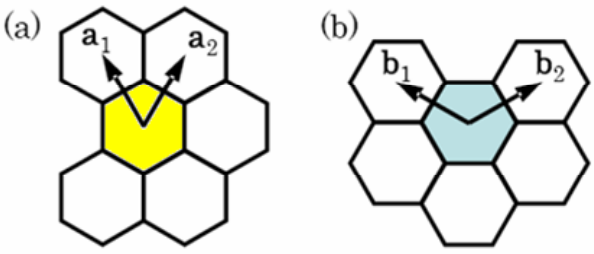

Figure 1-9. (a) vectors for real space and (b) reciprocal spaces vectors.

condense in a honeycomb lattice due to their sp^2 hybridization. The honeycomb lattice is not a Bravais lattice because two neighboring sites are not equivalent. The lattice vectors of graphene are defined to be a_1 and a_2, and the reciprocal lattice vectors, are b_1 and b_2, as shown in Fig. 1-9. The relation is expressed by,

$$a_i \cdot b_j = 2\pi\delta_{ij}, \quad (1\text{-}1)$$

where the Kronecker delta $\delta ij = \begin{cases} 0\ (i \neq j), \\ 1\ (i = j). \end{cases}$ (1-2)

For the convenience of definition, we define the vectors on 2-dimensional space,

$$\begin{aligned} &a_1 = a(-\frac{1}{2}, \frac{\sqrt{3}}{2}), a_2 = a(\frac{1}{2}, \frac{\sqrt{3}}{2}), \\ &b_1 = \frac{2\pi}{a}(-\frac{\sqrt{3}}{2}, \frac{1}{2}), b_2 = \frac{2\pi}{a}(\frac{\sqrt{3}}{2}, \frac{1}{2}). \end{aligned} \quad (1\text{-}3)$$

From the symmetry of the benzene ring of graphene, there are two different carbon atoms, called site A and B (see Fig. 1-10). We use the tight-binding approximation method to calculate the energy band of graphene. First, in a translational symmetric crystal, the wave function of an atomic orbital is a translation which satisfies the following translational operation $\hat{R}$,

$$\hat{R}\phi(r) \equiv \phi(r + R) = e^{ik \cdot R}\phi(r). \quad \text{(Bloch Theorem)} \quad (1\text{-}4)$$

The wave function of tight-binding uses the approximation of LCAO (Linear Combination of Atomic Orbitals). It is important to remember that the LCAO approximation assumes that the atomic wave-functions are well localized at the position of the atom ($R = n\vec{a_1} + m\vec{a_2}$). The electrical transport in graphene is performed by π electrons, and so we do not consider the σ electrons from now on. The tight-binding wave functions on the Bloch basis can be expressed as,

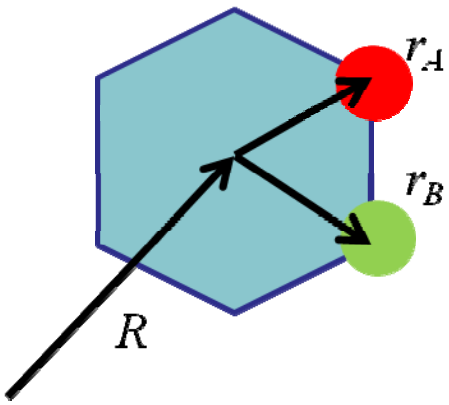

Figure 1-10. A site and B site consist the atoms in one unit cell of graphene.

$$\phi_{Ak} = \frac{1}{\sqrt{N}} \sum_R \phi_{2Z}(r - r_A - R)\exp(ikR),$$
$$\phi_{Bk} = \frac{1}{\sqrt{N}} \sum_R \phi_{2Z}(r - r_B - R)\exp(ikR), \qquad (1\text{-}5)$$

($k \in$ first Brillouin zone, R: all Brillouin Points in N^{th} lattice , $2z$: $2p_z$ orbital)

where N is the number of cells for normalization. The wave function of the $2p_z$ orbital can be expressed by the relative coordinate in a unit cell. The energy, transfer integral and overlap integral of $2p_z$ orbitals of site A and B within the same unit cell are expressed by,

$$\varepsilon = \int dr\phi_{2p}^*(r - r_A)H\phi_{2p}(r - r_A), \quad 1 = \int dr\phi_{2p}^*(r - r_A)\phi_{2p}(r - r_A),$$
$$t = \int dr\phi_{2p}^*(r - r_A)H\phi_{2p}(r - r_B), \quad s = \int dr\phi_{2p}^*(r - r_A)\phi_{2p}(r - r_B). \qquad (1\text{-}6)$$

It is possible to use the Bloch functions for calculating the elements of the matrix and overlapping the transfer matrix. The following equations are determined by,

$$H_{AA'}^{(k,k')} = \left\langle \phi_A(k,r) \middle| H \middle| \phi_{A'}(k',r') \right\rangle, \quad S_{AA'}^{(k,k')} = \left\langle \phi_A(k,r) \middle| \phi_{A'}(k',r') \right\rangle,$$
$$H_{BB'}^{(k,k')} = \left\langle \phi_B(k,r) \middle| H \middle| \phi_{B'}(k',r') \right\rangle, \quad S_{BB'}^{(k,k')} = \left\langle \phi_B(k,r) \middle| \phi_{B'}(k',r') \right\rangle,$$
$$H_{AB'}^{(k,k')} = \left\langle \phi_A(k,r) \middle| H \middle| \phi_{B'}(k',r') \right\rangle, \quad S_{AB'}^{(k,k')} = \left\langle \phi_A(k,r) \middle| \phi_{B'}(k',r') \right\rangle,$$
$$H_{BA'}^{(k,k')} = \left\langle \phi_B(k,r) \middle| H \middle| \phi_{A'}(k',r') \right\rangle, \quad S_{BA'}^{(k,k')} = \left\langle \phi_B(k,r) \middle| \phi_{A'}(k',r') \right\rangle. \qquad (1\text{-}7)$$

Meanwhile, $r' = r - r_{AorB} - R'$ expresses the relative coordinate in the unit cell which is different from the position of $\boldsymbol{R}$.

Now, we consider the effect from the nearest three atoms to obtain the energy dispersion relation by the Bloch functions. When we think about a graphene sheet as shown in Fig. 1-11, the carbon atoms located at the A site are surrounded by exactly three B atoms. On the other hand, a carbon atom of the B site is always surrounded by three A atoms.

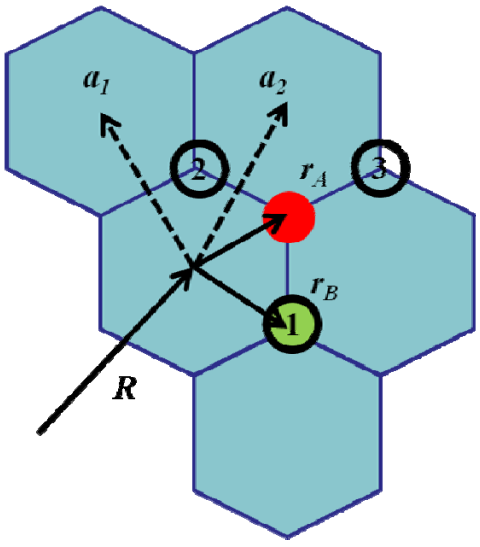

Figure 1-11. A site and B site in graphene and the nearest neighbors to A site.

Based on this consideration, H_{AA}, H_{BB}, S_{AA}, S_{BB} are the integral in the same atom, H_{AB}, $H_{BA}(=H_{BA}^{*})$, S_{AB}, $S_{BA}(=S_{BA}^{*})$ are the interaction integral with the nearest three atoms.

First, to derive H_{AA}, H_{BB}, S_{AA}, S_{BB}, we can consider the integral for the same atom, in other words, it is enough to deduce them in one unit cell. So, the transfer matrixes are,

$$\begin{aligned}
H_{AA}^{(k,k')} &= \int dr \frac{1}{\sqrt{N}} \sum_{R}^{N} \phi_{2p}^{*}(r-r_A) \exp[-ik\cdot R] H \frac{1}{\sqrt{N}} \sum_{R}^{N} \phi_{2p}(r-r_A) \exp[-ik'\cdot R] \\
&= \varepsilon \frac{1}{N} \sum_{R}^{N} \exp[-i(k-k')\cdot R] \\
&= \varepsilon \delta_{kk'}, \\
H_{BB}^{(k,k')} &= \int dr \frac{1}{\sqrt{N}} \sum_{R}^{N} \phi_{2p}^{*}(r-r_B) \exp[-ik\cdot R] H \frac{1}{\sqrt{N}} \sum_{R}^{N} \phi_{2p}(r-r_B) \exp[-ik'\cdot R] \\
&= \varepsilon \frac{1}{N} \sum_{R}^{N} \exp[-i(k-k')\cdot R] \\
&= \varepsilon \delta_{kk'}, \\
S_{AA}^{(k,k')} &= \int dr \frac{1}{\sqrt{N}} \sum_{R}^{N} \phi_{2p}^{*}(r-r_A) \exp[-ik\cdot R] \frac{1}{\sqrt{N}} \sum_{R}^{N} \phi_{2p}(r-r_A) \exp[-ik'\cdot R] \\
&= \frac{1}{N} \sum_{R}^{N} \exp[-i(k-k')\cdot R] \\
&= \delta_{kk'}, \\
S_{BB}^{(k,k')} &= \int dr \frac{1}{\sqrt{N}} \sum_{R}^{N} \phi_{2p}^{*}(r-r_B) \exp[-ik\cdot R] \frac{1}{\sqrt{N}} \sum_{R}^{N} \phi_{2p}(r-r_B) \exp[-ik'\cdot R] \\
&= \frac{1}{N} \sum_{R}^{N} \exp[-i(k-k')\cdot R] \\
&= \delta_{kk'}.
\end{aligned} \tag{1-8}$$

Then, to consider H_{AB}, $H_{BA}(=H_{BA}^{*})$, S_{AB}, $S_{BA}(=S_{BA}^{*})$, it is necessary to consider the effects from the three nearest atoms,

i) $R'=R$

$$\begin{aligned}
H_{AB}^{(k,k')} &= \int dr \frac{1}{\sqrt{N}} \sum_{R}^{N} \phi_{2p}^{*}(r-r_A) \exp[-ik\cdot R] H \frac{1}{\sqrt{N}} \sum_{R}^{N} \phi_{2p}(r-r_B) \exp[-ik'\cdot R] \\
&= t \frac{1}{N} \sum_{R}^{N} \exp[-i(k-k')\cdot R] \\
&= t \delta_{kk'},
\end{aligned}$$

$$S_{AB}^{(k,k')} = \int dr \frac{1}{\sqrt{N}} \sum_R^N \phi_{2p}^*(r - r_A) \exp[-ik \cdot R] \frac{1}{\sqrt{N}} \sum_R^N \phi_{2p}(r - r_B) \exp[-ik' \cdot R]$$
$$= s \frac{1}{N} \sum_R^N \exp[-i(k - k') \cdot R] \qquad (1\text{-}9)$$
$$= s\delta_{kk'}.$$

ii) $R'=R+a_1$

$$H_{AB'}^{(k,k')} = \int dr \frac{1}{\sqrt{N}} \sum_R^N \phi_{2p}^*(r - r_A) \exp[-ik \cdot R] H \frac{1}{\sqrt{N}} \sum_R^N \phi_{2p}(r - r_B) \exp[-ik' \cdot (R + a_1)]$$
$$= t \frac{1}{N} \sum_R^N \exp[-i(k - k') \cdot R + ik' \cdot a_1]$$
$$= t\delta_{kk'} \exp[ik' \cdot a_1],$$

$$S_{AB'}^{(k,k')} = \int dr \frac{1}{\sqrt{N}} \sum_R^N \phi_{2p}^*(r - r_A) \exp[-ik \cdot R] \frac{1}{\sqrt{N}} \sum_R^N \phi_{2p}(r - r_B) \exp[ik' \cdot (R + a_1)]$$
$$= s \frac{1}{N} \sum_R^N \exp[-i(k - k') \cdot R + ik' \cdot a_1] \qquad (1\text{-}10)$$
$$= s\delta_{kk'} \exp[ik' \cdot a_1].$$

iii) $R'=R+a_2$

$$H_{AB'}^{(k,k')} = \int dr \frac{1}{\sqrt{N}} \sum_R^N \phi_{2p}^*(r - r_A) \exp[-ik \cdot R] H \frac{1}{\sqrt{N}} \sum_R^N \phi_{2p}(r - r_B) \exp[-ik' \cdot (R + a_2)]$$
$$= t \frac{1}{N} \sum_R^N \exp[-i(k - k') \cdot R + ik' \cdot a_2]$$
$$= t\delta_{kk'} \exp[ik' \cdot a_2],$$

$$S_{AB'}^{(k,k')} = \int dr \frac{1}{\sqrt{N}} \sum_R^N \phi_{2p}^*(r - r_A) \exp[-ik \cdot R] \frac{1}{\sqrt{N}} \sum_R^N \phi_{2p}(r - r_B) \exp[ik' \cdot (R + a_2)]$$
$$= s \frac{1}{N} \sum_R^N \exp[-i(k - k') \cdot R + ik' \cdot a_2] \qquad (1\text{-}11)$$
$$= s\delta_{kk'} \exp[ik' \cdot a_2].$$

Thus, all parts of the matrix have been solved by the calculation above, and the term $\delta_{kk'}$ is included in every part. In order to observe the values of $\delta_{kk'}$, $k=k'$ is a necessary condition. So,

$$H_{AA} = H_{BB} = \varepsilon, \quad S_{AA} = S_{BB} = 1,$$

$$H_{AB} = t(1 + \exp[ik \cdot a_1] + \exp[ik \cdot a_2])$$
$$= tf(k),$$

$$H_{BA} = H_{AB}^* = tf^*(k),$$

$$
\begin{aligned}
S_{AB} &= s(1+\exp[ik\cdot a_1]+\exp[ik\cdot a_2]) \\
&= sf(k),
\end{aligned}
$$

$$
S_{BA} = S_{AB}^{*} = sf^{*}(k), \tag{1-12}
$$

where the sum of the phase factor is,

$$
f(k) \equiv 1+\exp[ik\cdot a_1]+\exp[ik\cdot a_2].
$$

Here, the transfer matrix and overlap matrix are expressed as,

$$
H = \begin{pmatrix} \varepsilon & tf(k) \\ tf^{*}(k) & \varepsilon \end{pmatrix},\ S = \begin{pmatrix} 1 & sf(k) \\ sf^{*}(k) & 1 \end{pmatrix}. \tag{1-13}
$$

Since the tight-binding wave function of Schrödinger equation is,

$$
H\Psi(r) = E\Psi(r), \tag{1-14}
$$

the expectation value is written as,

$$
\begin{aligned}
E &= \frac{\langle \Psi | H | \Psi \rangle}{\langle \Psi | \Psi \rangle} \\
&= \frac{\sum_{j,j'=A,B} C_j^{*} C_{j'} \langle \phi_j | H | \phi_{j'} \rangle}{\sum_{j,j'=A,B} C_j^{*} C_{j'} \langle \phi_j | \phi_{j'} \rangle} \\
&= \frac{\sum_{j,j'=A,B} C_j^{*} C_{j'} H_{jj'}}{\sum_{j,j'=A,B} C_j^{*} C_{j'} S_{jj'}}.
\end{aligned} \tag{1-15}
$$

Then, by the calculus of variations, we find the coefficient *C* which makes the smallest energy expectation value,

$$\frac{\partial E}{\partial C_j^*}=0$$

$$\Leftrightarrow \frac{\sum_{j'=A,B} C_{j'}H_{jj'}}{\sum_{j,j'=A,B} C_j^*C_{j'}S_{jj'}} - \frac{\sum_{j,j'=A,B} C_j^*C_{j'}H_{jj'} \times \sum_{j'=A,B} C_{j'}S_{jj'}}{(\sum_{j,j'=A,B} C_j^*C_{j'}S_{jj'})^2}=0 \qquad (1\text{-}16)$$

$$\Leftrightarrow \sum_{j'=A,B} C_{j'}H_{jj'} = \sum_{j'=A,B} C_{j'}S_{jj'} \times \frac{\sum_{j,j'=A,B} C_j^*C_{j'}H_{jj'}}{\sum_{j,j'=A,B} C_j^*C_{j'}S_{jj'}}$$

$$\Leftrightarrow \sum_{j'=A,B} C_{j'}H_{jj'} = E\sum_{j'=A,B} C_{j'}S_{jj'}.$$

Here, we define the column vector,

$$\mathbf{C}=\begin{pmatrix} C_A(k) \\ C_B(k) \end{pmatrix}, \qquad (1\text{-}17)$$

and the above equation becomes,

$$H\mathbf{C}=ES\mathbf{C}$$

$$\Leftrightarrow \begin{pmatrix} \varepsilon & tf(k) \\ tf^*(k) & \varepsilon \end{pmatrix}\begin{pmatrix} C_A(k) \\ C_B(k) \end{pmatrix} = E\begin{pmatrix} 1 & sf(k) \\ sf^*(k) & 1 \end{pmatrix}\begin{pmatrix} C_A(k) \\ C_B(k) \end{pmatrix}, \qquad (1\text{-}18)$$

which describes the Hamiltonian of 2-D graphene with an infinite size. It is necessary to satisfy the following conditions to make the matrix coefficient ***C*** be different from zero:

$$\det(H-ES)=0$$

$$\Leftrightarrow \begin{vmatrix} \varepsilon-E & (t-Es)f(k) \\ (t-Es)f^*(k) & \varepsilon-E \end{vmatrix}=0 \qquad (1\text{-}19)$$

$$\Leftrightarrow (\varepsilon-E)^2-(t-Es)^2\left|f(k)\right|^2=0.$$

The expectation value of energy is shown as,

$$E=\begin{cases} \varepsilon+t\sqrt{f(k)f^*(k)}, \\ \varepsilon-t\sqrt{f(k)f^*(k)}. \end{cases} \qquad (1\text{-}20)$$

From this result, we have the energy on the $2p_z$ orbital and transfer integral, so the dispersion of energy on k space can be observed. The energy dispersion in the first Brillouin zone of graphene is shown in Fig. 1-12 by using computer programming and set $\varepsilon=0$, t=-3.033eV, $s=0.129$ based on the report

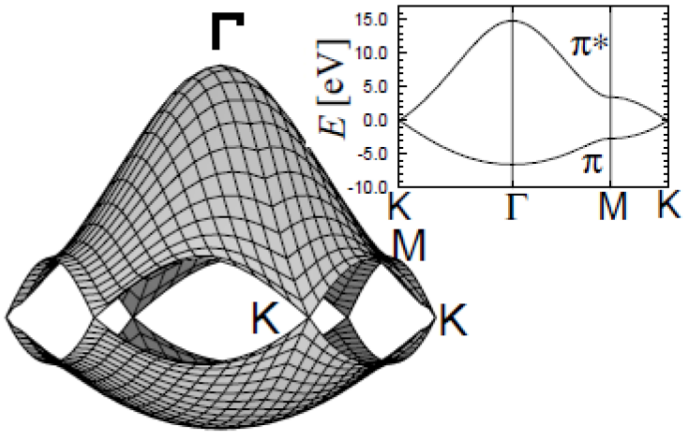

Figure 1-12. π and π* band in the first Brillouin zone of graphene, two bands connect at K-point.

of Saitoh et al [46]. The π & π* band and the dispersion energy of the first Brillouin zone connected at the K point. There are two carbon atoms in a unit cell of graphene and each atom provides one electron according to tight-binding approximation. The π band occupies two electrons at absolute zero in temperature and the electron transition occurs at finite temperature on π* band around the K point. Therefore, it is necessary to focus on the behavior of electrons in the vicinity of the K point to understand the electron transport properties in graphene. The energy band around K point is derived as follows.

We expand this Hamiltonian around K point with long wavelength approximation. The coordinates of K point can be expressed by reciprocal lattice vectors as,

$$K = \frac{1}{3}b_1 + \frac{2}{3}b_2. \qquad (1\text{-}21)$$

If we consider the wave vector near K point, $k = K + \Delta k$, then,

$$\begin{aligned} f(k) &\approx f(K) + \frac{\partial f(k)}{\partial k}\Big|_{k=K} \cdot \Delta k \\ &= f(K) + (i\Delta k \cdot a_1)\exp[iK \cdot a_1] + (i\Delta k \cdot a_2)\exp[iK \cdot a_2] \\ &= 1 + \exp[iK \cdot a_1] + \exp[iK \cdot a_2] + (i\Delta k \cdot a_1)\exp[iK \cdot a_1] + (i\Delta k \cdot a_2)\exp[iK \cdot a_2] \\ &= 1 + (1 + i\Delta k \cdot a_1)\exp[iK \cdot a_1] + (1 + i\Delta k \cdot a_2)\exp[iK \cdot a_2]. \end{aligned} \qquad (1\text{-}22)$$

We can calculate the inner product of the vectors as follows:

$$\begin{aligned} K \cdot a_1 &= (\frac{1}{3}b_1 + \frac{2}{3}b_2) \cdot a_1 = \frac{2}{3}\pi, \\ K \cdot a_2 &= (\frac{1}{3}b_1 + \frac{2}{3}b_2) \cdot a_2 = \frac{4}{3}\pi. \end{aligned} \qquad (1\text{-}23)$$

When we substitute these values into the above formula, we get,

$$\begin{aligned} f(k) &\approx 1 + (1 + i\Delta k \cdot a_1)\exp[i\frac{2}{3}\pi] + (1 + i\Delta k \cdot a_2)\exp[i\frac{4}{3}\pi] \\ &= 1 + (1 + i\Delta k \cdot a_1)(-\frac{1}{2} + i\frac{\sqrt{3}}{2}) + (1 + i\Delta k \cdot a_2)(-\frac{1}{2} - i\frac{\sqrt{3}}{2}) \\ &= (-\frac{\sqrt{3}}{2} - i\frac{1}{2})\Delta k \cdot a_1 + (\frac{\sqrt{3}}{2} - i\frac{1}{2})\Delta k \cdot a_2. \end{aligned} \qquad (1\text{-}24)$$

Here, $\Delta k = (k_x, k_y)$, so,

$$
\begin{aligned}
f(k) &\approx (-\frac{\sqrt{3}}{2} - i\frac{1}{2})(k_x, k_y)\cdot a(-\frac{1}{2}, \frac{\sqrt{3}}{2}) + (\frac{\sqrt{3}}{2} - i\frac{1}{2})(k_x, k_y)\cdot a(\frac{1}{2}, \frac{\sqrt{3}}{2}) \\
&= a(-\frac{\sqrt{3}}{2} - i\frac{1}{2})(-\frac{1}{2}k_x + \frac{\sqrt{3}}{2}k_y) + a(\frac{\sqrt{3}}{2} - i\frac{1}{2})(\frac{1}{2}k_x + \frac{\sqrt{3}}{2}k_y) \qquad \text{(1-25)} \\
&= \frac{\sqrt{3}}{2}a(k_x - ik_y),
\end{aligned}
$$

which describes H_{AB}. We can also observe,

$$H_{BA} = \frac{3}{2}a(k_x + ik_y)\,. \qquad \text{(1-26)}$$

So the Hamiltonian of graphene around K-point,

$$
\begin{aligned}
H &\sim \begin{pmatrix} 0 & k_x - ik_y \\ k_x + ik_y & 0 \end{pmatrix}, \\
H &= \hbar v_F \begin{pmatrix} 0 & k_x - ik_y \\ k_x + ik_y & 0 \end{pmatrix}.
\end{aligned} \qquad \text{(1-27)}
$$

Then, we consider the zeroth approximation ($2p_z$ wave functions are totally localized in carbon atoms), so,

$$S = \begin{pmatrix} 1 & 0 \\ 0 & 1 \end{pmatrix}. \qquad \text{(1-28)}$$

The eigen value of the energy around the K-point,

$$
\begin{aligned}
&\det(H - ES) = 0 \\
&\Leftrightarrow \begin{vmatrix} -E & \hbar v_F(k_x - ik_y) \\ \hbar v_F(k_x + ik_y) & -E \end{vmatrix} = 0 \\
&\Rightarrow E = \pm\hbar v_F\sqrt{k_x{}^2 + k_y{}^2} \\
&\qquad = \pm\hbar v_F |k|.
\end{aligned} \qquad \text{(1-29)}
$$

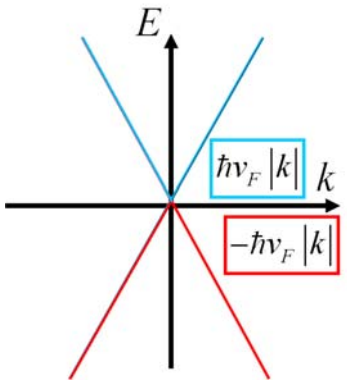

Figure 1-13. Band structure of graphene around K-point.

Therefore, the $2p_z$ orbital band structure of graphene is linear around the K-point as shown in Fig. 1-13. The calculations above show the band structure of the ideal state of a graphene sheet. In fact, the size of graphene is finite, and the defects and the absorption of impurities also influence the shape of band structure of graphene.

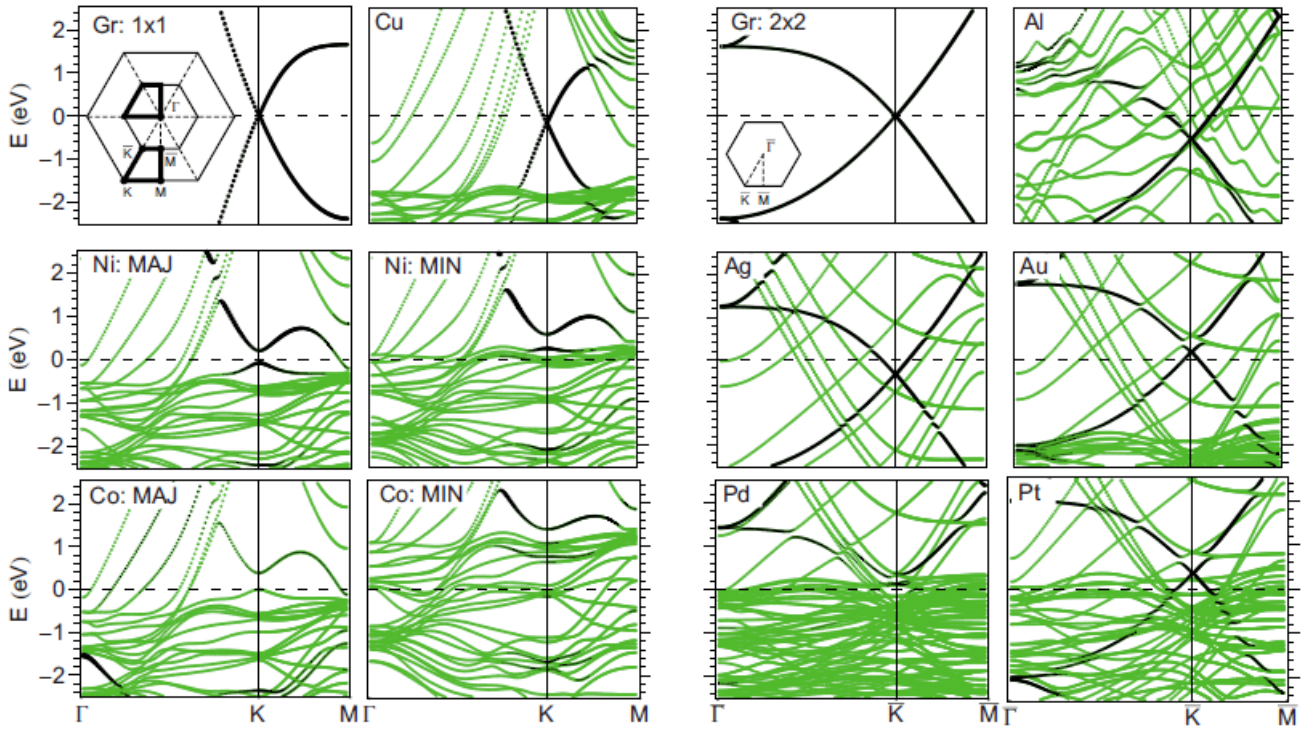

Figure 1-14. Band structures of graphene adsorbed upon Au, Pt, Cu, Ag, Al, Pd, Ni, and Co (111) substrates. The Fermi level is at zero energy. From Ref. [48].

The energy dispersion by first-principles calculations when a variety of metal atoms are attached to graphene has been reported (see Fig. 1-14) [47, 48]. The left figures show how the graphene band structure (black lines) is affected by metal atoms attached onto graphene by chemical adsorption. A strong reaction was applied to graphene and therefore the band structure of graphene changed drastically. The right figures show the weak metal-graphene binding between metal and graphene, where the original band structures of graphene are still recognizable.

1.2.2 Raman spectroscopy of graphene [49, 50]

The number of graphene layers is important for the research of graphene, since the properties of single-layer graphene and bilyaer graphene (BLG) are quite different. Nevertheless, it is difficult to distinguish between single-layer and bilayer graphene. Atomic force microscopy (AFM) is one method to identify single and multiple layers, but it has a low throughput. Moreover, due to the chemical contrast between graphene and the substrate (which results in an apparent chemical thickness of 0.5–1 nm, much bigger than that expected from the interlayer graphite spacing [39, 51]), in practice, it is only possible to distinguish between one and two layers by AFM if films contain folds or wrinkles [39, 51].

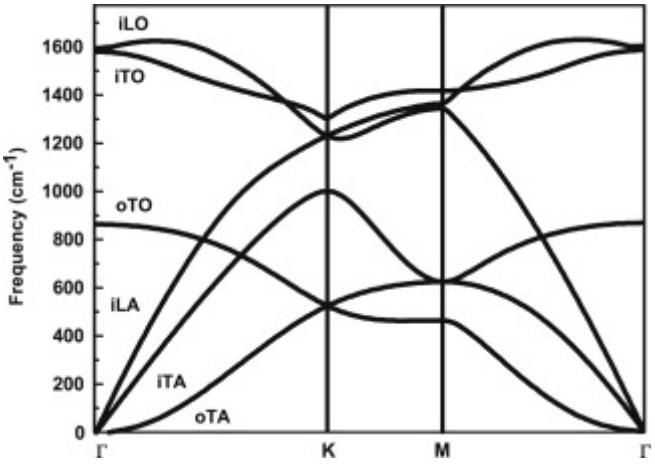

Figure 1-15. Calculated phonon dispersion relation of graphene showing the iLO, iTO, oTO, iLA, iTA and oTA phonon branches. From Ref. [52].

In principle, when the final vibrational state of the molecule is more energetic than the initial state, then the emitted photon will be shifted to a lower frequency in order for the total energy of the system to remain balanced. This shift in frequency is designated as a Stokes shift. If the final vibrational state is less energetic than the initial state, then the emitted photon will be shifted to a higher frequency, and this is designated as an anti-Stokes shift. Raman scattering is an example of inelastic scattering because of the energy transfer between the photons and the molecules during their interaction.

An understanding of the phonon dispersion in graphene is essential to interpreting the Raman spectra of graphene. Since the unit cell of monolayer graphene contains two carbon atoms, A and B, there are six phonon dispersion bands (see Fig. 1-15), in which three are acoustic branches (A) and the other three are optic (O)

phonon branches. For one acoustic branch (A) and one optic (O) phonon branch, the atomic vibrations are perpendicular to the graphene plane, and they correspond to the out-of-plane (o) phonon modes. For two acoustic and two optic phonon branches, the vibrations are in-plane (i). Traditionally, the directions of the vibrations are considered with respect to the direction of the nearest carbon–carbon atoms and, therefore, the phonon modes are classified as longitudinal (L) or transverse (T) according to vibrations parallel with or perpendicular to, respectively, the A–B carbon–carbon directions. Therefore, the six phonon dispersion curves are assigned to the LO, iTO, oTO, LA, iTA, and oTA phonon modes. (see Fig. 1-15) [52]

The most prominent features in the Raman spectra of monolayer graphene are the so-called G band appearing at 1582 cm^{-1} (graphite), and the G′ band at about 2700 cm^{-1}, when using laser excitation at 2.41 eV (see for example, Fig. 1-16). In the case of a disordered sample or at the edge of a graphene sample, we can also see the so-called disorder-induced D band, at about half of the frequency of the G′ band (around 1350 cm^{-1}, using laser excitation at 2.41 eV).

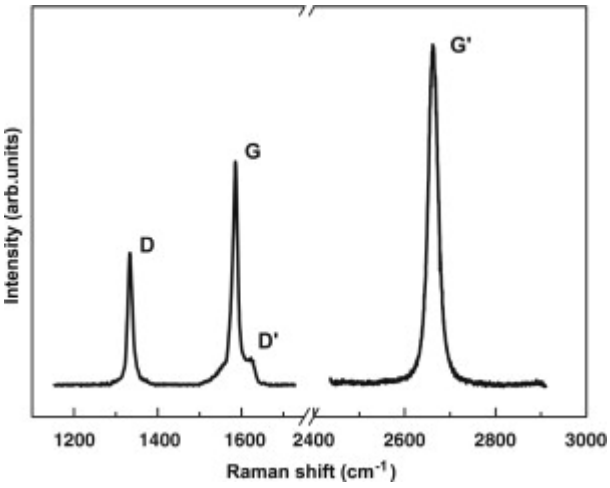

Figure 1-16. Raman spectrum of a graphene edge, showing the main Raman features, the D, G and G′ bands taken with a laser excitation energy of 2.41 eV. From Ref. [49].

The G band is associated with the doubly degenerated (iTO and LO) phonon mode at the Brillouin zone center. In fact, the G-band is the only band coming from a normal first order Raman scattering process in graphene. On the other hand, the G′ and D bands originate from a second-order process, involving two iTO phonons near the K point for the G′ band, or one iTO phonon and one defect in the case of the D band. Since the G′ band is approximately twice the frequency of the D band ($\omega_{G'} \sim 2\omega_D$), some authors prefer to call it the 2D band, due to the frequency relation between D band and 2D band. However, this two-phonon band is allowed in

the second-order Raman spectra of graphene without any kind of disorder or defects. In order to prevent any misleading connection of this feature with disorders or defects, and to avoid confusion between the designation of "2D" to denote two dimensionality, some researchers use the conventional notation "G′ band", since it is the second largest peak in graphene.

The origin and the dispersive behavior in the frequency of the D and G′ bands is to be found in the double resonance (DR) Raman process [53-55]. In the DR process, the wave-vectors q of the phonons associated with the D and G′ bands (measured from the K point) couple preferentially to the electronic states with wave-vectors k (measured from the K point), such that $q \approx 2k$. The double-resonance (DR) process shown in the center and right side of Fig. 1-17 begins with an electron of wave-vector $\boldsymbol{k}$ around K absorbing a photon of energy E_{laser}. The electron is inelastically scattered by a phonon or a defect of the wavevector $\boldsymbol{q}$ and energy E_{phonon} to a point belonging to a circle around the K′ point, with the wavevector $\boldsymbol{k}+\boldsymbol{q}$, where the K′ point is related to K by time reversal symmetry. The electron is then scattered back to a $\boldsymbol{k}$ state, and emits a photon by recombining with a hole at the $\boldsymbol{k}$ state. In the case of the D band, the two scattering processes consist of one elastic scattering event by the defects of the crystal, and one inelastic scattering event by emitting or absorbing a phonon, as shown in Fig. 1-17. In the case of the G′-band, both processes are inelastic scattering events and two phonons are involved. This double resonance mechanism is called an intervalley process, because it connects points in circles around equivalent K and K′ points in the first Brillouin zone of graphene. On the other hand, the double resonance process responsible for the D′ band (~1620 cm^{-1}) is an intravalley process, since it connects two points belonging to the same circle around the K point (or the K′ point) [55, 56].

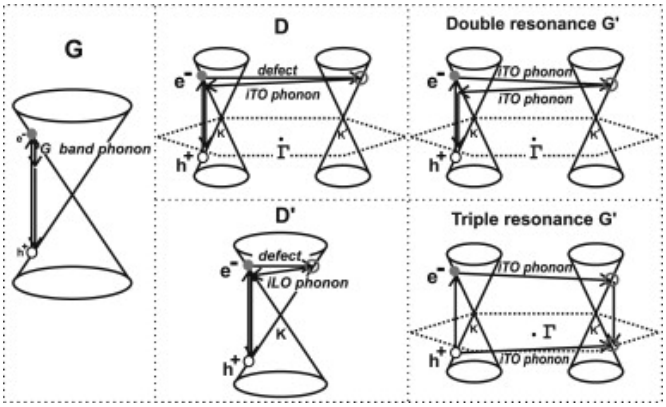

Figure 1-17. The origins from the main bands in graphene. From Ref. [49].

One can distinguish different layers in graphene by the changing shape of band, typically in G′-band. For single-layer graphene, there is only one energy band, so only one D peak and one G′ peak appears. For the case of bilayer graphene, since the energy band splits into two, D peak and G′ peak also split. With the number of layers of graphene increases, more splitting of bands occurs. The shape of the bands also changes and finally comes close to the shape of graphite peaks when the number of layers is large enough. The typical shapes of G′ band are shown in Fig. 1-18; the number of layers can be determined by the shape of the G′ band. This is the common method, widely used to identify the number of graphene layers.

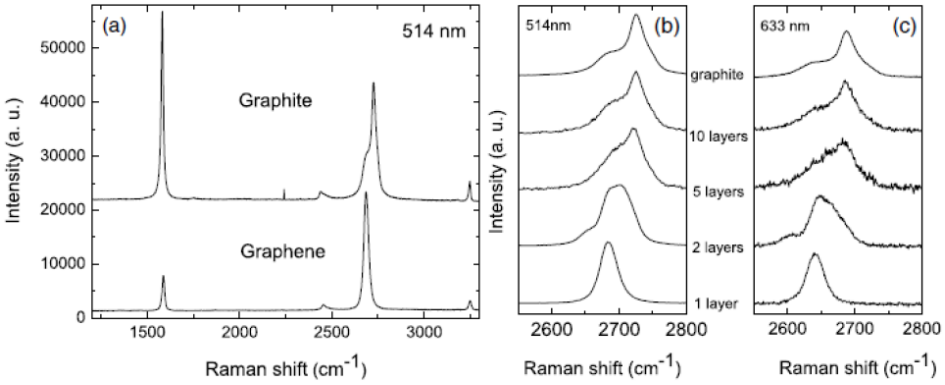

Figure 1-18. Raman spectra of various layers of graphene and graphite. G'-band is used for identifying the numbers of graphene layers. From Ref. [50].

1.3 Graphene Spintronics

In this part, I will review previous work in graphene spintronics. The main reasons why graphene is an attractive for spintronics are its a long spin lifetime (due to a small spin–orbit coupling of carbon atoms) and the negligible hyperfine interaction due to the absence of nuclear spins for the main isotope ^{12}C. The combination of the expected long spin lifetime with a high electron velocity, related to the linear dispersion relation of electrons in graphene, underlies the potential of graphene for spintronics. The ability to transport spin information efficiently over practical distances enables the development of further complex spintronic devices, e.g. the reconfigurable logic gate integrating both memory and logic proposed by Dery et al [57], and might eventually open the way to spin information processing.

In graphene spintronics, the electrical spin injection method, typically nonlocal method is widely used. This method was first proposed by Jedema and his co-workers in 2001 for a Py/Cu/Py structure. They demonstrated spin injection and nonlocal spin detection in Py/Cu/Py lateral spin valves (LSV) at room temperature (RT) [58] (see Fig. 1-19). The spin relaxation length of Cu has been estimated to be 350 nm at RT and 1000 nm at 4.2 K by studying the spacing dependence of the nonlocal magnetoresistance (MR). In 2002, Jedema and co-workers performed spin precession measurements in the Al strip, which clearly demonstrated that the nonlocal MR signal originates from spin injection and transport [59].

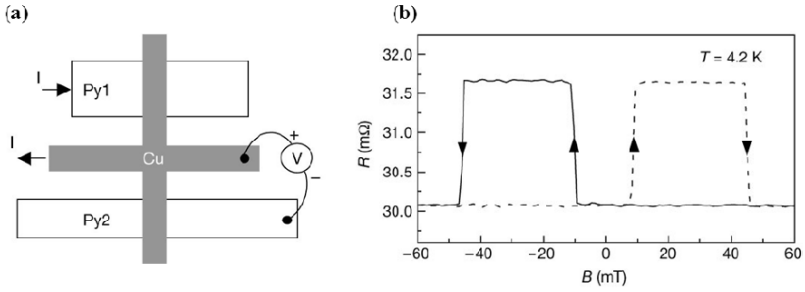

Figure 1-19. Electrical spin injection and accumulation in an Py/Cu/Py spin valve. (a) Nonlocal measurement geometry. (b) Nonlocal MR loop measured at 4.2 K. From Ref. [58].

There exists some debate on the issue of the first observation of spin transport in graphene. The first experiment on spin transport in graphene was reported in 2006 [60]. The problem of this research is its reliability, as the signal was quite unclear for a LSV experiment. In this report, a piece of graphene was connected to ferromagnetic electrodes by LSV as shown in Fig. 1-20 (a "local" configuration). The current flowing through the device depends on the persistence of the spin polarization and on whether the electrodes are magnetically aligned in a parallel or anti-parallel configuration.

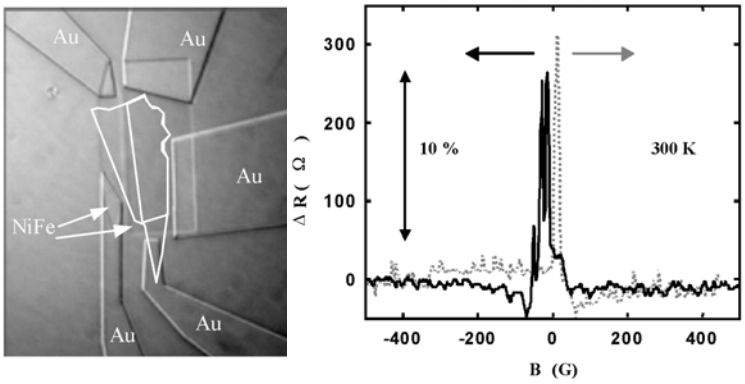

Figure 1-20. Report on spin transport in graphene by a LSV. From Ref. [60].

The LSV measurement was rapidly followed by several other spin transport measurements on single-layer graphene (SLG) and multi layer graphene (MLG) [23, 24, 61, 62]. Ref. 23 & 24 are the most popular reports, for their reliable contributions as pioneers on graphene spintronics. Basically there are two configurations for the measurements, called "local" and "nonlocal". The local configuration is a simple two-terminal device acting as an LSV. In the nonlocal configuration, four terminals are used, slightly different in geometry from those used in conventional four point measurements. Specifically, as seen in Fig. 1-21, the current path (between electrodes 3 & 4) is separated from the voltage measurement zone (electrodes 1 & 2). The nonlocal configuration was originally developed to extract low signals in semiconductors and metals, where the non-spin-aligned current would overwhelm the signal in local LSV measurements. As an example of this nonlocal configuration, Figure 1-21 shows the SLG device proposed by Tombros et al [24]. Injecting a spin polarized current at electrode 3 (Figure 1-21(b)) creates an out-of-equilibrium spin population in the graphene layer. The spin accumulations are defined by the difference of spin-up and spin-down carriers $(\Delta\mu = (\mu_{\uparrow} - \mu_{\downarrow}))$. This polarization of spins diffuse and is measured below electrodes 1 and 2, away from the electrical current (Figure 1-21(b)).The spatial spread of the spin polarization in a material is characterized by the spin diffusion length, λ_{sf}, which is related to the spin relaxation time, τ_{sf} (spin lifetime), in that material by $\lambda_{sf} = \sqrt{D \cdot \tau_{sf}}$, where D is the diffusion coefficient. An example of a

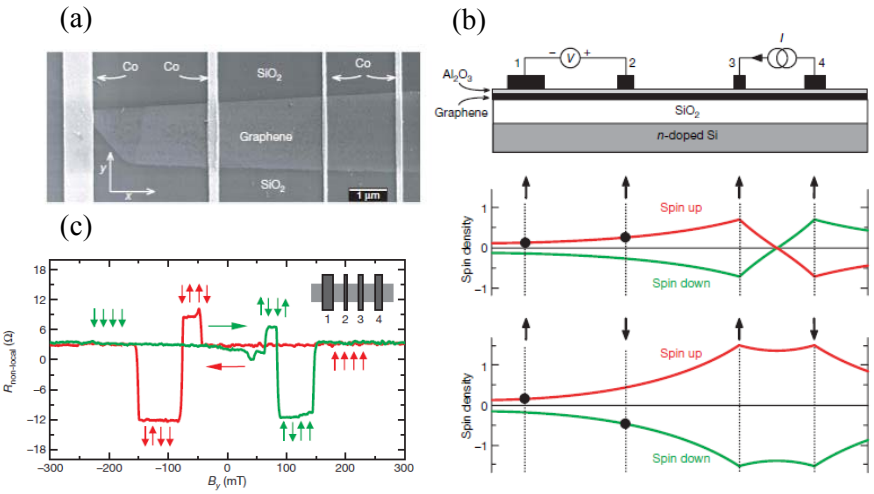

Figure 1-21 (a) An SEM top view of a four-terminal nonlocal device based on an exfoliated SLG. (b) Nonlocal measurement geometry of a graphene spin-valve device. (c) Spin signal s of device.

room-temperature nonlocal spin signal is shown in Fig. 1-21(c). The nonlocal spin signal appears as a difference in the nonlinear resistance $R_{nl} = V / I$ in different parallel and anti-parallel configurations of the magnetic electrodes as the magnetic field H is swept. These measurements were made at room temperature in a 600-nm-wide device with a 3-μm spacing between central electrodes 2 and 3. The amplitude of the signal depends not only on the length but also on the mean contact resistance, R_b, of the tunnel barrier between the graphene and the electrodes. A larger resistance prevents the spin from escaping into the electrodes and preserves a larger spin polarization. The measurement is usually analyzed according to a one-dimensional model based on the drift–diffusion equations. The nonlocal spin signal, ΔR_{nl}, can be expressed as [63]

$$\Delta R_{nl} = \pm \frac{2\gamma^2 \rho_{sq} \lambda_{sf}}{w} \frac{(wR_b / \rho_{sq}\lambda_{sf})^2 \exp(-L/\lambda_{sf})}{(1+wR_b / \rho_{sq}\lambda_{sf})^2 - \exp(-2L/\lambda_{sf})} \qquad (1\text{-}30)$$

where γ is the injection polarization, ρ_{sq} is the square(sheet) resistance of the material (graphene in this case), λ_{sf} is its spin diffusion length, w is its width, and L is the distance between injection and detection. This expression predicts an exponential decay, $\exp(-L/\lambda_{sf})$, of the spin signal as a function of the device length, except when λ_{sf} is very long, leading to slower $1/L$ decay. Based on the experimentally observed exponential variation, a spin diffusion length of 1.6 μm was derived for the graphene sample [63].

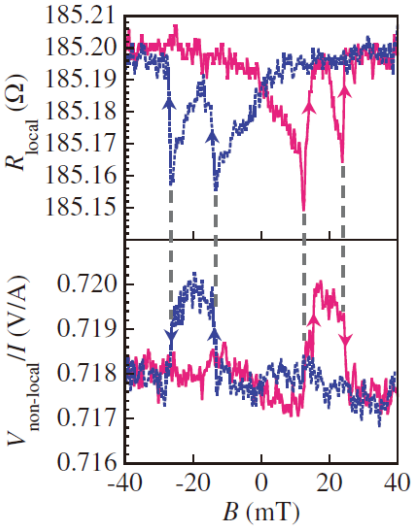

Figure 1-21. (d). The spin signal from Ref. [23].

Another important pioneer research on spintronics in multi-layer graphene was carried out by Ohishi et al [23], as shown in Fig. 1-21(d). In this report, the tunnel barrier was not used to increase the spin injection efficiency. They observed a clear spin signal from a nonlocal structure, which indicated the spin transport in graphene can also be realized without tunnel barriers. Unfortunately, the modulation of gate voltage was not observed in this research.

The spin transport parameters can also be extracted using the Hanle effect, in which a magnetic field is applied in a direction perpendicular to the spin accumulation and causes precession and dephasing of the spins in the lateral channel (see Fig. 1-22). This eventually leads to an oscillating decay of the spin signal, as

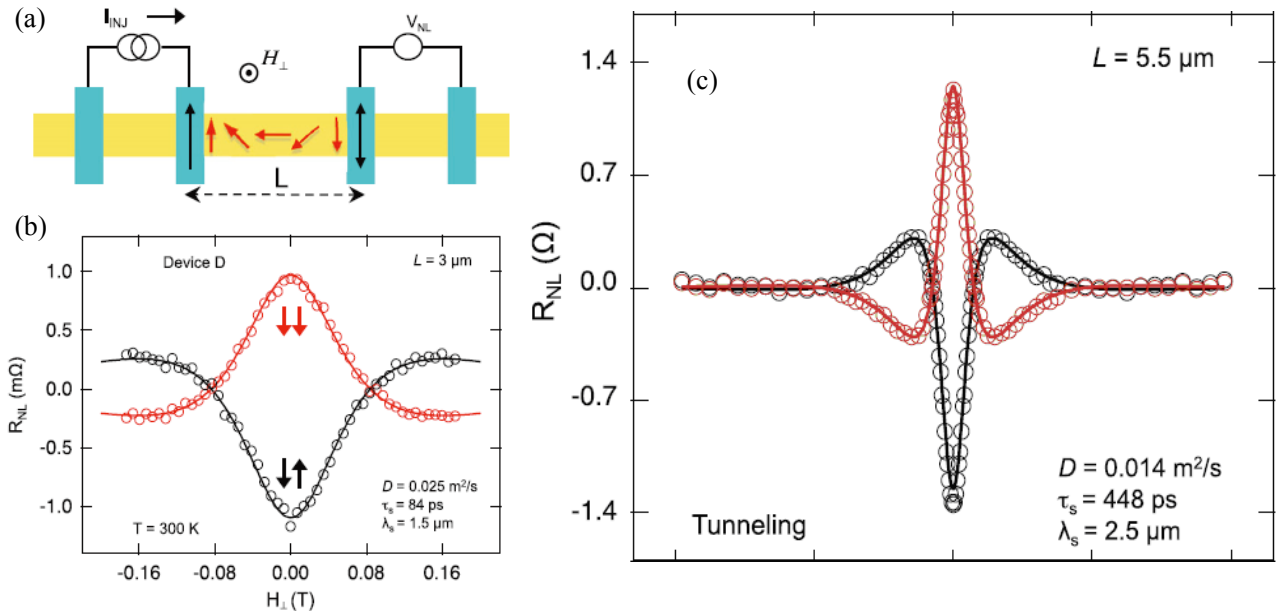

Figure 1-22**.** Hanle effect: (a) Application of an external magnetic field perpendicular to the channel plane forces the precession of the polarization of the spin current. (b), (c) Room-temperature Hanle curves recorded by Wei et al [64].

illustrated by the experimental results of Wei et al [64] in Fig. 1-22 (b)–(c). When the alignment between the applied field and the spin polarization suppresses the precession effects, the spin signal is restored. Fitting of the Hanle curves with solutions of Bloch equations leads to the determination of the diffusion constant D, spin life time τ_{sf}, and spin diffusion length λ_{sf}. In graphene samples, τ_{sf} and λ_{sf} values of up to 0.2 ns and 2.2 μm, respectively, were found at room temperature. Values in the same range were also later found by the Kawakami group [65-67]. By using the nonlocal techniques, they found $\tau_{sf} \approx 1$ ns at 4 K and $\tau_{sf} \approx 0.3$ ns at room temperature.

1.4 Recent studies on large-scale graphene

Whereas most of the spin-transport measurements have been made on exfoliated graphene on SiO_2, recent publications have also reported experiments performed on graphene grown by chemical vapor deposition (CVD) on copper foils and transferred onto SiO_2 [68]. These experiments showed spin transport properties similar to those of exfoliated graphene and introduced the interesting possibility of large-scale production of spin-transport devices, because large areas of CVD graphene can be fabricated easily. Another very interesting alternative for large-scale integration is epitaxially grown graphene on silicon carbide (SiC). In addition to their large size, epitaxial graphene (EG) samples also show very high mobility [69]. However, graphene layers grown on the silicon-terminated face (Si face) of SiC show different structures and properties from those grown on the carbon terminated face (C face), and this is also true for spin transport. For the Si face, which allows easier control of layer growth, Maassen et al [70] performed nonlocal spin transport measurements on multilayer epitaxial graphene (MEG). They found an average mobility of ~1900 $cm^2V^{-1}s^{-1}$ and τ_{sf} values on par with those of the best exfoliated samples (up to 2.3 ns at low temperature) but with surprisingly small diffusion constants and λ_{sf} values in comparison. For the C face, Dlubak et al [71] explored spin transport on MEG (~10 layers) (see Figure 1-23). Although the number of layers is more difficult to control, this type of graphene is composed of uncoupled monolayer graphene sheets (it is not simply a thin graphite layer), leading to better

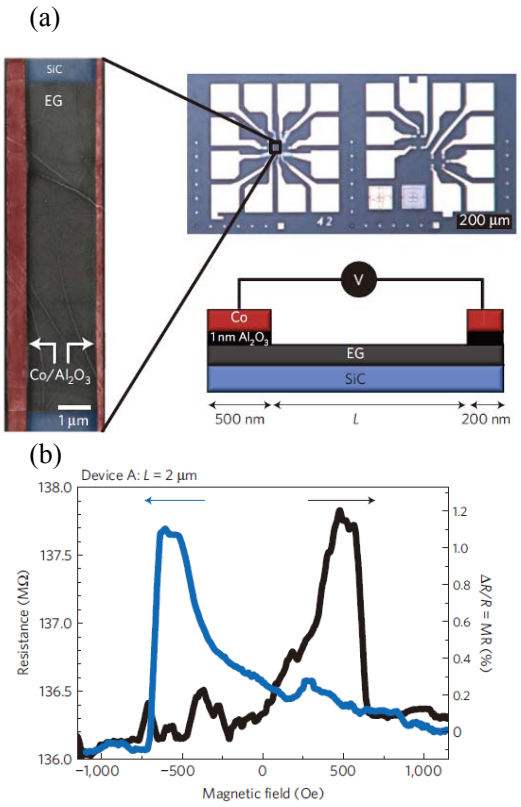

Figure 1-23. A two-terminal local spin device of graphene [71], (a) SEM image of a two-terminal local spin valve, optic image of samples and schematic view of device. (b) local spin signals measured at 4 K.

transport properties. Dlubak et al found very high mobilities, of ~17,000 $cm^2V^{-1}s^{-1}$. In these samples, cobalt/alumina tunnel junctions of very large resistance, in the megaohm range, were used as injectors and detectors [72]. Local magnetoresistance (MR) curves obtained with MEG [71] are shown in Fig. 1-23 (b) with local spin signals (ΔR) in the megaohm range. These observed spin signals, much larger than the resistances of the cobalt electrodes and graphene channel, are the largest spin signals ever observed with graphene. This study attributed the impressive spin signal of these devices to the length of λ_{sf} in the 100 μm range and above. Such spin diffusion lengths, much longer than those reported previously, are probably related to the very high mobility and high quality of C-face SiC epitaxial graphene. But the spin signals (even though they were large) were very unreliable, compared to those in other reports, as shown in Fig. 1-21. Therefore the reliability of this research is still under debate. The main results of almost all previous research estimated the spin diffusion length to be around 2 μm in graphene.

1.5 Spin relaxation in graphene

There are two main spin relaxation processes, one that requires energy exchange, and one that does not. Assuming that the total spin is S and the external magnetic field is B in the z direction, the spins diffuse, decay and precess as follows:

$$\begin{aligned}
\frac{dS_z}{dt} &= \frac{g\mu B}{\hbar}(B\cdot S)_z - \frac{S_z}{T_1} + D\nabla^2 S_z, \\
\frac{dS_x}{dt} &= \frac{g\mu B}{\hbar}(B\cdot S)_x - \frac{S_x}{T_2} + D\nabla^2 S_x, \\
\frac{dS_y}{dt} &= \frac{g\mu B}{\hbar}(B\cdot S)_y - \frac{S_y}{T_2} + D\nabla^2 S_y,
\end{aligned} \qquad (1\text{-}31)$$

in which the g is the electron g factor, μ_B is the Bohr magneton, and D is the spin diffusion coefficient. T_1 is the longitudinal relaxation time and T_2 is the transverse relaxation time, also known as spin dephasing time. Electrically, T_2 can be measured in a spin precession measurement, with the magnetic field perpendicular to the spin direction. T_1 can be measured through the spacing dependence of the spin signal. Both T_1 and T_2 are

affected by the interaction of spins with other degrees of freedom.

1.5.1 Elliot-Yafet mechanism

The Elliot-Yafet mechanism was first proposed by Elliot and Yafet (EY). The EY mechanism is generated by the local atomic electric field induced by the lattice ions flipping the spins via spin-orbit coupling [73, 74]. As shown in Fig. 1-24 (a), the electron has a chance to flip its spin at each scattering by impurities or phonons. The EY mechanism leads to a linear relationship of the spin relaxation rate and momentum scattering rate, and the spin diffusion length ($\lambda_{sf} = \sqrt{D \cdot \tau_{sf}}$) will be linearly proportional to the mean free path.

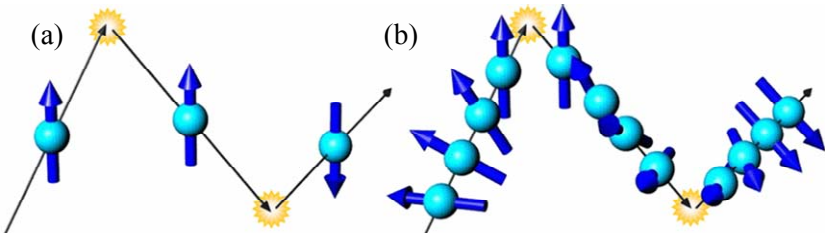

Figure 1-24. Spin relaxation mechanisms (a) Elliot-Yafet mechanism. (b) Dyakonov-Perel mechanism.

1.5.2 D'yakonov-Perel mechanism

The D'yakonov-Perel (DP) mechanism exists in a crystal lacking inversion symmetry with spin orbit coupling. In such systems, a finite electric field will induce a momentum-dependent effective magnetic field $B(k)$. The spins will precess around this effective magnetic field with a Larmor frequency, i.e. $\omega(k) = e/m^* B(k)$. However, random changes of the direction and frequency of the spins will lead to less spin relaxation and longer spin lifetimes (Fig. 1-24(b)). In other words, the spin relaxation rate will be inversely proportional to the momentum scattering rate, which is the opposite of the EY mechanism.

There is much debate over the dominant spin relaxation mechanism in graphene. In the theoretical studies, both the EY and the DP spin relaxation mechanism are still being discussed [75-77]. In the experimental studies, the van Wees group believes the EY spin relaxation is the dominant spin relaxation mechanism in graphene

from SLG to 14-layer graphene. The Özyilmaz group and the Kawakami group show the importance of the EY spin relaxation in SLG, and of the DP spin relaxation in BLG, as shown below in detail.

It was observed by the van Wees group [78] that λ_{sf} increased linearly with the diffusion constant (proportional to τ_p, the momentum scattering time). This led the authors to suggest that, for their samples at least, the mechanism of spin relaxation was of the Elliot–Yafet (EY) type. Another interesting result was more recently obtained for MLG by the same group [79]. They found that τ_{sf} increased with the number of layers. In the framework of the EY mechanism, this increase in τ_{sf} can be attributed to a better screening of the external scattering potentials, as reported for suspended graphene [80]. In agreement with the conclusions of the van Wees group, the Kawakami group found a decrease in τ_{sf} as τ_p decreased, suggesting the dominance of EY spin relaxation. However, interestingly, in experiments on bilayer graphene (BLG), they found the opposite behavior: a τ_{sf} value of up to 6.2 ns at low temperature and close to 1 ns at room temperature [66]. Compared to the experiments on SLG by the same group, surprisingly, this inverse dependence on τ_p suggests the dominance of the DP mechanism, which relates spin flips to the accumulation of lattice-induced precession of the spin between scattering events. Thus, increased τ_p leads to increased τ_{sf}. Wei et al also found [67] that organic-ligand-bound gold nanoparticles, although introducing faster momentum scattering by localized charges, had no effect on τ_{sf}. More recently, the interpretation of the observed variation of τ_{sf} with τ_p and its relationship to the two mechanisms has been investigated. In most experiments, the variation of τ_p (which is proportional to μ, the mobility) is controlled through the variation of the charge density n through a gate, for which $\tau_p \propto 1/n$. However, it was shown that, away from the Dirac point, for the EY mechanism, $\tau_{sf} \propto 1/\tau_p$. Also, the EY mechanism could turn into DP-like behavior. In addition, it was suggested that the DP mechanism could in some cases lead to EY-like behavior [77]. With contradictory results for τ_{sf} for different types of samples, the mechanism of spin relaxation in graphene is not yet clear, and it appears that no straightforward distinction can be made between the Elliot-Yafet and Dyakonov-Perel mechanisms with the available

experimental data. One direction for future work is the study (both theoretical and experimental) of the EG samples for which the longest τ_{sf} (a few hundred nanoseconds) and λ_{sf} (a few hundred micrometers) were found [71]; another way is to find some new methods of spin injection, to investigate the spin diffusion and spin relaxation in graphene from a different standpoint.

1.5.3 Spin orbit coupling in graphene

The spin-orbit (SO) coupling in graphene is given by a Rashba-like term in the Hamiltonian [78]: $H_{SO} = -\frac{\Delta}{2}(\hat{\sigma} \times \hat{s})_z$ where Δ is the SO coupling strength, $\hat{s} = (\hat{s}_x, \hat{s}_y)$ are the Pauli matrices for the electron spin and $\hat{\sigma} = (\hat{\sigma}_x, \hat{\sigma}_y)$ are the Pauli matrices for the pseudospin which is associated with the A-B sublattices. There are three types of SO couplings: the intrinsic SO coupling (Δ_{int}), the electrical field (ε_z) induced Rashba SO coupling (Δ_{ε}), and the curvature induced SO coupling (Δ_{curv}). Typical calculated values are Δ_{int} = 0.01 K (10^{-6} eV) [67-69], Δ_{ε} = 0.07 - 0.13 K, (~10^{-5} eV) for ε = 50 V/300 nm, and Δ_{curv}= 0.20 K (1.7×10^{-5} eV) for a radius of the curvature of 100 nm. The total SO coupling will be the sum up of these three parts $\Delta = \Delta_{int} + \Delta_{\varepsilon} + \Delta_{curv}$. Typically, the EY mechanism should be more important for "dirty" samples, and the DP mechanism should be more important for "clean" samples. The spin relaxation time for the EY mechanism, τ_{EY}, is given by $\tau_{EY} \sim \tau(\hbar v_F k_F)^2 / \Delta^2$, where τ is the momentum scattering time [78]. The spin relaxation time for the DP mechanism, τ_{DP}, is given by $\tau_{EY} \sim \tau^{-1}(\hbar / \Delta)^2$. The total spin relaxation time, τ_S, is given by $\tau_s^{-1} = \tau_{EY}^{-1} + \tau_{DP}^{-1}$. The spin relaxation is estimated using reasonable graphene parameters (v_F = 10^6 m/s, carrier density n = 10^{12} cm^{-2}, $k_F = \sqrt{2\pi n}$). For the intrinsic SO coupling ($\Delta = \Delta_{int} = 10^{-6} eV$), τ_S can be as high as ~100 μs (at electron mean free path of 4 nm). For the curvature-enhanced SO coupling ($\Delta = \Delta_{curv} = 1.7\times10^{-5} eV$), τ_S can be as high as ~200 ns.

1.6 Towards spin transport in graphene from a new standpoint

As mentioned in section 1.3, it is necessary to investigate the spin transport properties in graphene from a different viewpoint; until now, the investigations on spin transport in graphene [23, 24, 61, 62] have always focused on the electrical spin injection method, which is not enough. Besides electrical spin injection/detection method, the spin pumping method for injecting spins from ferromagnetic material to condensed matter [86, 87] is with the detection method called the inverse spin Hall effect (ISHE) (the details will be explained in the next chapter). These methods have been reported by Saitoh's group [88]. They applied microwave onto a ferromagnetic material NiFe (Py) to induce the spin precession of magnetization in Py. The loss of spin angular momentum was conserved to the connected nonmagnetic material, Pt. The spin current in the Pt generated a charge current due to the ISHE. Saitoh et al provided a new method for spin injection and spin detection, which does not use the electric current for spin injection at all, although no spin transport was observed in their study. Another advantage of spin pumping method is the efficiency of spin injection by large electrodes. It has been reported that spin injection efficiency drastically decreased by increasing the electrode sizes in the electrical method [89]. On the other hand, the conductance mismatch problem restricts the spin injection from FM to semiconductors or organic materials due to the large different in conductivities. Tunnel barriers are always used to circumvent this impedance mismatch problem. At this point, the spin pumping method provides a simple way to inject spins without any barriers since the spin angular momentum is conserved from FM to NM, rather than injecting of carriers into NM. After the demonstration of spin pumping and ISHE, spin wave spin current was achieved in YIG by using the spin pumping method by Saitoh's group [90]. This method expected to be further applied to investigation about the spin transport of pure spin current in graphene spintronics.

1.7 Purpose of this study and outline

In graphene research, the focus has been on the limited spin diffusion length and the unclear spin relaxation, so it is essential to make an effort to establish a new method for investigating spin transport properties in graphene.

In this thesis, I mainly present the experimental results about spin transport on SLG by magnetization dynamics, including the observation of pure spin current of spin transport in SLG at room temperature by spin pumping, the temperature dependence of the spin Hall angle of palladium, and the temperature dependence of spin coherence in SLG by spin pumping. The chapters and the contents in this thesis each deal with the following issues:

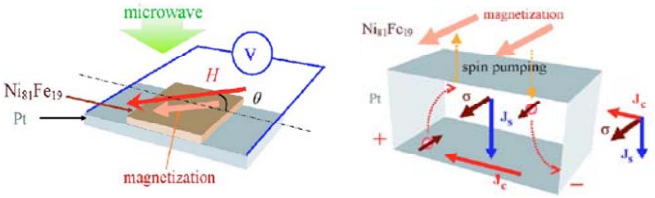

Figure 1-25. Schematic view of Py/Pt spin pumping device. From Ref. [88].

Chapter 3:

I present the detailed results of dynamical spin injection into SLG, successfully observe the ISHE output voltage in Pd and demonstrate the generation of pure spin current in SLG by the spin pumping method. The spin coherence was estimated to agree with other reports. The difference in the spin diffusion length of the two samples is due to the amount of defects in SLG.

Chapter 4:

I investigate the temperature dependence of the spin Hall angle of Pd by the spin pumping method It was found to decrease with increasing temperature, which is different with the behavior of Pt [91]. The origin of this characteristic temperature-dependence of the spin Hall angle of Pd is not clear yet.

Chapter 5:

I continue the study of the temperature-dependence of spin coherence in SLG by magnetization dynamics. The spin coherence was found to be independent of temperature. The result is consistent with previous reports using the electrical method on CVD-grown SLG [64].

References

[1] S. A. Wolf, D. D. Awschalom, R. A. Buhrman, J. M. Daughton, S. von Molnar, M. L. Roukes, A. Y. Chtchelkanova, and D. M. Treger, Science **294**, 1488 (2001).

[2] I. Zutic, J. Fabian, and S. Das Sarma, Rev. Mod. Phys **76**, 323 (2004).

[3] C. Chappert, A. Fert, and F. Nguyen Van Dau, Nature Materials **6**, 813 (2007).

[4] A. Fert, Rev. Mod. Phys. **80**, 1517 (2008).

[5] S. D. Bader, and S. S. P. Parkin, Annual Review of Condensed Matter Physics **1**, 71 (2010).

[6] C. H. Bennett, and D. P. DiVincenzo, Nature **404**, 247 (2000).

[7] M. N. Baibich, J. M. Broto, A. Fert, F. N. Van Dau, and F. Petroff, Phys. Rev. Lett. **61**, (1988).

[8] G. Binasch, P. Grünberg, F. Saurenbach, and W. Zinn, Phys. Rev. B **39**, 4828 (1989).

[9] M. Julliere, Phys. Lett. A **54**, 225 (1975).

[10] P. M. Tedrow, and R. Meservey, Phys. Rev. Lett. **26**, 192 (1971).

[11] M. A. Ruderman, and C. Kittel, Phys. Rev. **96**, 99 (1954).

[12] T. Kasuya, Prog. Theo. Phys. **16**, 45 (1956).

[13] K. Yosida, Phys. Rev. **106**, 893 (1957).

[14] J. S. Moodera, L. R. Kinder, T. M. Wong, and R. Meservey, Phys. Rev. Lett. **74**, 3273 (1995).

[15] T. Miyazaki, and N. Tezuka, J. Magn. Magn. Mater. **139**, L231 (1995).

[16] S. S. P. Parkin, C. Kaiser, A. Panchula, P. M. Rice, B. Hughes, M. Samant, and S.-H. Yang, Nat. Mater. **3**, 862 (2004).

[17] S. Yuasa, T. Nagahama, A. Fukushima, Y. Suzuki, and K. Ando, Nat. Mater. **3**, 868 (2004).

[18] W. H. Butler, X.-G. Zhang, T. C. Schulthess, and J. M. MacLaren, Phys. Rev. B **63**, 054416 (2001).

[19] S. Ikeda, J. Hayakawa, Y. Ashizawa, Y. M. Lee, K. Miura, H. Hasegawa, M. Tsunoda, F. Matsukura, and H. Ohno, Appl. Phys. Lett. **93**, 082508 (2008).

[20] S. Datta, and B. Das, Appl. Phys. Lett. **56,** 665 (1990).

[21] Y. Ohno, D.K. Young, B. Beschoten, F. Matsukura, H. Ohno, and D.D. Awschalom, Nature **402**, 790 (1999)

[22] T. Matsuno, S. Sugahara, and M. Tanaka, Jpn. J. Appl. Phys. **43**, 6032 (2003).

[23] M. Ohishi, M. Shiraishi, R. Nouchi, T. Nozaki, T. Shinjo, and Y. Suzuki, Jpn. J. Appl. Phys. **46**, L605 (2007).

[24] N. Tombros, C. Jozsa, M. Popinciuc, H.T. Jonkman, and B.J. van Wees, Nature **448**, 571 (2007).

[25] Z. H. Xiong, D. Wu, Z. V. Vardeny, and J. Shi, Nature **427**, 821 (2004).

[26] T. S. Santos, J. S. Lee, P. Migdal, C. Lekshmi, B. Satpati, and J. S. Moodera, Phys. Rev. Lett. **98**, 016601 (2007).

[27] V. Dediu, L. E. Hueso, I. Bergenti, A. Riminucci, F. Borgatti, P. Graziosi, C.Newby, F. Casoli, M. P. De Jong, C. Taliani, and Y. Zhan, Phys. Rev. B **78**, 115203 (2008).

[28] D. Sun, L. Yin, C. Sun, H. Guo, Z. Gai, X.-G. Zhang, T. Z. Ward, Z. Cheng, and J. Shen, Phys. Rev. Lett. **104**, 236602 (2010).

[29] K. V. Raman, S. M. Watson, J. H. Shim, J. A. Borchers, J. Chang, and J. S. Moodera, Phys. Rev. B **80**, 195212 (2009).

[30] J.-W. Yoo, H. W. Jang, V. N. Prigodin, C. Kao, C. B. Eom, and A. J. Epstein, Phys. Rev. B **80**, 205207 (2009).

[31] J.-W. Yoo, C.-Y. Chen, H. W. Jang, C. W. Bark, V. N. Prigodin, C. B. Eom, and A. J. Epstein, Nat. Mater. **9**, 638 (2010).

[32] D. Huertas-Hernando, F. Guinea, and A. Brataas, Phys. Rev. B **74**, 155426 (2006).

[33] B. Trauzettel, D. V. Bulaev, D. Loss, and G. Burkard, Nat. Phys. **3**, 192 (2007).

[34] K. Tsukagoshi, B. W. Alphenaar, and H. Ago, Nature **401**, 572 (1999).

[35] S. Sahoo, T. Kontos, J. Furer, C. Hoffmann, M. Graber, A. Cottet, and C.Schonenberger, Nat. Phys. **1**, 99 (2005).

[36] H. T. Man, I. J. W. Wever, and A. F. Morpurgo, Phys. Rev. B **73**, 241401(R) (2006).

[37] N. Tombros, S. J. v. d. Molen, and B. J. van Wees, Phys. Rev. B **73**, 233403 (2006).

[38] L. E. Hueso, J. M. Pruneda, V. Ferrari, G. Burnell, J. P. Valdes-Herrera, B. D.Simons, P. B. Littlewood, E. Artacho, A. Fert, and N. D. Mathur, Nature **445**, 410 (2007).

[39] K. S. Novoselov, A. K. Geim, S. V. Morozov, D. Jiang, Y. Zhang, S. V. Dubonos,I. V. Grigorieva, and A. A. Firsov, Science **306**, 666 (2004).

[40] A. K. Geim, and K. S. Novoselov, Nat. Mater. **6**, 183 (2007).

[41] C. Berger, Z. Song, T. Li, X. Li, A. Y, Ogbazghi, R. Feng, Z. Dai, A. N. Marchenkov, E. H. Conrad, P. N. First, and W. A. d. Heer, J. Phys. Chem. B **108**, 19912 (2004).

[42] K. S. Kim, Y. Zhao, H. Jang, S. Y. Lee, J. M. Kim, K. S. Kim, J.-H. Ahn, P. Kim, J.-Y. Choi, and B. H. Hong, Nature **457**, 706 (2009).

[43] X. Li, W. Cai, J. An, S. Kim, J. Nah, D. Yang, R. Piner, A. Velamakanni, I. Jung, E. Tutuc, S. K. Banerjee, L. Colombo, and R. S.Ruoff, Science **324,** 5932 (2009).

[44] H. Ago, Y. Ito, N. Mizuta, K. Yoshida, B. Hu, C. M. Orofeo, M. Tsuji, K. Ikeda, S. Mizuno. ACS Nano **4**(12), 7407-7414 (2010).

[45] P.R.Wallace, Phys. Rev. **71**, 622 (1947).

[46] 齋藤理一郎, 篠原久典 「カーボンナノチューブの基礎と応用」 p.16 培風館 (2004).

[47] Kevin T. Chan, J. B. Neaton, and Marvin L. Cohen, Phys. Rev. B **77**, 235430 (2008).

[48] P. A. Khomyakov, G. Giovannetti, P. C. Rusu, G. Brocks, J. van den Brink, and P. J. Kelly, Phys. Rev. B **79**, 195425 (2009).

[49] L.M. Malard, M.A. Pimenta, G. Dresselhaus, and M.S. Dresselhaus, Phys. Rep. **73**, 51 (2009).

[50] A.C. Ferrari, J.C. Meyer, V. Scardaci, C. Casiraghi, M. Lazzeri, M. Mauri, S. Piscanec, Da Jiang, K.S. Novoselov, S. Roth, and A.K. Geim, Phys. Rev. Lett. **97,** 187401 (2006).

[51] K. S. Novoselov, A. K. Geim, S. V. Morozov, D. Jiang, Y. Zhang, S. V. Dubonos, I. V. Grigorieva, and A. A. Firsov, Science **306**, 666 (2004).

[52] M. Lazzeri, C. Attaccalite, L. Wirtz, and Francesco Mauri, Phys. Rev. B **78,** 081406, (2008).

[53] A.V. Baranov, A.N. Bekhterev, Y.S. Bobovich, and V.I. Petrov, Opt. Spectrosk. **62**, 1036, (1987).

[54] C. Thomsen, and S. Reich, Phys. Rev. Lett. **85**, 5214, (2000).

[55] R. Saito, A. Jorio, A.G. Souza Filho, G. Dresselhaus, M.S. Dresselhaus, and M.A. Pimenta, Phys. Rev. Lett. **88,** 027401, (2002).

[56] R. Saito, A. Grüneis, Ge.G. Samsonidze, V.W. Brar, G. Dresselhaus, M.S. Dresselhaus, A. Jorio, L.G. Cançado, C. Fantini, M.A. Pimenta, and A.G. Souza Filho, New J. Phys. **5**, 157.1,(2003).

[57] H. Dery , H. Wu , B. Ciftcioglu , M. Huang , Y. Song , R. Kawakami , J. Shi ,I. Krivorotov , I. Zutic , and L.J. Sham , IEEE Trans. Electron Devices **59** , 259 (2011).

[58] F. J. Jedema, A. T. Filip, and B. J. van Wees, Nature **410**, 345 (2001).

[59] F. J. Jedema, H. B. Heersche, A. T. Filip, J. J. A. Baselmans, and B. J. van Wees, Nature **416**, 713 (2002).

[60] E.W. Hill, A.K. Geim, K. Novoselov, F. Schedin, and P. Blake, IEEE Trans. Magn. **42** (10), 2694 (2006).

[61] H. Goto, A. Kanda, T. Sato, S. Tanaka, Y. Ootuka, S. Odaka, H. Miyazaki, K. Tsukagoshi, and Y. Aoyagi, Appl. Phys. Lett. **92** (21), 212110 (2008).

[62] S. Cho, Y.F. Chen, and M. Fuhrer, Appl. Phys. Lett. **91** (12), 123105 (2007).

[63] M. Popinciuc, C. Jozsa, P.J. Zomer, N. Tombros, A. Veligura, H.T. Jonkman, and B.J. van Wees, Phys. Rev. **80** (21), 214427 (2009).

[64] W. Han, K.M. McCreary, K. Pi, W.H. Wang, Y. Li, H. Wen, J.R. Chen, and R.K. Kawakami, J. Magn. Magn. Mater. **324** (4), 365 (2012).

[65] W. Han, K. Pi, K.M. McCreary, Y. Li, J.I. Wong, A. Swartz, and R.K. Kawakami, Phys. Rev. Lett. **105** (16), 167202 (2010).

[66] W. Han, and R.K. Kawakami, Phys. Rev. Lett. **107** (4), 047207 (2011).

[67] W. Han, J.R. Chen, D. Wang, K.M. McCreary, H. Wen, A.G. Swartz, J. Shi, and R.K. Kawakami, Nano Lett. **23**, 135203 (2012).

[68] A. Avsar, T.Y. Yang, S. Bae, J. Balakrishnan, F. Volmer, M. Jaiswal, Z. Yi, S.R. Ali, G. Guntherodt, B.H. Hong, B. Beschoten, and B. Ozyilmaz, Nano Lett. **11** (6), 2363 (2011).

[69] M. Sprinkle, D. Siegel, Y. Hu, J. Hicks, A. Tejeda, A. Taleb-Ibrahimi, P. Le Fèvre, F. Bertran, S. Vizzini, H. Enriquez, S. Chiang, P. Soukiassian, C. Berger, W.A. de Heer, A. Lanzara, E. Conrad, Phys. Rev. Lett. **103** (22), 226803 (2009).

[70] T. Maassen, J.J. van den Berg, N. Ijbema, F. Fromm, T. Seyller, R. Yakimova, and B.J. van Wees, Nano Lett. **12** (3), 1498 (2012).

[71] B. Dlubak, M.B. Martin, C. Deranlot, B. Servet, S. Xavier, R. Mattana, M. Sprinkle, C. Berger, W.A. De Heer, F. Petroff, A. Anane, P. Seneor, A. Fert, Nat. Phys. **8** (7), 557 (2012).

[72] B. Dlubak, P. Seneor, A. Anane, C. Barraud, C. Deranlot, D. Deneuve, B. Servet, R. Mattana, F. Petroff , and A. Fert, Appl. Phys. Lett. **97** (9), 092502 (2010).

[73] R. J. Elliott, Phys. Rev. **96**, 266 (1954).

[74] Y. Yafet, in Solid State Physics, edited by F. Seitz and D. Turnbull (Academic Press Inc., New York, 1963), Vol. 14, p. 1.

[75] A. H. Castro Neto, and F. Guinea, Phys. Rev. Lett. **103**, 026804 (2009).

[76] Ochoa H, Castro Neto A H, Guinea F. Phys. Rev. Lett. **108**(20), 206808 (2012).

[77] P. Zhang and M. W. Wu, New J Phys. **14** 033015 (2012).

[78] C. Jozsa, T. Maassen, M. Popinciuc, P.J. Zomer, A. Veligura, H.T. Jonkman, and B.J. van Wees, Phys.

Rev. B **80** (24), 241403 (R) (2009).

[79] T. Maassen, F.K. Dejene, M.H.D. Guimaraes, C. Jozsa, B.J. van Wees, Phys. Rev. B **83** (11), 115410 (2011).

[80] K.I. Bolotin, K.J. Sikes, Z. Jiang, M. Klima, G. Fudenberg, J. Hone, P. Kim, and H.L. Stormer, Solid State Commun. **146** (9–10), 351 (2008).

[81] H. Ochoa, A.H. Castro-Neto, and F. Guinea, Phys. Rev. Lett. **108** (20), 206808 (2012).

[82] D. Huertas-Hernando, F. Guinea, and A. Brataas, Phys. Rev. Lett. **103**, 146801 (2009).

[83] H. Min, J. E. Hill, N. A. Sinitsyn, B. R. Sahu, L. Kleinman, and A. H. MacDonald, Phys. Rev. B **74**, 165310 (2006).

[84] D. Huertas-Hernando, F. Guinea, and A. Brataas, Phys. Rev. B **74**, 155426 (2006).

[85] Y. Yao, F. Ye, Y.-L. Qi, S.-C. Zhang, and Z. Fang, Phys. Rev. B **75**, 041401(R) (2007).

[86] Y. Kitamura, E. Shikoh, Y. Ando, T.Shinjo, and M.Shiraishi, Sci. Rep. **3** 1739 (2013).

[87] M. Koike, E. Shikoh, Y. Ando, T. Shinjo, S. Yamada, K. Hamaya, and M. Shiraishi, Appl. Phys. Express **6** 023001 (2013).

[88] K. Ando and E. Saitoh, J. Appl. Phys. **108** 113925 (2010).

[89] M. Morota, Y. Niimi, K. Ohnishi, D. H. Wei, T. Tanaka, H. Kontani, T. Kimura, and Y. Otani, Phys. Rev. B **83,** 174405 (2011).

[90] Y. Kajiwara, K. Harii, S. Takahashi, J.Ohe, K. Uchida, M. Mizuguchi, H. Umezawa, H. Kawai, K. Ando, K. Takanashi, S. Maekawa and E. Saitoh, Nature **464**, 7286, (2010).

[91] M. Morota, Y. Niimi, K. Ohnishi, D. H. Wei, T. Tanaka, H. Kontani, T. Kimura, and Y. Otani, Phys. Rev. B **83** 174405 (2011).

Chapter 2

Theory and experiments

Abstract

This section is divided into two parts. In the first, I discuss the theoretical aspects of the dynamical spin injection theory and the effect of the inverse spin Hall effect on spin detection. The ferromagnetic resonance condition is also discussed. The applicability of existing models to my study is also discussed. In the second part, I show the details of the fabrication procedures.

2.1 Pure spin current

Pure spin current is a new concept, which is defined as $J_s = J_\uparrow - J_\downarrow$. To understand pure spin current clearly, we start from the normal electric current that has been used in our daily lives for over 200 years. In a normal electric current, an equivalent amount of up-spin electrons and down-spin electrons move in the same direction. The total number of contributed electrons in the electric current is four, and the total number of spins in this case is zero. In the second illustration in Fig. 2-1, the spin-polarized electric current means the carriers move with spins. As shown in the pure spin current case in Fig. 2-1, the total number of electrons contributing to charge current is zero, but the spin current obeys the time reversal symmetry, so the up-spins move from left to right, is equivalent to the same amount of down spins move to the opposite direction. Therefore, in a solid, the existence of a spin current can be modeled as the same number of electrons with opposite spins traveling in opposite directions along the spin-current spatial direction. Since there is no energy dissipation for the time reversal symmetric motion, the utilization of pure spin current is a potential method for the realization of low energy consumption devices in the future.

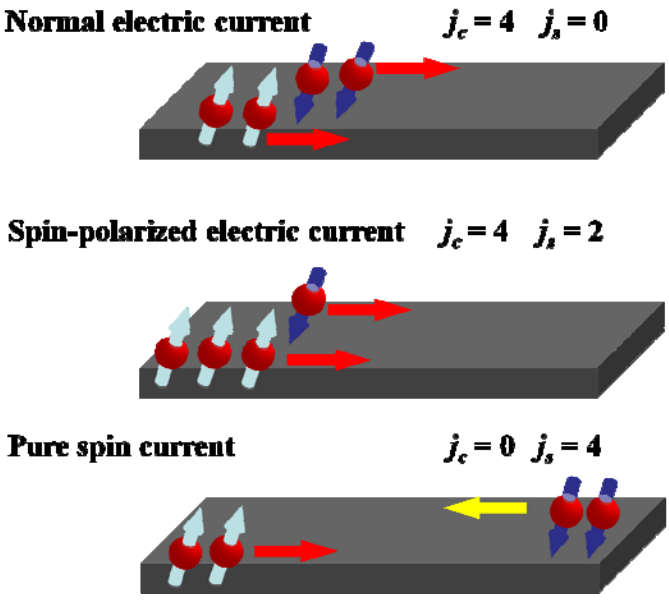

Figure 2-1. Concept of electric current and spin current.

2.2 Landau Lifshitz Gilbert (LLG) equation

In 1935, Landau and his student Lifshitz came up with the famous LL equation in their theory of magnetic domain and domain wall resonance. The first term in the LL equation can be derived from the Heisenberg equation of spin, which is related to the energy conservation of magnetic-free energy. The second term in the LL equation was said to originate from the relativistic interaction between the magnetic moment and the crystal in the original paper [1]. Nowadays this nonlinear second term is believed to be caused by the dissipative process, which is difficult to explain accurately, but is similar to the frictional force (see Fig. 2-2). The atomic magnetic moment $\mu_a = -g\mu_B \mathbf{S}$, where g is the g-factor, μ_B is the Bohr magnet, and $\mathbf{S}$ is the atomic spin. If we omit energy dissipation, the eigenvalue of the Hamiltonian $\mathscr{H} = -\mu_a \cdot \mathbf{H}$, is conserved. Then we can use Heisenberg's equations to describe the motion of spin $\mathbf{S} = \hat{e}_i S_i$:

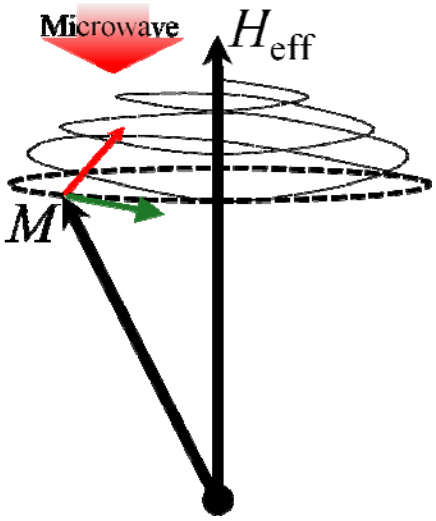

Figure 2-2. Directions of precession term and damping term of LLG equation.

$$\frac{dS_i}{dt} = \frac{1}{i\hbar}\left[S_i, \mathscr{H}\right] = \frac{g\mu_B}{i\hbar}\left[S_i, S_j\right]H_j = \frac{g\mu_B}{\hbar}\varepsilon_{ijk}S_k H_j. \qquad (2\text{-}1)$$

The atomic moment in a cell can be written as $\mathbf{M} = n\mu = -ng\mu_B \mathbf{S}$, where n is the atomic density. Based on Eq. (2-1), if the energy is conserved, we have,

$$\frac{d\mathbf{M}}{dt} = -ng\mu_B \frac{d\mathbf{S}}{dt} = -g\frac{e}{2mc}(\mathbf{M}\times\mathbf{H}) = -\gamma_0(\mathbf{M}\times\mathbf{H}), \qquad (2\text{-}2)$$

where the constant $\gamma_0 = ge/2mc$ is the gyromagnetic ratio for an atomic spin. For the ferromagnetic alloys of Fe, Co, Ni transition metal elements, due to the quenching of the orbital angular momentum of d-electrons, the g-factor of the atomic spin is usually just the g = 2 of an electron. When the dissipation of magnetic free energy is included, the calculation of atomic spins is based on a non-equilibrium statistics, and their motion becomes nonlinear. Based on the Hamiltonian $\mathscr{H} = -\mu_a \cdot \mathbf{H}$, the dissipation of magnetic energy means the moment $\mathbf{M}$

will rotate to the direction of the local magnetic field **H**, which equals the effective magnetic field $\mathbf{H}_{eff}$ as shown in Fig. (2-2). Therefore Landau and Lifshitz added a damping term in the equation of the motion of the spin, and created the famous LL equation. In micromagnetics, the equation of motion for magnetic moments is always called the LLG equation, because the American scientist Thomas Gilbert explained the damping term of the LL equation by the dissipative Lagrange equation with a Rayleigh's dissipation function in 1955 [2]:

$$\frac{d\mathbf{M}}{dt} = -\gamma(\mathbf{M}\times\mathbf{H}_{eff}) + \alpha\mathbf{M}\times\frac{d\mathbf{M}}{dt}. \qquad (2\text{-}3)$$

Here, γ is the gyromagnetic ratio for FM, and α is Gilbert damping constant. The first term in this equation expresses the field term as shown in Fig. 2-2 (green arrow), the second term, which is the damping term, expresses the damping torque (red arrow in Fig. 2-2).

2.3 Ferromagnetic resonance (FMR)

If we apply a microwave onto FM with magnetization, the magnetization of FM will precess along the external magnetic field H. The ferromagnetic resonance means sweeping H to H_{FMR}; the damping torque is suppressed by the microwave, and only the field term in LLG equation works. At this time, the magnetization rotates around the external magnetic field by angular frequency ω, and the motion of magnetization becomes,

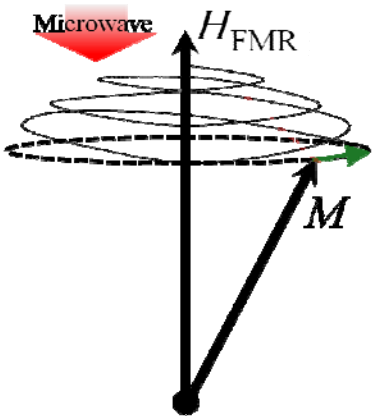

Figure 2-3. FMR condition.

$$\frac{dM}{dt} = -\gamma(M\times H_{eff}), \qquad (2\text{-}4)$$

in which, H_{eff} is described as the sum of external magnetic field and the demagnetizing field (H_d) in FM. Based on the definition of the demagnetizing factors N_x, N_y, N_z, we have,

$$H_d = (H_{dx}, H_{dy}, H_{dz}) = (\frac{N_x}{\mu_0}M_x, \frac{N_y}{\mu_0}M_y, \frac{N_z}{\mu_0}M_z). \qquad (2\text{-}5)$$

The external magnetic field can be expressed as,

$$H = (-\frac{N_x}{\mu_0}M_x, -\frac{N_y}{\mu_0}M_y, H_0 - \frac{N_z}{\mu_0}M_z). \qquad (2\text{-}6)$$

For the solution of Eq.(2-4) using Eq.(2-6), we have,

$$\omega_0^2 = \gamma^2 \left\{ H_0 + \frac{1}{\mu_0}(N_x - N_z)M \right\} \left\{ H_0 + \frac{1}{\mu_0}(N_y - N_z)M \right\}, \qquad (2\text{-}7)$$

in which the demagnetizing factors are determined by the shape of the FM, i.e., the FMR is dependent on the shape of the FM. In this study, the external magnetic field is applied in plane, so we have the following FMR condition:

$$\omega^2 = \gamma^2 H_{FMR}(H_{FMR} + \frac{M}{\mu_0}). \qquad (2\text{-}8)$$

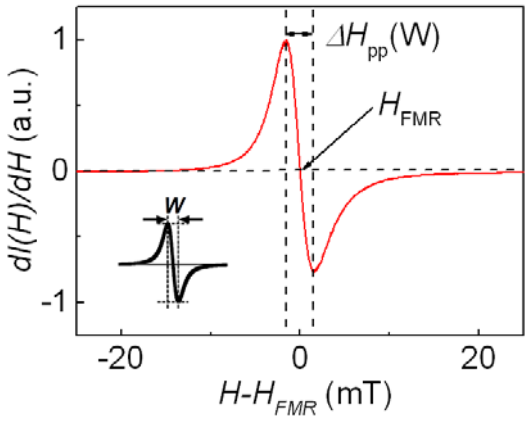

Figure 2-4. An example of FMR spectrum.

The typical spectrum of FMR is shown in Fig. (2-4), which is the first derivative of the absorption curve. ΔH_{PP} is the linewidth of the spectrum, which is related to the damping constant α. The modulation of the linewidth corresponds to the change of spin angular momentum. H_{FMR} is the magnetic field at the resonance point. The damping is suppressed at this point and the magnetization only rotates around the external magnetic field.

2.4 Spin pumping

For a FM/NM bilayer structure, microwave induces the FMR in FM and forces the continuous precession of magnetization. At this time, the time average of the precession magnetization amplitude is smaller than that of the amplitude without microwave (see Fig. 2-5). Due to the spin angular momentum conservation, part of this loss

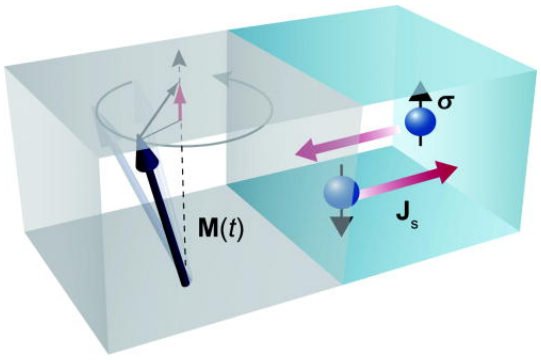

Figure 2-5. A schematic illustration of the spin pumping. From Ref.[3].

of magnetization corresponding to the spin angular momentum must be transferred to the adjacent layer. This transferred spin angular momentum induces spin accumulation at the FM/NM interface and generation of pure spin current in NM. Note that there is no charge flow in the materials, only spin angular momentum is conserved and pure spin current is generated.

On the FM side, at the resonance point, the field angle between the magnetization and the external magnetic field is the largest and the most stable. The linewidth changes when an adjacent layer of the NM is connected to the FM. The spin current is generated in the NM due to the spin pumping, a process which is revealed by the modulation in the linewidth of FMR spectrum. In other words, the realization of spin pumping can be determined by the modulation of linewidth (W).

The spin pumped into an adjacent layer by a precessing magnetic moment is given by [2],

$$\frac{dM}{dt} = -\gamma(M \times H_{eff}) + \frac{\alpha}{M_s} M \times \frac{dM}{dt}, \qquad (2\text{-}9)$$

in which M_s is the saturation magnetization. The magnetization precession drives the spin pumping into the NM layer. The dc component of a generated spin current at the interface is expressed as,

$$j_s^0 = \frac{\omega}{2\pi}\int_0^{2\pi/\omega} \frac{\hbar}{4\pi} g_r^{\uparrow\downarrow} \frac{1}{{M_s}^2}\left[M(t) \times \frac{dM(t)}{dt} \right] dt, \qquad (2\text{-}10)$$

where $g_r^{\uparrow\downarrow}$ and $\hbar$ are the real part of the mixing conductance of the FM/NM interface and the Dirac constant, respectively. The real part of the mixing conductance indicates the spin pumping efficiency of the direction from FM to NM. Also, $g_r^{\uparrow\downarrow}$ is given by [3],

$$g_r^{\uparrow\downarrow} = \frac{2\sqrt{3}\pi M_s \gamma d_F}{g\mu_B \omega}(W_{F/N} - W_F). \qquad (2\text{-}11)$$

Here, g is g-factor, μ_B is the Bohr magneton, and d_F is the thickness of the FM layer. From Eqs. (2-9)-(2-11), the spin current density at the FM/NM interface is obtained as,

$$j_s = \frac{g_r^{\uparrow\downarrow}\gamma^2 h^2 \hbar \left[4\pi M_s + \sqrt{(4\pi M_s)^2\gamma^2 + 4\omega^2} \right]}{8\pi\alpha^2 \left[(4\pi M_s)^2\gamma^2 + 4\omega^2 \right]}, \qquad (2\text{-}12)$$

where h is the amplitude of the microwave magnetic field. In this study, it is set to 0.16 mT at a microwave power of 200 mW.

2.5 Inverse spin Hall effect (ISHE)

The spin Hall effect (SHE) and the inverse spin Hall effect (ISHE), have recently attracted a lot of attention due to the realization of the conversion between charge current and spin current. Spins are scattered in the vertical direction by the spin-orbital interaction. The Hamiltonian of the spin-orbital interaction is proportional to the 4th order of atom number Z [4]. It can be omitted in light atoms (eg. Hydrogen, Carbon), but can not be ignored in heavy metals such as Pd and Pt. Therefore, it is natural to expect ISHE in heavy metals.

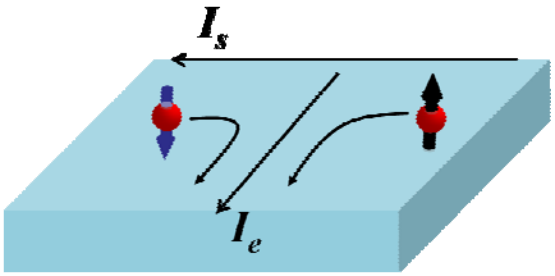

Figure 2-6. A schematic view of ISHE.

Figure 2-6 shows an illustration of ISHE for a spin current. The up-spin and down-spin travel in opposite directions, and both of them are scattered to the vertical direction of the spin current due to the spin-orbital interaction. This defluxion induces a charge current in the transverse direction. Thus, the spin current is converted to a measurable charge current via ISHE, enabling electric detection of the spin current.

Moreover, the ISHE is expressed as [5],

$$\vec{J}_c = \theta_{SHE}\left(\frac{2e}{\hbar}\right)\vec{J}_c \times \vec{\sigma}. \qquad (2\text{-}13)$$

Here, θ_{SHE} and σ are the spin Hall angle of the material and the spin vector, respectively. The physical meaning of θ_{SHE} is the intrinsic ISHE conversion efficiency of materials. It should be noted that the output charge current is proportional to the outerproduct of the spin current and spin vector, and the direction of the charge current will be inversed if the external magnetic field turns to the opposite direction.

The ISHE was recently observed using a spin pumping method operated by ferromagnetic resonance [3].

Since it enables the electric detection of a pure spin current, it is useful for exploring spin currents in condensed matter. The output voltage from the converted electric current can be observed by the theoretical calculations shown below.

First, we consider a bilayer structure of Pd/FM. The spins are pumped from the FM due to the modulation of the magnetization precession. As shown in Fig. 2-17, j_s is generated along the -y direction. The spin current which decays in heavy metal Pd is expressed as,

$$j_s(y) = \frac{g_r^{\uparrow\downarrow}\gamma^2\hbar^2\hbar[(d_N - y)/\lambda_N]}{\sinh(d_N/\lambda_N)} j_s. \qquad (2\text{-}14)$$

Here, d_N and λ_N are the thickness and the spin diffusion length of Pd. Spin current is converted to a charge current due to the ISHE,

$$j_c(y) = \theta_{SHE}(2e/\hbar) j_s(y). \qquad (2\text{-}15)$$

The spin current density is,

$$\begin{aligned} \langle j_c \rangle &= (1/d_N)\int_0^{d_N} j_c(y)dy \\ &= \theta_{SHE}\left(\frac{2e}{\hbar}\right)\frac{\lambda_N}{d_N}\tanh\left(\frac{\lambda_N}{2d_N}\right) j_s. \end{aligned} \qquad (2\text{-}16)$$

To consider an equivalent circuit as shown in Fig. 2-8 [3], the observed output voltage from ISHE is given by,

$$V_{ISHE} = \frac{R_F R_N}{R_F + R_N} Ic = w\left[\sigma_N + \frac{d_F}{d_N}\sigma_F\right]^{-1} \langle j_c \rangle, \qquad (2\text{-}17)$$

where R_F, R_N, w, σ_F and σ_N are the resistance, width, and conductivities of the FM and the NM, respectively.

The output electromotive force due to the ISHE by spin pumping is shown as,

$$V_{ISHE} = \frac{w\theta_{SHE}\lambda_N \tanh(d_N/2\lambda_N)}{d_N\sigma_N + d_F\sigma_F}\left(\frac{2e}{\hbar}\right) j_s. \qquad (2\text{-}18)$$

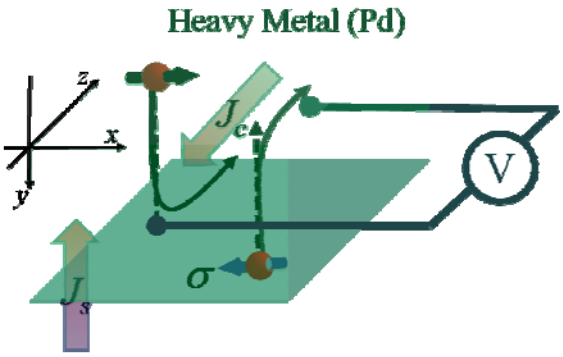

Figure 2-7. A schematic view of ISHE.

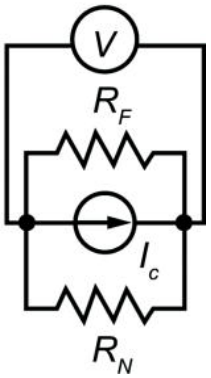

Figure 2-8. The equivalent circuit of ISHE. From Ref. [3].

2.6 Sample structure for spin transport

The sample structure is shown in Fig. 2-9. We fabricated the Py layer and Pd wire onto SLG (with SiO_2 substrate). Py is used for spin injection by magnetization dynamics, while Pd is used for its ISHE due to large spin-orbital interaction. The spins are injected (pumped) from Py to the interface of SLG, then the spin accumulation induces spin diffusion in SLG, and one side of the diffused spins can be absorbed by the Pd wire due to the ISHE. The generated charge current can be detected by a voltmeter. In other words, the spin transport in SLG is achieved if the voltage of ISHE can be observed.

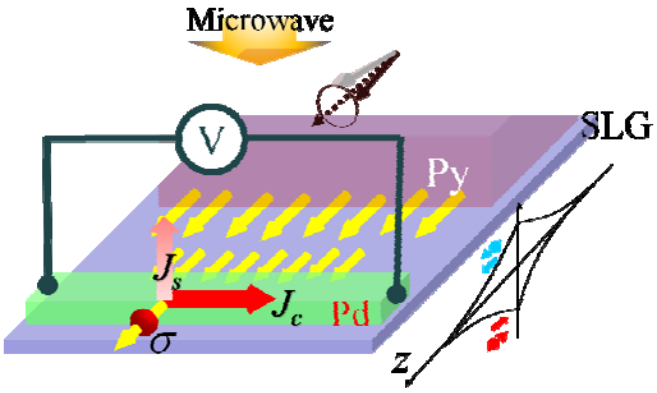

Figure 2-9. Sample design for realization of spin transport in SLG by magnetization dynamics.

Since we changed the structure from pumping/ISHE mode to pumping/transport/ISHE mode, the applicability of existing equations needs more consideration. The main difference comes from the pumping site. In the conventional case, the pumped spin current density is uniform at the interface, and this uniform spin current is generated to the charge current by ISHE (see right figure in Fig. 2-10). In the case of the structure with spin transport, the spin current density arrives at the Pd site from different gaps, as shown in the left figure of Fig.2-10, but the typical spin diffusion length of SLG is around 2 μm. The gaps between Py and Pd are designed to be ca. 1 μm, so almost all detected spins come from the area around the edge of the Py facing Pd, as shown in Fig. 2-10 (red arc area). Thus, the existing

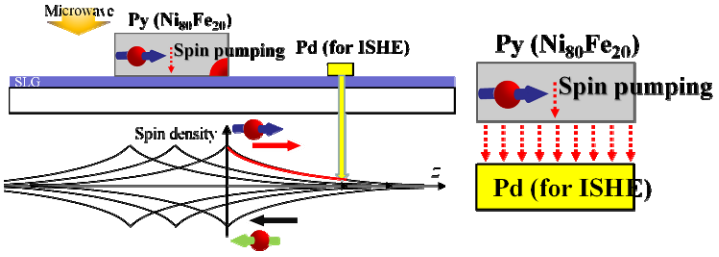

Figure 2-10. Comparison of spin pumping/ISHE with and without spin dissipation.

formulas are still applicable to the spin transport case, and the spin diffusion area is the gap between Py and Pd. On the other hand, the spin diffusion length is estimated by the decaying exponential function, and the contribution from the area that is away from the Pd edge is quite limited. So far in the discussion of this study, the estimated value of the spin diffusion of SLG is slightly shorter than the real value.

2.7 Fabrication procedures

The graphene samples on SiO_2 have been fabricated by Ago's group from Kyushu University by using the CVD method. The fabrication procedures of pumping/SLG/ISHE samples are shown below.

1. Clean graphene samples by acetone and 2-proponal (IPA)

   Acetone is used for cleaning; it dissolves almost all organic compounds. IPA is for removing acetone residue. We avoid using the ultrasonic cleaner for graphene as it is partly destructive for the graphene layer.

2. EB lithography (EB litho.) for "+" marks

   Spin coating by PMMA/MMA bilayer resist, 1000rpm, 5s, 4000rpm, 60s

   Bake on hotplate, MMA 150℃, 90s, 170℃, 20min (15min is also enough, no obvious difference)

   EB litho. by Elionix ELS-3700 (vacuum → FC→ current → MK → focus → exposure, 1mm chip size, 20000 dot)

   Condition: 1 nA, Dose: 2.35 μsec/dot

   (Dose: adjust the quantity of charge by exposing time)

   Develop: ZED-N50 (2min 30s), rinse by IPA (30s)

Figure 2-11. The EB lithography system. Sample room (left) and the control unit (right).

3. EB evaporation for “+” marks

   By i-Quick, Cr (5 nm)/Au (100 nm)

   Rate: Cr: 0.2~0.3 Å/s, Au: 1.0 Å/s

   Lift-off: by ZDMAC (vibration stage until resist is peeled, one or two hours), clean by acetone & IPA

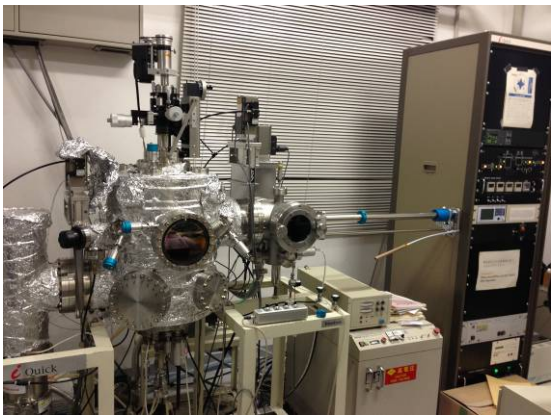

Figure 2-12. i-Quick system. Cr and Au can be evaporated in this system.

4. EB litho. for Pd wire

   Same with step-2 for the wide part of Pd

   For the narrow part of Pd, condition: 20 pA, Dose: 230 μsec/dot (check it when condition is bad)

5. EB evaporation for Pd

   By ODA-8300, Pd (5 nm)

   Rate: 0.3~0.4 Å/s

   Lift-off: by ZDMAC (by vibration stage until resist is peeled, one or two hours), clean by acetone & IPA

(For control experiment of Py/SLG/Cu, perform step 4 & 5 for Cu (5 nm), and evaporate in MBE)

Figure 2-13. A picture of ODA-8300 system. Py, Pd, Al can be evaporated in this

6. EB litho. for Pd wire

   Use the same marks with Pd wires if possible.

   Procedures are the same with step 2.

7. EB evaporation for Py

   By ODA-8300, Py (25 nm)/Al (4nm)

   Rate: 0.3~0.4 Å/s

   Lift-off: by ZDMAC (vibration stage until resist is peeled, one or two hours), clean by acetone & IPA.

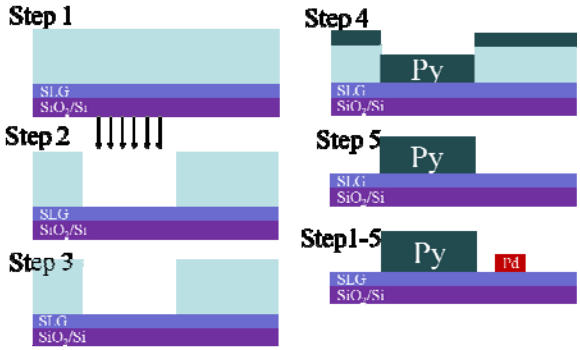

Figure 2-14 EB litho procedures and lift-off techniques.

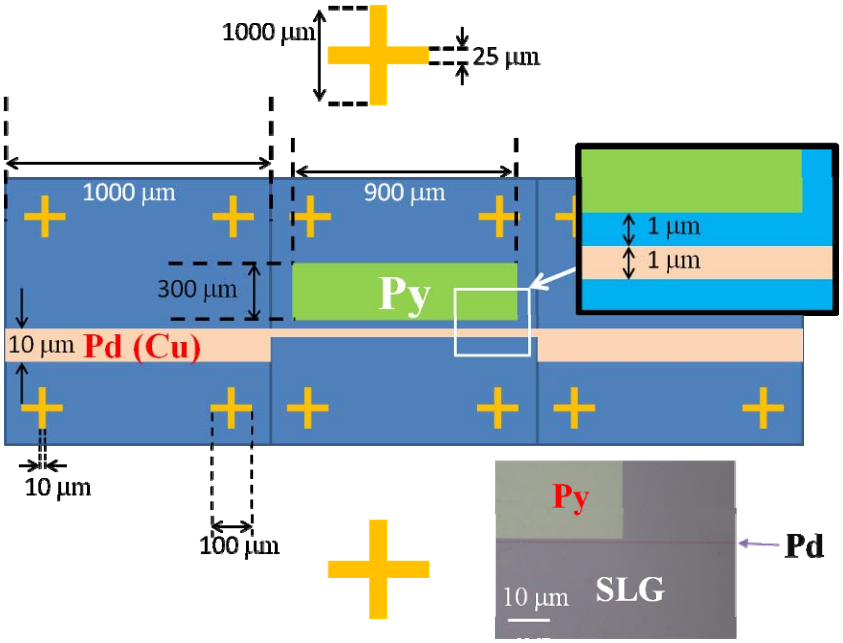

Figure 2-15. Sizes for patterns, marks and chips and a microscope image of sample

2.8 Experimental setup

Electron spin resonance (ESR) system

We used two types of ESR equipment for measurement (Bruker EMX 10/12 TE_{102} cavity and JEOL TE_{011} cavity). Their resonance fields are slight different (ca. 9.62 GHz for Bruker system, ca. 9.12 GHz for JEOL system). Studies at RT can be carried out in Bruker system, the JEOL is available to modulate temperature from -170℃ to 200℃. We sweep the external magnetic field around resonance field by applying certain high frequency magnetic field. The FMR occurs when the system is at FMR

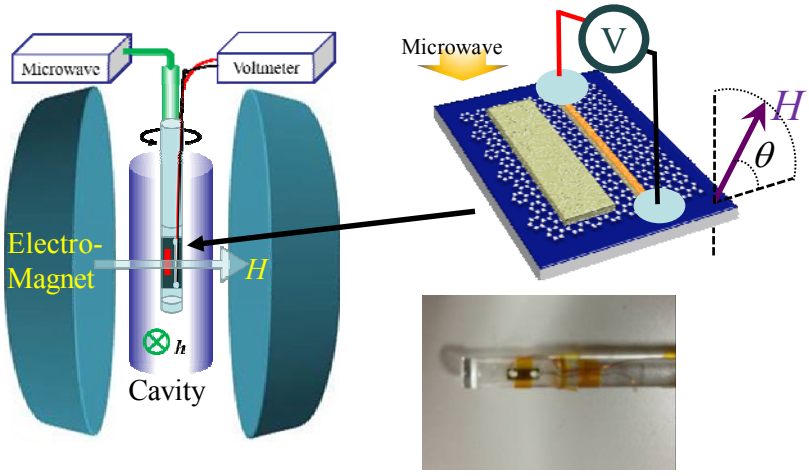

Figure 2-16. The measurement setup of ESR equipment.

condition. Spins will be injected from FM to NM at resonance point. The spins in Pd are converted to a detective charge current and calculate the spin diffusion in SLG (Chapter 3) and spin Hall angle in Pd (Chapter 4). We also change the direction of external magnetic field as shown in Fig. 2-16 by a goniometer, the FMR field also shifts with the changing of the angle due to the magnetic anisotropy in the ferromagnetic material; and the details will be shown in Chapter 3. Other measurements are briefly shown below.

1. Optical microscope, for checking the patterns, taking photographs of samples. The magnification of this optical microscope is 50, 100, 200, 500 and 1000.
2. Nano voltmeter (KEITHELEY), for the detection of the output voltage from the Pd wire due to ISHE.
3. 4-terminal prober system
4. Semiconductor parameter system. 3 and 4 are used for field-effect-transistor (FET) measurement.
5. Setup for measurement of graphene FET

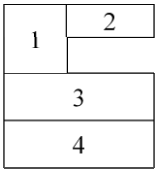

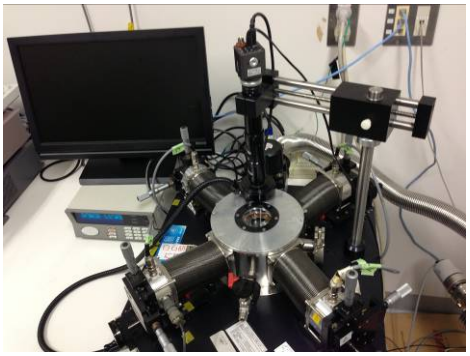

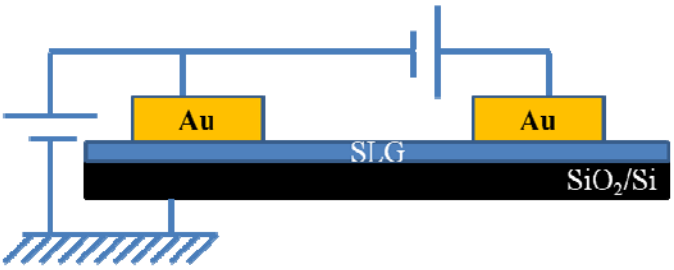

Figure 2-17. The instruments for measurements and the measurement setup for FET characteristics.

References

[1] L.D. Landau, E. Lifshitz, On the theory of the dispersion of magnetic permeability in ferromagnetic bodies. Phys. Zeitsch. der Sow. 8, 153 (1935), reprinted in English by Ukr. J. Phys. 53, 14 (2008).

[2] T.L Gilbert, IEEE Trans.Magn. **40** (6), 3443–3449 (2004).

[3] K. Ando and E. Saitoh, J. Appl. Phys. **108,** 113925 (2010).

[4] M. Shiraishi and T. Ikoma, Physica E **43,** 1295 (2011).

[5] H. Nakayama and K. Ando, Phys. Rev. B **85**, 144408 (2012).

Chapter 3

Dynamically-generated pure spin current in single-layer graphene*

Abstract

In this section, I introduce an approach which enables the generation of pure spin current into single-layer graphene (SLG), free from electrical conductance mismatch by using dynamical spin injection. Experimental demonstration of spin-pumping-induced spin current generation and spin transport in SLG at room temperature was successfully achieved with our method, and the spin coherence length was estimated to be 1.36 μm by using a conventional theoretical model based on the Landau-Lifshitz-Gilbert equation. The spin coherence length is proportional to the quality of SLG, which indicates that spin relaxation in SLG is governed by the Elliot-Yafet mechanism, as previously reported.

---

*Published as: Z. Tang, E. Shikoh, H. Ago, K. Kawahara, Y. Ando, T. Shinjo and M. Shiraishi,

Phys. Rev. B 87, 140401(R) (2013)

3.1 Experimental details

The SLG used in this study was a large-area SLG grown by chemical vapor deposition (CVD). The SLG was transferred to a SiO_2/Si substrate (300 nm thick SiO_2; and the details are described elsewhere [1]). Figure 3-1(a) shows a schematic image of the sample used in this study. A 25-nm-thick, 900 × 300 μm^2 rectangular shape $Ni_{80}Fe_{20}$ film (Py) and a 5-nm-thick and 1-μm-wide Pd wire were fabricated by using electron beam lithography and an evaporation method. An Al capping layer was evaporated onto the Py layer in order to

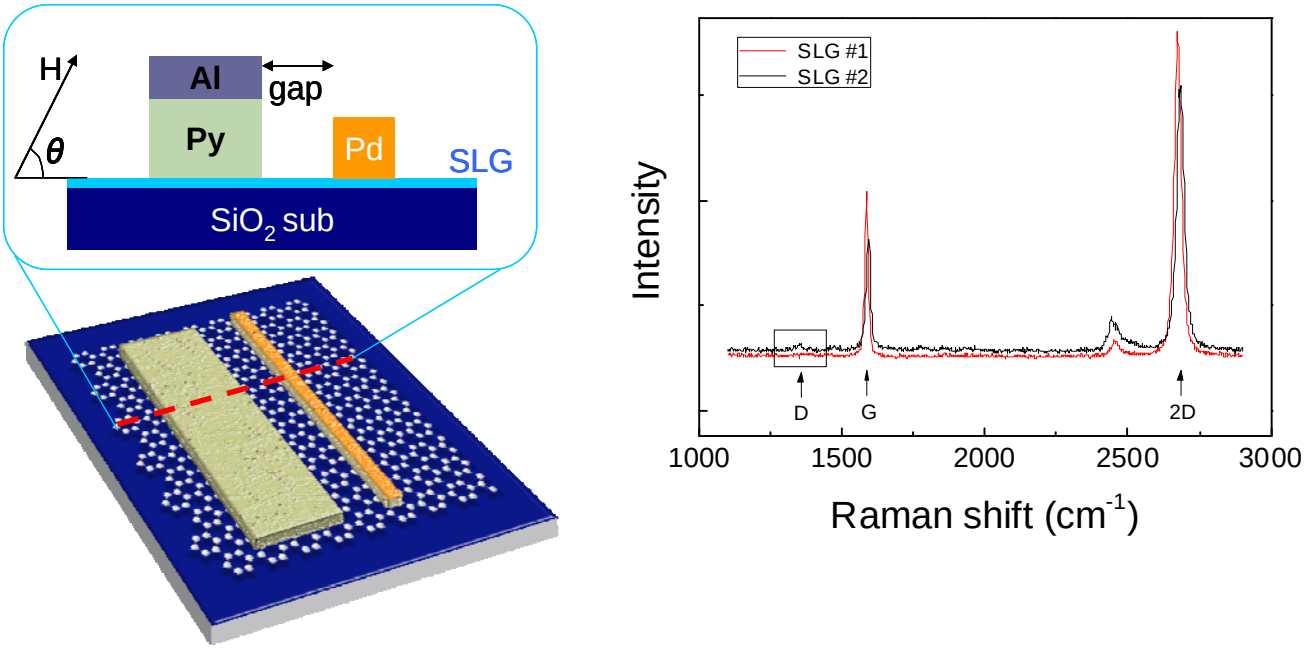

Figure 3-1. (a). A schematic image of the SLG spin pumping sample. The CVD-grown SLG is transferred to the SiO_2/Si substrate, and the Al/Py and the Pd electrodes are separately evaporated on the SLG. The angle of the external magnetic field is shown in the inset. (b). Raman spectra of the SLG just after the synthesis. The black and red solid lines are data from sample 1 and 2, respectively.

prevent oxidation of the Py. The gap length between the Py and the Pd was ca. 970 nm. Two electrodes are attached to both ends of the Pd wire by silver paste. The *I-V* curve is linear, indicating an Ohmic contact in the interface. An external magnetic field was applied by changing the angle θ, as shown in Fig. 3-1(a) (θ is equal to 0° when the magnetic field is parallel to the SLG plane). Figure 3-1(b) shows the typical Raman spectra of the

SLGs, obtained by using a Raman spectrometer (Tokyo Instrument, Nanofinder30). We prepared two different qualities of the SLGs (sample 1 and 2). Sample 1 has less defects than sample 2, since the D-band can be observed only from sample 2 (see Fig. 3-1(b)). Furthermore, we clarified that they are SLGs by measuring the transport characteristics.

3.2 Results and discussion

3.2.1 Enhancement of FMR spectrum

Figure 3-2 shows the FMR spectra of the Py with and without the SLG/Pd. The line width of the spectrum

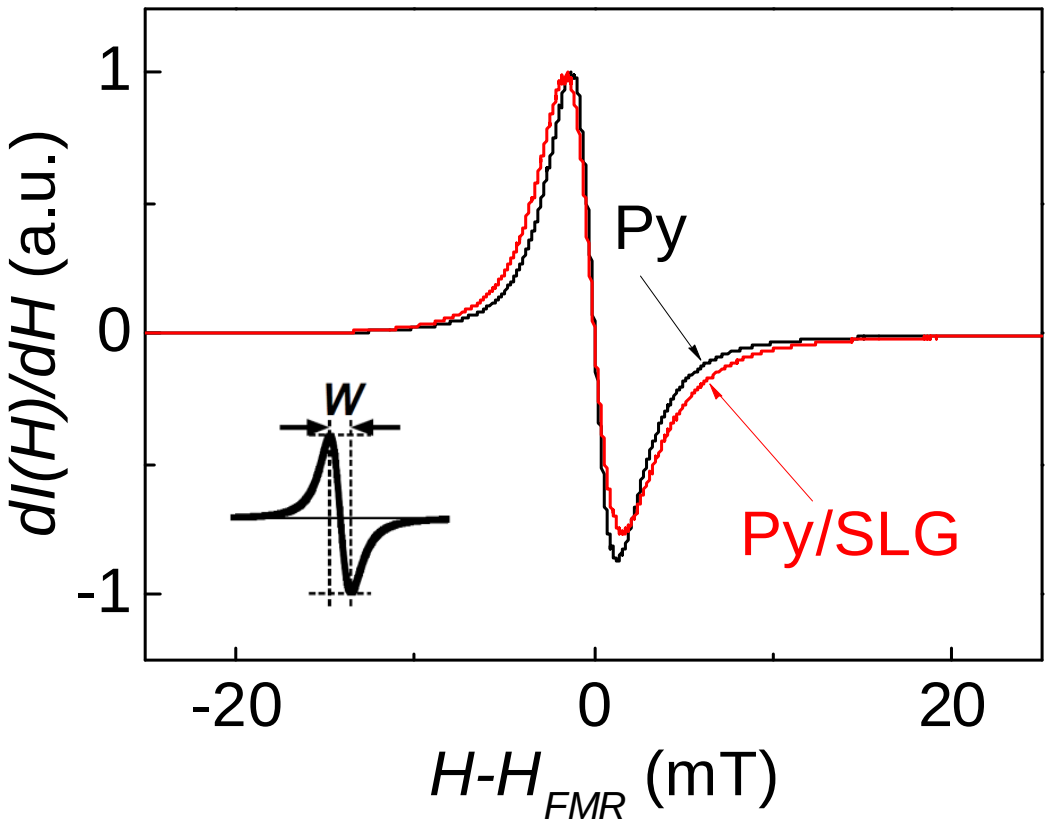

Figure 3-2. FMR spectra of the Py on the SiO_2 substrate (a black solid line) and the Py/SLG on the SiO_2 substrate (a red solid line, sample 1). An increase of the line width can be seen, which is attributed to a shift of the Gilbert damping constant, α, namely, spin pumping into the SLG.

from the sample with the SLG/Pd is larger than that without the SLG/Py, a fact which is attributed to the modulation of α, due to successful spin pumping into the SLG/Pd. Spin coherence in the experiment is estimated based on the conventional spin pumping theory described in Chapter 2. The real part of mixing conductance $g_r^{\uparrow\downarrow}$ is given by,

$$g_r^{\uparrow\downarrow} = \frac{2\sqrt{3}\pi M_s \gamma d_F}{g\mu_B \omega}(W_{Py/SLG} - W_{Py}), \qquad (3\text{-}1)$$

where g, μ_B and d_F are the g-factor, the Bohr magneton and the thickness of the Py layer, respectively, and, d_F, $W_{Py/SLG}$ and W_{Py} in this study were 25 nm, 3.10 mT and 2.57 mT, respectively. The spin current density at the Py/SLG interface is obtained as,

$$j_s = \frac{g_r^{\uparrow\downarrow}\gamma^2 h^2 \hbar[4\pi M_s\gamma + \sqrt{(4\pi M_s)^2\gamma^2 + 4\omega^2}]}{8\pi\alpha^2[(4\pi M_s)^2\gamma^2 + 4\omega^2]}, \quad (3\text{-}2)$$

where h is the microwave magnetic field, set to 0.16 mT at a microwave power of 200 mW. As discussed above, the broadening of W in the Py/SLG compared with that in the Py film was attributed to spin pumping into the SLG. $g_r^{\uparrow\downarrow}$ in the Py/SLG layer was calculated to be 1.6×10^{19} m^{-2}, and thus j_s was calculated to be 7.7×10^{-9} Jm^{-2}. Here, half of the generated j_s can contribute to the electromotive force in the Pd electrode in our device geometry, since a pure spin current diffuses isotropically as shown in Fig. 2-10 in Chapter 2. The generated j_s decays by spin diffusion in SLG, i.e., it decays to $j_s \cdot \exp(-\frac{d}{\lambda})$ when the spins diffuse to the Pd wire. Furthermore, taking into account the spin relaxation in the Pd wire the electromotive force can be written as,

$$V_{ISHE} = \frac{w\theta_{SHE}\lambda_{Pd}\tanh(d_{Pd}/2\lambda_{Pd})}{d_{SLG}\sigma_{SLG} + d_{Pd}\sigma_{Pd}}(\frac{2e}{\hbar})j_s, \quad (3\text{-}3)$$

in the simplest model. Here, w, λ_{Pd}, d_{Pd} and σ_{Pd} are the length of the Pd wire facing the Py (900 nm), the spin diffusion length (9 nm) [2], the thickness (5 nm) and the conductivity of the Pd, respectively, and d_{SLG} and σ_{SLG} are the thickness (assumed to be ca. 0.3 nm) and conductivity of the SLG (measured to be ca. 3.10×10^6 S/m under the zero gate voltage application. See section 3.3.6). The spin-Hall angle in a Py/Pd junction, θ_{SHE}, has been reported to be 0.01 [3], which allows us to theoretically estimate the electromotive force in the Pd wire as

2.37×10^{-5} V if no spin dissipation occurs in the SLG.

3.2.2 Spin transport in SLG by spin pumping

Figures 3-3 (a)-(c) show the FMR signals as functions of θ, where the FMR of the Py occurs in every condition. The electromotive force of the Pd wire is shown in Figs. 3-3 (d)-(f), where the electromotive force is observed when θ is set to be 0° and 180°, but no signal is observed at θ = 90°. Since this finding is in

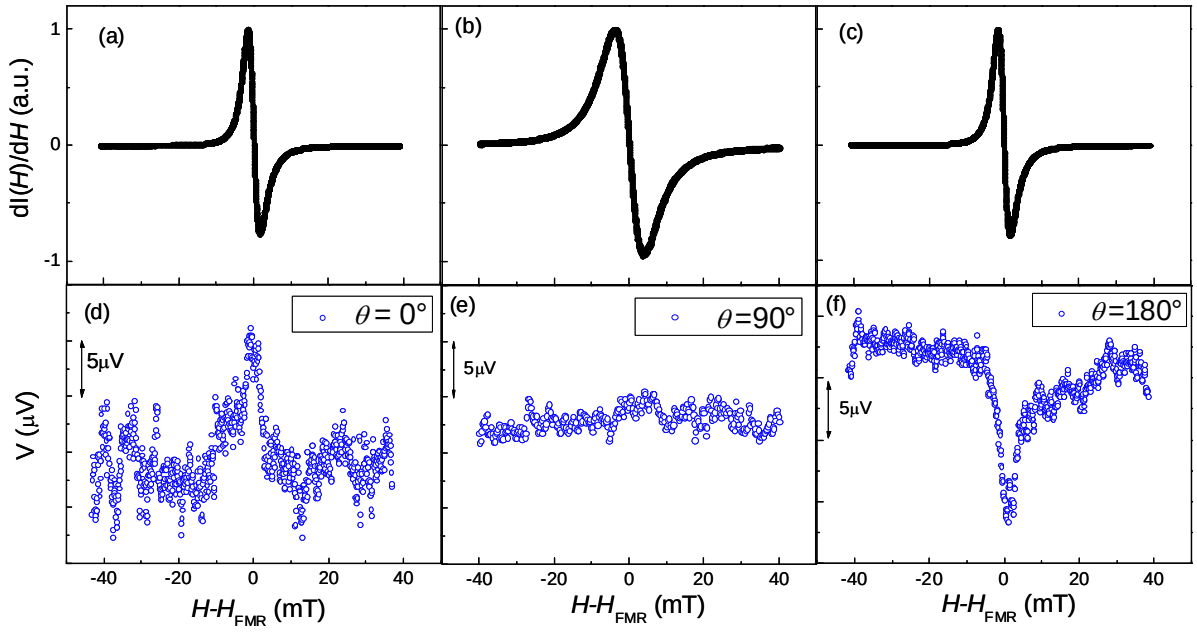

Figure 3-3. Results on spin pumping and spin transport in sample 1. (a)-(c) Ferromagnetic resonance spectra of the Py under external magnetic field at (a) 0°, (b) 90° and (c) 180° under the microwave power of 200 mW. (d)-(f) Electromotive forces from the Pd wire on the SLG when θ is set to be (d) 0°, (e) 90° and (f) 180° under the microwave power of 200 mW.

accordance with the angular dependence of the electromotive force due to the ISHE ($J_c \sim J_s \times \sigma$), the observed electromotive force is ascribed to the ISHE of the Pd, which is due to spin pumping into the SLG and the achievement of spin transport for a dynamically generated pure spin current at room temperature. Note that there is no spurious effect with the observed symmetry, and only the ISHE possesses symmetry. For example, the anomalous Hall effect (AHE) signal can be included as a spurious signal, which may impede detection of

the ISHE signals, but the AHE does not show external magnetic field dependence of the electromotive force. The following investigations also support the result that the ISHE signals were dominantly observed. The theoretical fitting was performed in order to separate the ISHE and the AHE signals in the observed electromotive force by using the following equation [4]:

$$V = V_{ISHE}\frac{\Gamma^2}{(H-H_{FMR})^2+\Gamma^2} + V_{AHE}\frac{-2\Gamma(H-H_{FMR})}{(H-H_{FMR})^2+\Gamma^2} + aH + b, \quad (3\text{-}4)$$

where V_{ISHE} is the electromotive force, V_{AHE} is the voltage due to the AHE, H is an external static magnetic field for the FMR, H_{FMR} is the magnetic field where the FMR occurs, with values of 107.7 mT at 0° and 180°, and 1084.5 mT at 90°. Γ, a, b are fitting parameters. An example of the fitting is shown in Fig. 3-4, and V_{ISHE} and

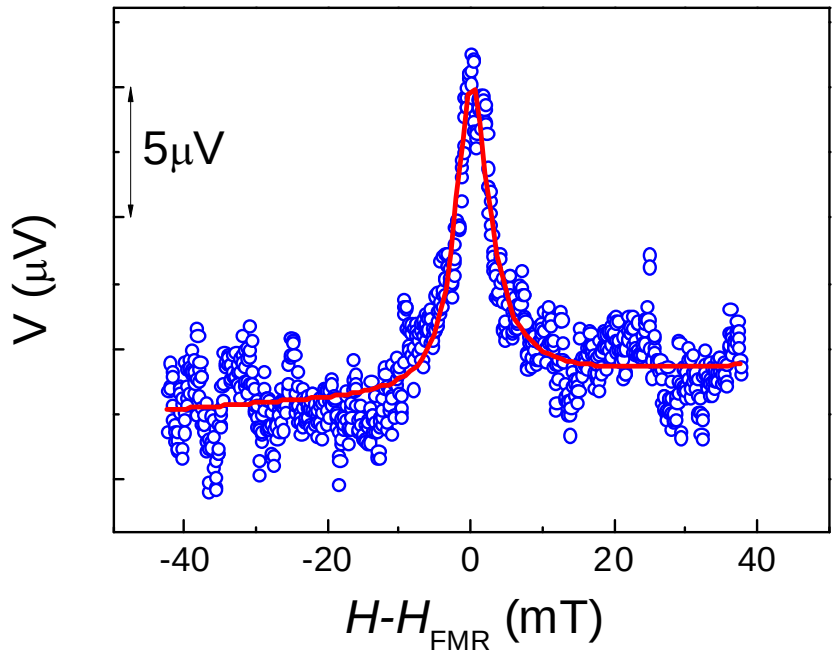

Figure 3-4. Results of the analysis of the contribution from the electromotive force due to ISHE and AHE. The open circles represent the external magnetic field dependence of ΔV for sample 1, where $\Delta V = \left[V(\theta = 0^\circ) - V(\theta = 180^\circ)\right]/2$ in order to eliminate the heat effect during measurement. The solid line is the fitting line, which is calculated by using Eq. (3-4).

V_{AHE} are estimated to be 1.16×10^{-5} V and 6.67×10^{-7} V, respectively. The contribution from the AHE to the electromotive force by the ISHE was very weak. The theoretically estimated electromotive force in the Pd wire

was 2.37×10^{-5} V if no spin relaxation occurred in the SLG. In contrast, the experimentally observed electromotive force was 1.16×10^{-5} V. This discrepancy is ascribed to dissipation of spin coherence during spin transport in the SLG (the decay of j_s), which can be described as an exponential damping dependence on the spin transport. From the above calculations, the spin coherence length in the SLG is estimated to be 1.36 μm.

3.2.3 Comparison with defective sample (sample 2)

For comparison, we carried out the same experiments on sample 2 with a gap length of 780 nm, whose quality is not as good as that of sample 1 (the conductivity was measured to be 6.40×10^{5} S/m under the zero

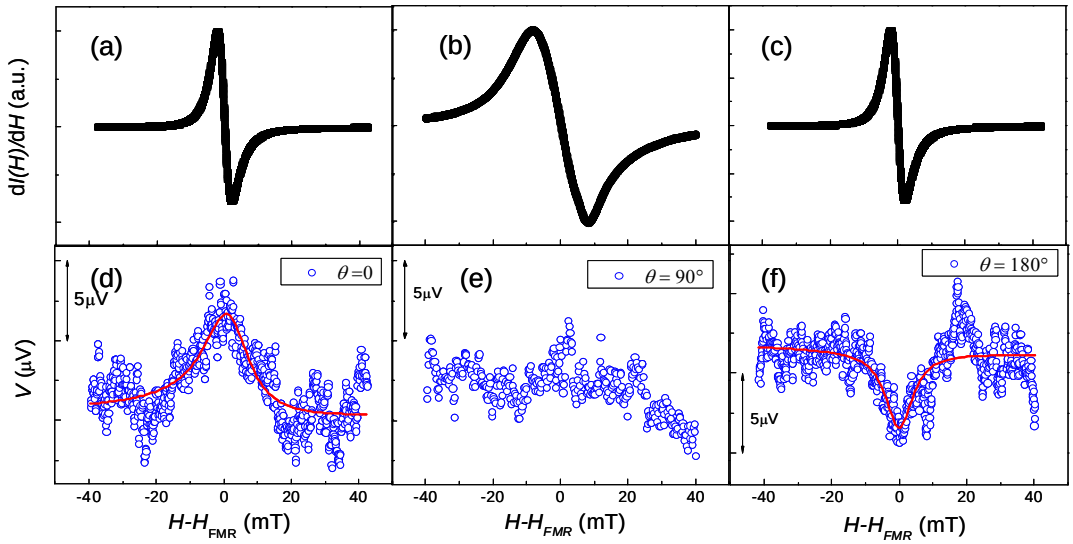

Figure 3-5. Results on spin pumping and spin transport in sample #2. (a)-(c) Ferromagnetic resonance of the Py under θ is set to be (a) 0°, (b) 90° and (c) 180° under the microwave power of 200 mW. (d)-(f) Electromotive forces from the Pd wire on the SLG when θ is set to be (d) 0°, (e) 90° and (f) 180° under the microwave power of 200 mW. Electromotive forces can be observed as expected, indicating successful dynamical spin injection. However, the signal was weak and noisy. The red solid lines in (d) and (f) show the fitting lines obtained by using Eq. (3, 4).

gate voltage application). Figures 3-5 (a)-(f) show the results; here, again, the obvious ISHE signals and the inversion of the ISHE signals can be seen as the external magnetic field was reversed. However, the signals

were comparatively weak and the estimated spin coherence length was ca. 460 nm, which is in agreement with the sample qualities and also with the reported spin relaxation mechanism in SLG, i.e., the Elliot-Yafet type. These observations also corroborate with our result which is attributed to dynamical spin injection and spin transport in the SLGs. The spin coherence length in the CVD-grown SLG, which was estimated by using the dynamical method, is comparable to the previously reported value (1.1 μm) estimated by using an electrical method [5]. In contrast, the spin coherence length of the SLG in this study is much longer than that obtained in p-Si (ca. 130 nm) in our previous study [6], which directly indicates the advantage of graphene for spin transport.

3.2.4 Control experiment

In order to eliminate spurious signals such as the intrinsic inverse spin Hall effect from the Py on the SLG, we confirmed that no electromotive force was detected from the Py/SLG sample (no Pd wire was fabricated).

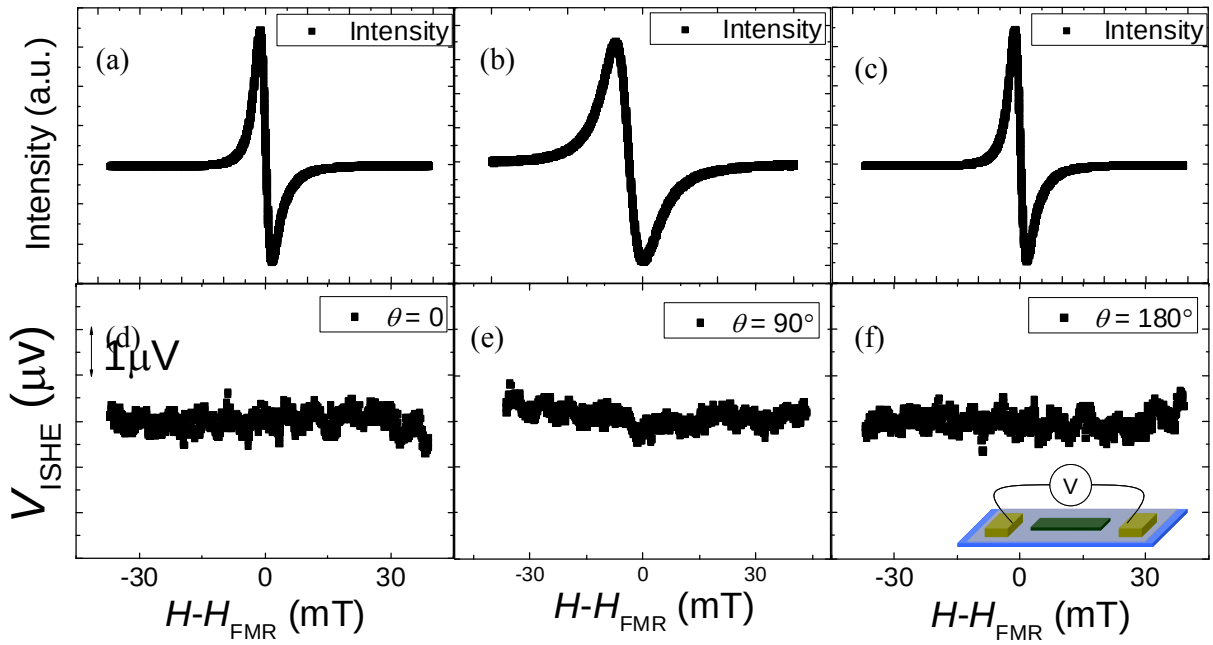

Figure 3-6. (a)-(f) Results of control experiment of Py/SLG sample. a-c) Ferromagnetic resonance spectra of the Py under the external magnetic field at a) 0°, b) 90° and c) 180° under the microwave power of 200 mW. d-f) Electromotive forces from the Pd wire on the SLG when θ is set to be d) 0°, e) 90° and f) 180°. No electromotive force was detected from the sample.

The electromotive force was measured at both edges of the SLG (see inset of Fig. 3-6), but no signal was

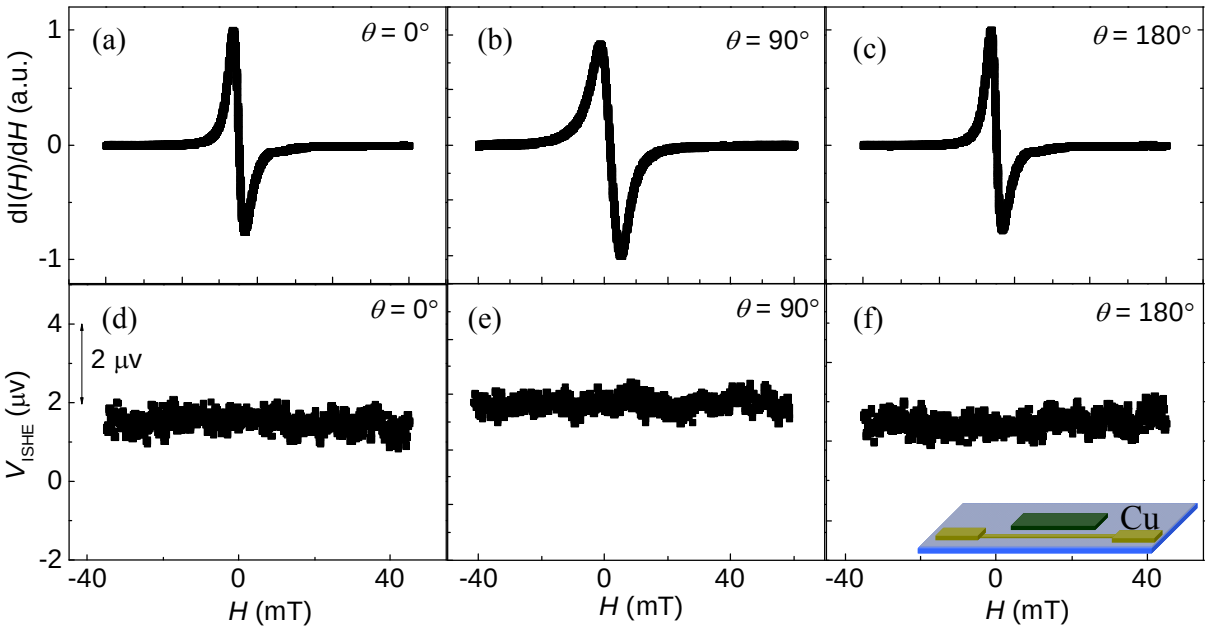

Figure 3-7. (a)-(f) Results on control experiment of the Py/SLG/Cu sample. a-c) Ferromagnetic resonance spectra of the Py under the external magnetic field at a) 0°, b) 90° and c) 180° under the microwave power of 200 mW. d-f) Electromotive forces from the Pd wire on the SLG when θ is set to be d) 0°, e) 90° and f) 180°. No electromotive force was detected from the sample.

detected. This result directly shows that the electromotive force observed in the Py/SLG/Pd sample does not come from the electromotive force from the Py itself, as reported [7]. Furthermore, we fabricated a Py/SLG/Cu sample and here again, no electromotive force was detected (see Fig. 3-7), which corroborates with our main result. These control experiment results clearly indicate that the voltage signals in Fig. 3-3 come from the ISHE in the Pd wire.

3.2.5 Power dependence of output voltage

Figure 3-8 (a) shows the microwave power dependence of the electromotive force at the Pd for the Py/SLG/Pd sample. The electromotive force at the Pd wire, V_{ISHE}, is nearly proportional to the microwave

power, which indicates that the density of the generated spin current in the SLG proportionally increases with the applied microwave power [3], which is quite consistent with Eq. (3-4) ($j_s \sim h^2$). Also, as shown in Fig. 3-8 (b), the electromotive force increases linearly with the microwave power, although the voltage due to the AHE

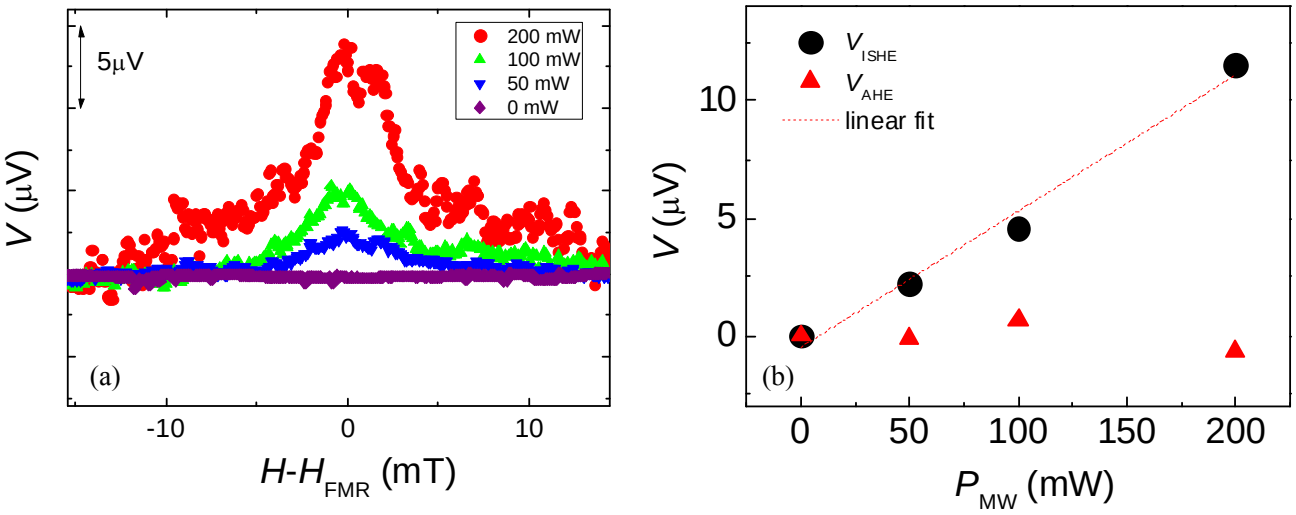

Figure 3-8. (a) Microwave power dependence of the electromotive forces in the Pd wire. A magnetic field was applied parallel to the film plane. A monotonical increase of the electromotive force can be observed. (b). Microwave power (P_{MW}) dependence of V_{ISHE} and V_{AHE} measured for the Py/SLG/Pd sample. The contributions from the ISHE (V_{ISHE}) and anomalous Hall effect (V_{AHE}) are plotted by black circles and red triangles, respectively. The dashed line shows the linear fit of the data for the V_{ISHE}.

was small. In fact, the ratio of the signal intensities due to the ISHE and AHE at 200 mW was estimated to be 17, which indicates that the ISHE signal is dominant in the observed electromotive force and that the observed signal was mainly due to spin transport in the SLG.

3.2.6 Transfer characteristics

In order to clarify whether the graphene channel was definitely formed, we measured the field-effect transistor (FET) characteristics of sample 1, and showed that typical FET features were observed (see Fig. 3-9). Here, a slight distortion in the gate voltage dependence of source-drain current was observed, which often appears in SLG-FETs with ferromagnetic contacts [8]. This FET characteristic apparently indicates that the

charge current flows in the SLG. The conductivity of the SLG is measured to be ca. 3.10×10^{6} S/m under the zero gate voltage application.

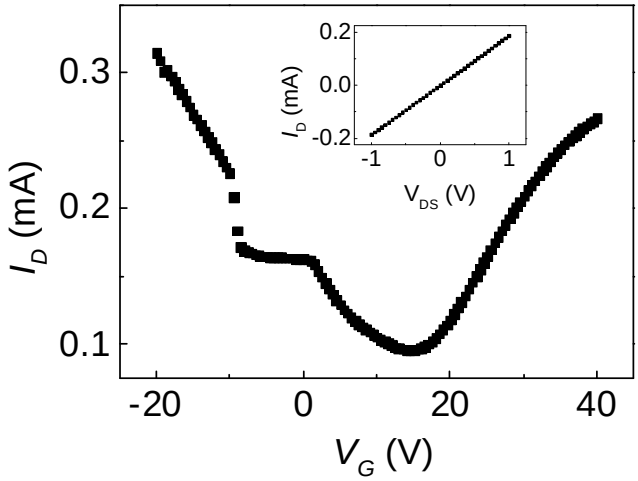

Figure 3-9. FET characteristics of SLG sample 1. The inset shows the the *I-V* curve of the source-drain current. The measurement was carried out at room temperature.

3.2.7 Gap dependence experiment

Although exponential decay of spin coherence in SLG was experimentally verified with the electrical method in previous studies, we carried out additional experiments by changing the gap length by using different SLG samples. Here, the electromotive forces from the Pd were normalized by the mixing conductance; there were slight differences in the mixing conductances of the sample. As shown in Fig.

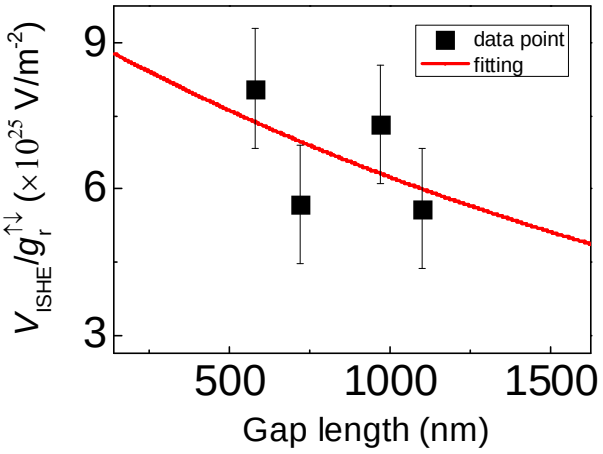

Figure 3-10. The gap dependence of the decay of the electromotive force normalized by the mixing conductance. The data points are the measured values from four different samples.

3-10, a roughly exponential dependence was obtained, even though the error bars were comparatively large probably due to the inhomogeneity of the sample-to-sample quality of the CVD-grown SLGs. When we use the following equation, $\frac{V_{ISHE}}{g_r^{\uparrow\downarrow}} = A \cdot \exp(-\frac{d}{\lambda})$, the spin diffusion length is estimated to be 2.2 μm, which is comparable to the value estimated in this study.

3.2.8 Reproducible experiment

A new sample (sample 3) was also investigated by spin pumping method and ISHE. The structure is shown in Fig. 3-11. A Py film and a Pd wire were evaporated onto the SLG layer with a SiO_2 substrate by the EB lithography and the EB evaporation method. The external magnetic field and magnetization direction are denoted by the blue and red arrows. θ_H and θ_M are the angles between the arrows and the SLG plane. The angular dependence of magnetization was further investigated. Figure 3-12 shows the FMR spectra dI(H)/dH measured for pure Py film with and without the SLG/Pd. I donates the microwave absorption intensity. The line width W of the spectrum for Py film is clearly enhanced when Py film has SLG attached Since the spectral width W is proportional to the Gilbert damping constant α, this modulation of α demonstrates the emission of a spin current into the SLG layer.

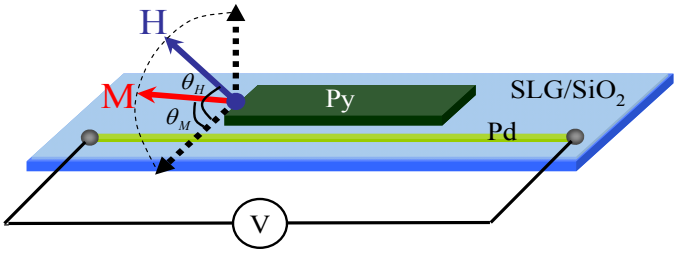

Figure 3-11. A schematic illustration of Py/SLG/Pd.

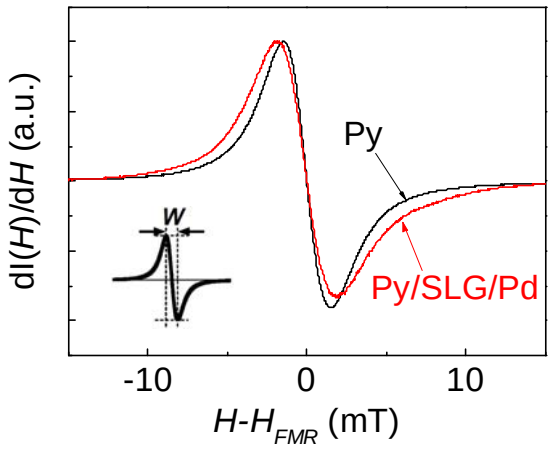

Figure 3-12. The black and red solid lines are the FMR spectrum of the Py on the SiO_2 substrate and the Py/SLG/Pd on the SiO_2 substrate, respectively.

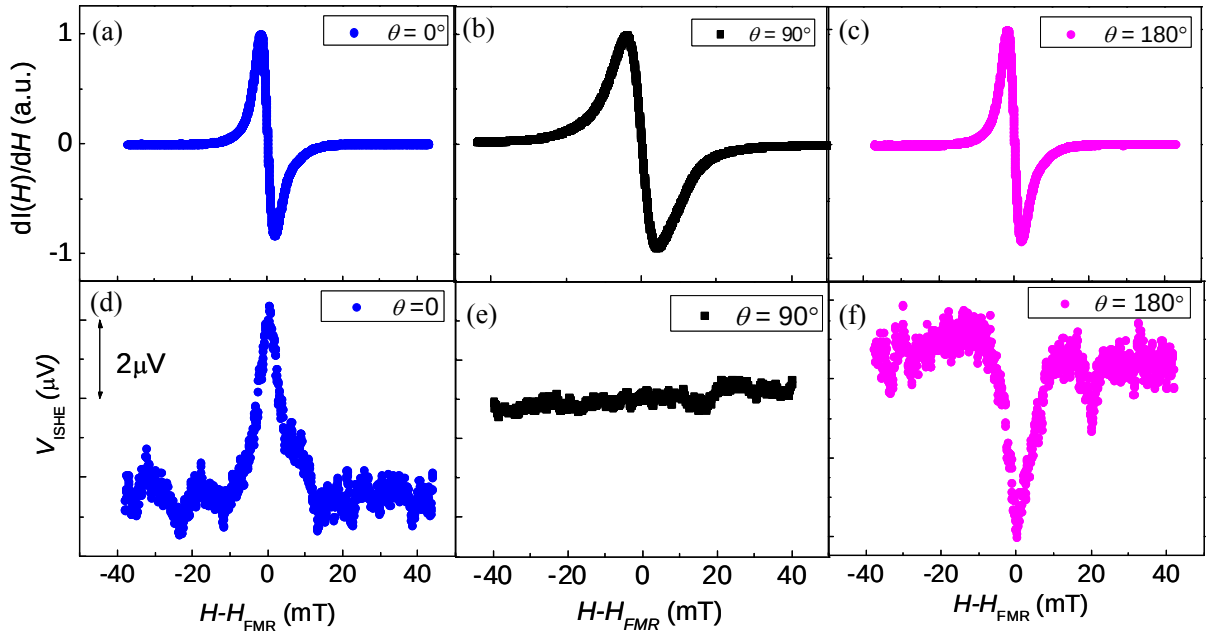

Figure 3-13. Results on spin pumping from Py layer and ISHE signal in Pd wire.

Figures 3-13 (a)-(c) show the FMR signals as functions of θ_H, where the FMR of the Py occurs under all conditions. The results reproduce the angular dependence of ISHE signals of sample 1 as shown in Fig 3-3. The contribution of ISHE was estimated to be 4.80×10^{-6} V by fitting the data to Eq.3-2. The spin diffusion length of this sample was estimated to be 1.8 μm at room temperature by the same calculation procedures used in the results for sample 1. This result perfectly reproduced the observed data in sample 1 and 2.

Figure 3-14 shows a typical FET

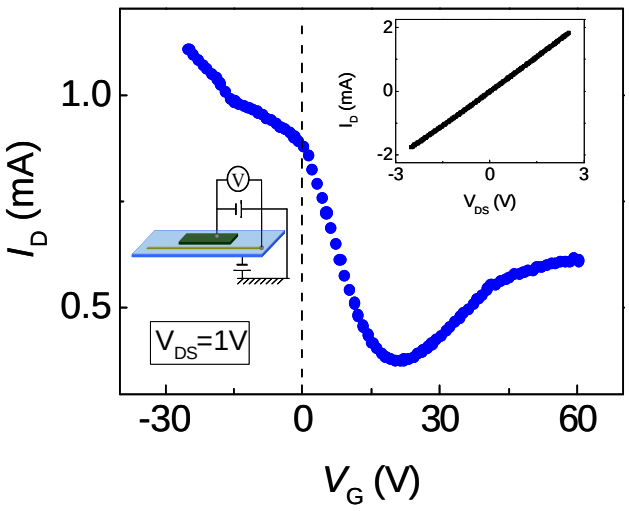

Figure 3-14. An FET characteristic of the sample. The right inset shows a linear I-V curve under the zero gate voltage application. The left inset shows an illustration of the FET characteristic measurement setup under the bias voltage of 1 V.

behavior from SLG. The field effect mobilty of SLG is estimated to be ca. 5600 $cm^2/V{\cdot}s$, although a slight distortion in the gate voltage dependence was observed. The distortion often appears in ferromagnetic contacts; it is ascribable to metal/graphene contact state, which was reported in other studies, although a complete understanding of the phenomenon has not been obtained yet. The inset shows the current-voltage (*I-V*) characteristic measured for Py/SLG/Pd sample. The two electrodes are attached to the Py layer and Pd wire. The *I-V* characteristic shows a clearly linear behavior, which indicates an Ohmic contact between the Py/SLG interface.

3.2.9 An investigation towards the estimation of spin precession in SLG

To further clarify spin relaxation in SLG by the spin pumping method, we investigated the angular dependence of the magnetization precession. When an oblique external magnetic field H was applied to the Py film plane, the magnetization precession direction θ_M was not parallel to H, because of the demagnetization field in the Py film. The static equilibrium condition yields the following expression [2], which relates θ_H and θ_M (see Fig. 3-15):

$$\left(\frac{H}{4\pi M_s}\right)\sin\left(\theta_H - \theta_M\right) = \sin\theta_M \cos\theta_M, \quad (3\text{-}5)$$

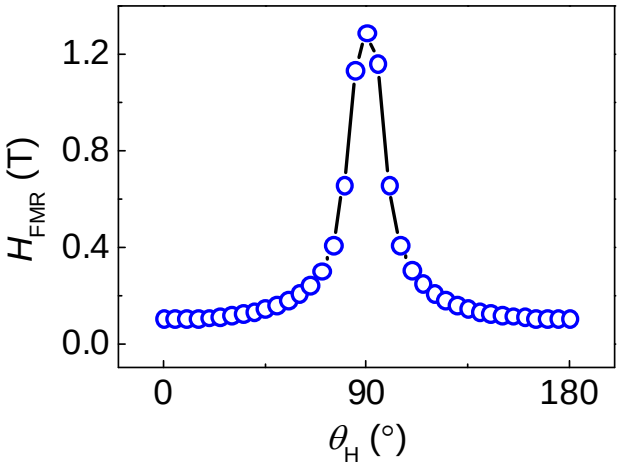

Figure 3-15. θ_H dependence of the ferromagnetic resonance field, H_{FMR}. Every θ_M that is related to every certain θ_H can be observed by the static equilibrium condition.

where H is the strength of the external magnetic field. Figures 3-16 show the dependence of θ_M on θ_H, obtained by using Eq. (3-5). The θ_H dependence of the electromotive force normalized by the value at $\theta_H = 0$ is shown in

more detail Fig. 3-17. A clear angular dependence of V was observed. The spin momentum scattering time can be calculated by using the equation of conductivity $\sigma = \frac{e^2}{h} k_F v_F \tau_p$, and k_F is given by $k_F = \sqrt{\frac{4\pi n}{g_s g_v}}$ [9], where g_s and g_v are the 2-fold valley and spin degeneracies, respectively, h is Planck's constant, e is the electron charge, and k_F and v_F are the Fermi wave vector and Fermi velocity of graphene. The spin momentum scattering time τ_p in this study was calculated as 45 fs by Boltzmann transport theory [10] at zero-bias voltage. For the case of spin relaxation time, the diffusion constant is expressed by $D = \frac{1}{2} v_F^2 \tau_p$, so the diffusion constant of graphene in this study is 0.0225 $m^2 s^{-1}$; as a result, the spin relaxation time in this study is estimated to be 144 ps by using $\tau_s = \lambda^2 / D$. The spin precession time is between the value of spin relaxation time and the spin momentum time in this study, i.e., a combination of spin relaxation and the spin momentum scattering process. The applied microwave might also influence the spin relaxation process in SLG. The experimental demonstration of real spin relaxation time by spin pumping method needs further investigation.

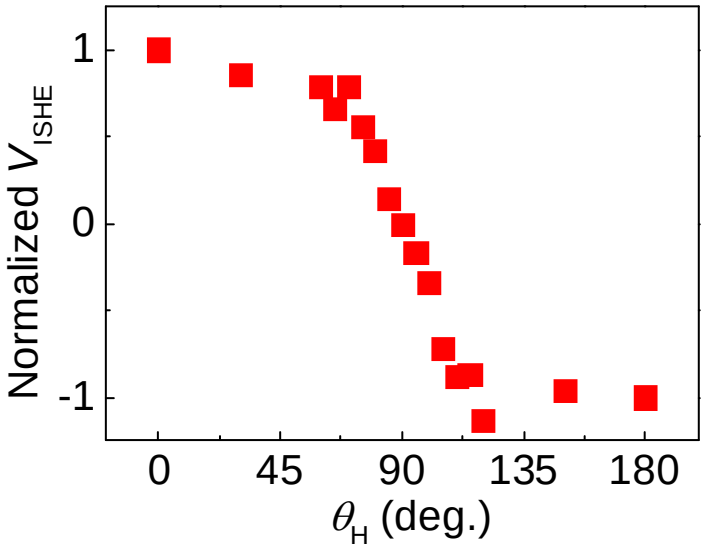

Figure 3-17. External magnetic field dependence of normalized electromotive force. The squares are the experimental data.

3.3 Conclusion

In summary, I successfully demonstrated the dynamical spin injection, resulting in generation of spin current in SLG at room temperature, which enables generation of a pure spin current free from electrical conductance mismatch. The spin coherence length of CVD-grown SLG was 1.36 μm, which is comparable with previous reports on spin coherence length of CVD-grown SLG. This provides a novel platform for discussing spin transport physics in SLG from a new viewpoint.

References

[1] C. M. Orofeo, H. Hibino, K. Kawahara, Y. Ogawa, M. Tsuji, K. Ikeda, S. Mizuno, and H. Ago, Carbon **50**, 2189 (2012).

[2] J. Foros, G. Woltersdorf, B. Heinrich, and A. Brataas, J. Appl. Phys. **97**, 10A714 (2005).

[3] K. Ando and E. Saitoh, J. Appl. Phys. **108**, 113925 (2010).

[4] E. Saitoh, M. Ueda, H. Miyajima, and G. Tatara, Appl. Phys. Lett. **88**, 182509 (2006).

[5] A. Avsar, T.-Y. Yang, S. Bae, J. Balakrishnan, F. Volmer, M. Jaiswal, Z. Yi, S.R. Ali, G. Guentherodt, B. H. Hong, B. Beschoten, and B. Ozyilmaz, Nano Lett. **11**, 2363 (2011).

[6] E. Shikoh, K. Ando, K. Kubo, E. Saitoh, T. Shinjo, and M. Shiraishi, Phys. Rev. Lett. **110**, 127201 (2013).

[7] A. Tsukahara, Y. Ando, E. Shikoh, M. P. Delmo, T. Shinjo, and M. Shiraishi, arXiv:1301.3580.

[8] R. Nouchi, M. Shiraishi, and Y. Suzuki, Appl. Phys. Lett. **93**, 152104 (2008).

[9] K. V. Emtsev, F. Speck, T. Seyller, L. Ley and J. D. Riley, Phys. Rev. B, **77** (15), 155303 (2008).

[10] E. H. Hwang, S. Adam,S. and Das Sarma, Phys. Rev. Lett. **98**, 186806 (2007).

Chapter 4

Temperature dependence of the spin Hall angle of palladium*

Abstract

In this section, the temperature dependence of the spin Hall angle of palladium (Pd) was experimentally investigated by spin pumping. A $Ni_{80}Fe_{20}$/Pd bilayer thin film was prepared, and a pure spin current was dynamically injected into the Pd layer. This caused the conversion of the spin current to a charge current owing to the inverse spin Hall effect. It was found that the spin Hall angle varies as a function of temperature, whereby the value of the spin Hall angle increases up to ca. 0.02 at 123 K.

---

*Published as: Z. Tang, Y. Kitamura, Y. Ando, T. Shinjo and M. Shiraishi,

Appl. Phys. Express 6 083001 (2013).

4.1 Experimental details

Figure 4-1 shows the schematic illustration of a $Ni_{80}Fe_{20}$(Py)/Pd bilayer sample. A 25-nm-thick permalloy(Py) film and a 5-nm-thick Pd film were prepared on an oxidized silicon substrate by electron beam evaporation. Both Py and Pd layers were rectangular, with an area of 2 × 1 mm^2. The Pd layer was connected to the positive and negative ends of a nano-voltmeter as shown in Fig. 4-1(a). Spins from the ferromagnetic Py were injected into the Pd layer by the dynamical spin injection method. The sample system was placed at the center of a TE_{011} microwave cavity in an ESR (JEOL) instrument with a frequency (f) of 9.12 GHz. An external magnetic field H was applied to the Py/Pd bilayer at an angle of θ_H, as shown in Fig. 4-1.

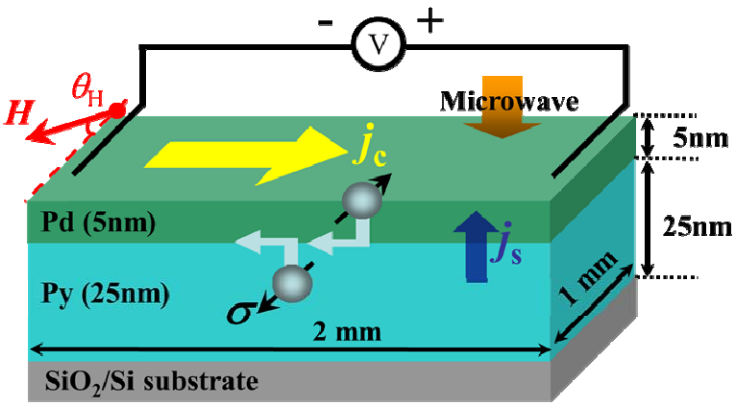

Figure 4-1. Schematic illustration of the Py/Pd bilayer sample used in this study. H represents an external magnetic field and θ_H the angle of the external magnetic field. The dimensions of the sample are shown in the figure.

4.2 Results and discussions

4.2.1 Observation of FMR signals

The ferromagnetic resonance (FMR) condition was determined using the following equation [1, 2]:

$$(\frac{\omega}{\gamma})^2 = H_{FMR}(H_{FMR} + 4\pi M_s), \quad (4\text{-}1)$$

where $\omega = 2\pi f$, γ, H_{FMR}, and M_s are the gyro-magnetic ratio of the ferromagnet, the FMR field, and the saturation magnetization of Py, respectively. Figure 4-2 shows the FMR spectra of Py with and without Pd. The line width of the spectrum corresponding to Py/Pd is larger than that corresponding to Py alone, which is attributed to the modulation of the Gilbert damping constant (α) owing to successful spin pumping into the Pd layer.

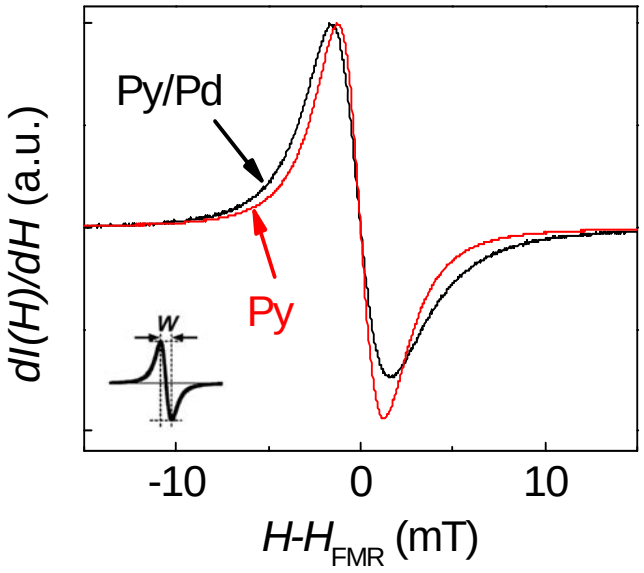

Figure 4-2. FMR spectra of the Py layer (red line) and the Py/Pd layer on the SiO_2 substrate (black line). An increase in the line width can be observed, which is attributed to modulation of the Gilbert damping constant α, indicating successful spin injection into the Pd layer by spin pumping.

4.2.2 Inverse spin Hall effect

The FMR spectra and output dc voltages of the Py/Pd bilayer at RT resulting from the ISHE in the Pd are shown in Figs. 4-3 (a) and (b), respectively. The FMR intensities and resonance fields were nearly identical for all values of θ_H, and an electromotive force was induced when θ_H was set to 0° and 180°, while the signal was

flat at θ_H = 90°. Because this is consistent with the symmetry of the ISHE ($J_c \propto J_s \times \sigma$), the observed electromotive force was ascribed to the ISHE of Pd, which was due to a pure spin current generated dynamically by spin pumping at the Py/Pd interface. A theoretical fitting was then performed, in order to separate the ISHE and anomalous Hall effect (AHE) signals by using the following equation [3]:

$$V = V_{ISHE}\frac{\Gamma^2}{(H-H_{FMR})^2+\Gamma^2} + V_{AHE}\frac{-2\Gamma(H-H_{FMR})}{(H-H_{FMR})^2+\Gamma^2} + aH + b, \qquad (4\text{-}2)$$

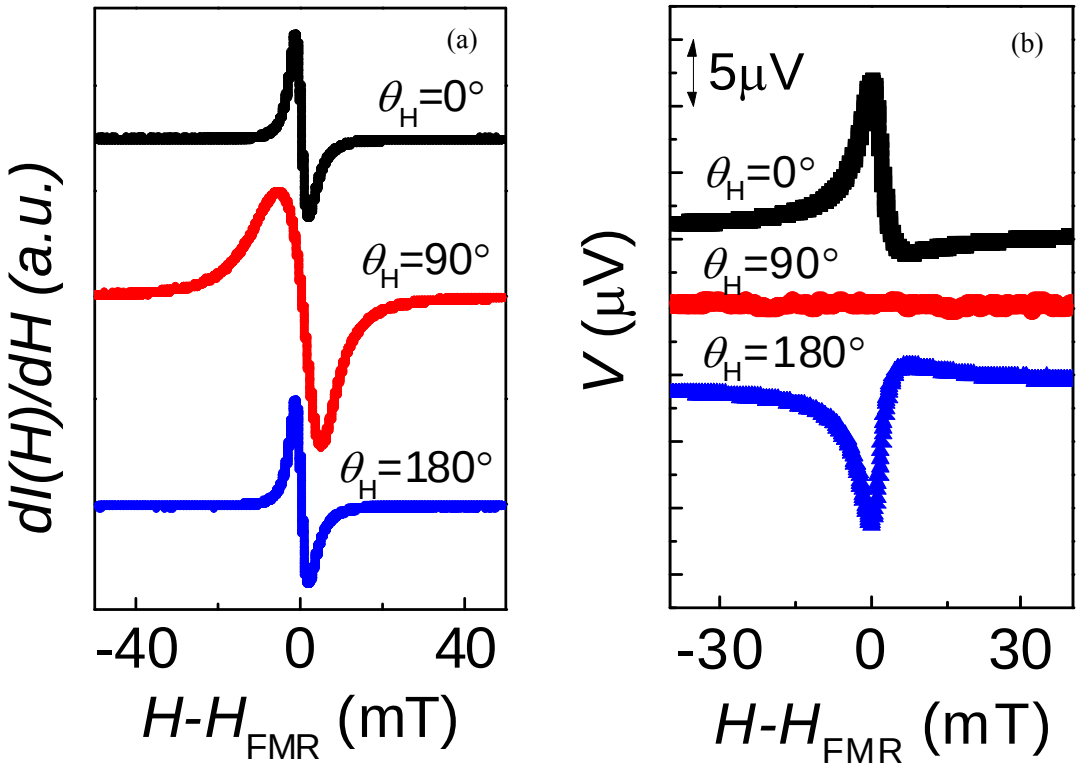

Figure 4-3. (a) Magnetic field angle (θ_H) dependence of the FMR signal *dI(H)/dH* for the Py/Pd bilayer sample. (b) Magnetic field angle (θ_H) dependence of the electromotive force measured from the Py/Pd bilayer sample.

where V_{ISHE} is the electromotive force owing to the ISHE, V_{AHE} is the output voltage resulting from the AHE, and H is the external static magnetic field. The value of H_{FMR} was experimentally determined to be 89.51mT at 0° and 180° at RT. The variables Γ, a, and b are the fitting parameters. As shown in Fig. 4-4, a theoretical fitting using Eq. (4-2) effectively reproduced the experimental results, and V_{ISHE} was estimated to be 7.66 μV at RT.

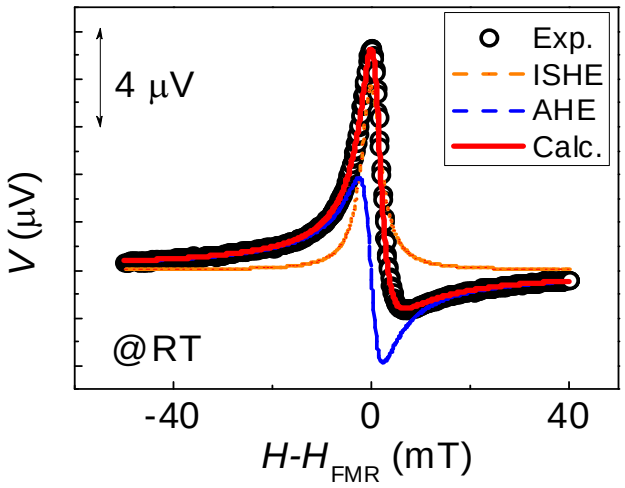

Figure 4-4. Magnetic field dependence of the V_{ISHE} for the Py/Pd bilayer film at 200mW and RT.

4.2.3 Calculation of spin Hall angle of Pd at RT

A pure spin current was injected at the Py/Pd interface via spin pumping under the resonance condition, and the generated spins diffused into the Pd layer were converted to a charge current (j_c), as shown in Fig. 4-1(a). The spin current density j_s was theoretically calculated as [4],

$j_s = \frac{g_r^{\uparrow\downarrow}\gamma^2 h^2 \hbar[4\pi M_s\gamma + \sqrt{(4\pi M_s)^2\gamma^2 + 4\omega^2}]}{8\pi\alpha^2[(4\pi M_s)^2\gamma^2 + 4\omega^2]}$, where h is the microwave magnetic field. It was set to 0.16 mT at a microwave power of 200 mW; $g_r^{\uparrow\downarrow}$ is given by $g_r^{\uparrow\downarrow} = \frac{2\sqrt{3}\pi M_s\gamma d_{Py}}{g\mu_B\omega}(W_{Py/Pd} - W_{Py})$, where g, μ_B, d_{Py}, $W_{Py/Pd}$, and W_{Py} are the g-factor, Bohr magneton, thickness of the Py layer, FMR spectral width of the Py/Pd film, and FMR spectral width of the Py film, respectively. In this study, d_{Py}, $W_{Py/Pd}$, and W_{Py} were 25 nm, 3.03mT, and 2.49mT, respectively. The electromotive force due to the ISHE can then be expressed in the simplest form as follows [4]:

$$V_{ISHE} = \frac{w\theta_{SHE}\lambda_{Pd}\tanh(d_{Pd}/2\lambda_{Pd})}{d_{Py}\sigma_{Py} + d_{Pd}\sigma_{Pd}}\left(\frac{2e}{\hbar}\right)j_s, \qquad (4\text{-}3)$$

where w is the length of the Py layer defined as in Fig. 4-1(a), d_{Py} and σ_{Py} are the thickness (25 nm) and electric conductivity ($4.48\times 10^6\,\Omega^{-1}\,m^{-1}$) of the Py layer at RT, respectively, and d_{Pd} and σ_{Pd} are the thickness (5nm) and electric conductivity ($3.50\times 10^6\,\Omega^{-1}\,m^{-1}$) of the Pd layer, respectively. From the above calculations, the spin Hall angle θ_{SHE} was estimated to be 0.011 at RT, which is reasonably consistent with the results obtained in a previous study [5].

4.2.4 Power dependence of V_{ISHE} at RT

Figure 4-5 shows the microwave power dependence of the electromotive force from the Pd of the Py/Pd sample. The electromotive force from the Pd layer V_{ISHE} was proportional to the microwave power. As shown in the inset of Fig. 4-5, the power dependence of V_{ISHE} was in good agreement with the theoretical prediction [6], indicating that the generation of the observed electromotive force can be attributed to the ISHE in Pd. More importantly, the unsaturated FMR spectra enabled the estimation of the spin Hall angle of Pd. Therefore, the results about the spin Hall angle that was discussed in section 4.3.3, are reliable under the power of 200mW with an unsaturated magnetization. .

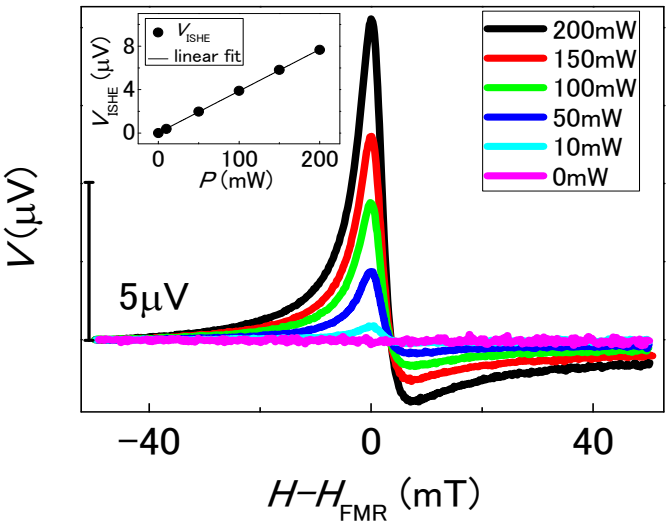

Figure 4-5. Microwave power dependence of the electromotive force in the Pd film. A magnetic field was applied parallel to the film plane (θ_H =0°). The output voltage increased with increasing microwave power. The inset shows the power dependence of the V_{ISHE}.

4.2.5 Temperature dependence of spin Hall angle of Pd

To estimate the spin Hall angle at various temperatures, the temperature evolution of the linewidth (W) of a simple Py film, resonance field (H_{FMR}) and saturation magnetization ($4\pi M_s$) were measured and evaluated (see Fig. 4-6), and the results were physically reasonable. Note that σ_{Py}, σ_{Pd}, V_{ISHE}, and λ_{Pd} changed with the temperature, and thus, the temperature dependence of σ_{Py} and σ_{Pd} was also evaluated (see Fig. 4-7(a)); the estimated values of V_{ISHE}

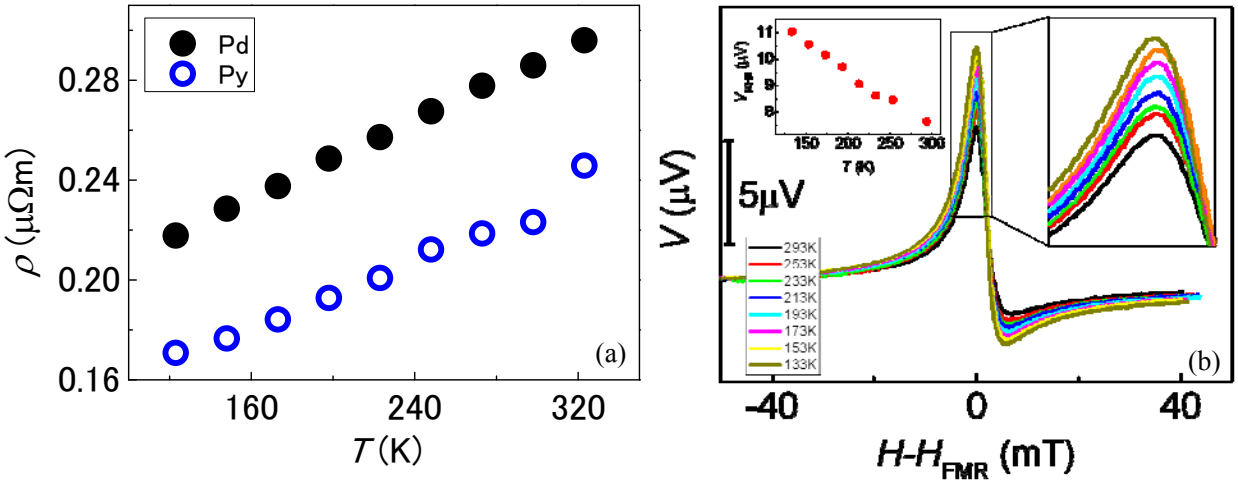

Figure 4-7. (a). Temperature dependence of the resistivity of the Pd and Py layers. Red and blue circles indicate the experimental data for Pd and Py, respectively. The red and blue lines show the linear fittings. (b) Temperature dependence of the resistivity of the Pd and Py layers. Red and blue circles indicate the experimental data for Pd and Py, respectively. Red and blue lines show the linear fittings.

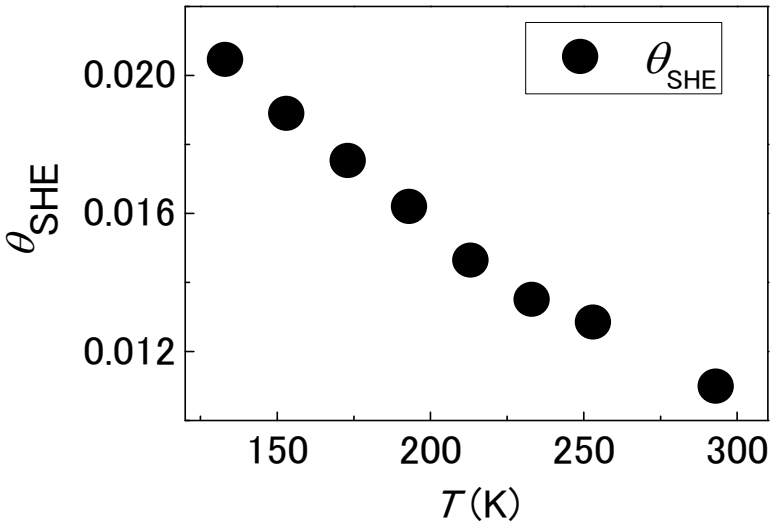

Figure 4-8. Temperature dependence of the spin Hall angle θ_{SHE} of Pd. The spin Hall angle decreased with an increase in the temperature.

obtained from Eq. (4-2) at different temperatures are shown in the inset of Fig. 4-3(c). The spin diffusion length of Pd, denoted as λ_{Pd}, has been reported to be 9nm at RT and 25nm at 4.2K [7, 8]; as a result, λ_{Pd} can be estimated at each temperature by interpolating the values at RT and at 4.2 K (in fact, λ_{Pd} is estimated to be 9.12 nm at 133 K by our calculation). Here, we assumed that the spin lifetime is inversely proportional to temperature [8]. The change of λ_{Pd} yields little contribution to the change of θ_{SHE}. Thus, θ_{SHE} of Pd can be estimated by solving Eq. (4-3) and using the conductivities of Pd and Py and the estimated spin diffusion length of Pd at each temperature. The results of this evaluation are shown in Fig. 4-8. It was found that θ_{SHE} increased up to 0.020 monotonically as the temperature decreased to 130 K.

4.2.6 Spin Hall angle of Platinum

I also measured temperature dependence of the spin Hall angle of Platinum (Pt), which is a similar material with Pd of sample group in the periodic table. The result is shown in Fig. 4-9. On the contrary, the spin Hall

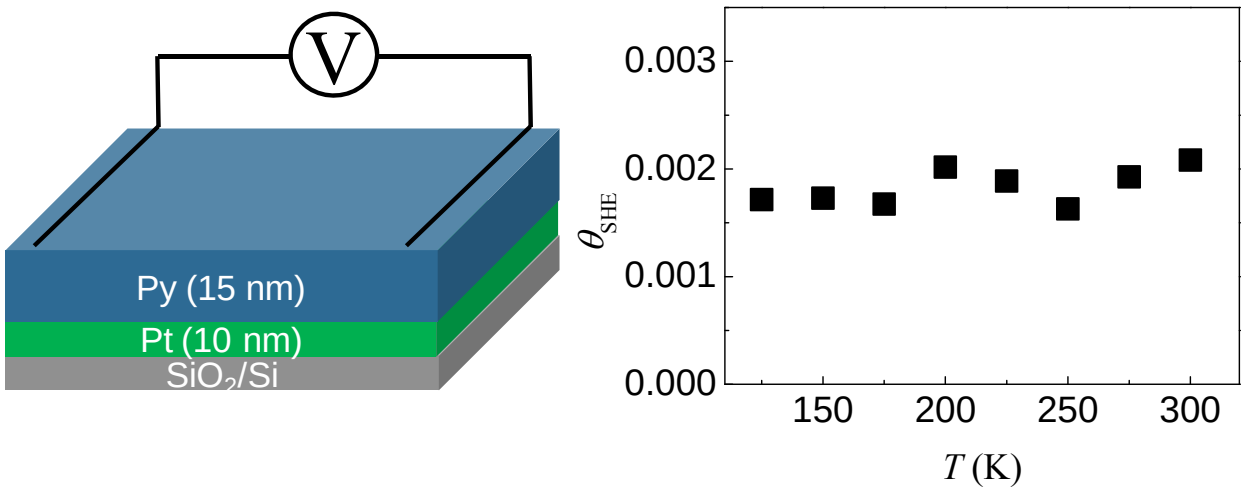

Figure 4-9 Schematic view of Py/Pt sample structure and the temperature dependence of spin Hall angle of Pt.

angle of Pt is almost independent of temperature. This result is in consistent with the result in previous reports [9, 10]. The reason of this discrepancy between Pd and Pt are discussed in section 4.2.6.

4.2.6 Discussion

Surprisingly the temperature evolution of θ_{SHE} of Pd exhibits the opposite behavior of that of Pt [9, 10]. Whereas Pt and Pd belong to the same group in the periodic table, the electron configurations are different, which may cause this difference. In fact, the electron configuration of the d-orbital allows for different signs of θ_{SHE} [11]. The origin of this characteristic temperature dependence of θ_{SHE} of Pd is out of the scope of this study, but will be investigated in the near future. It is interesting that Pt and Pd belong to the same group in the periodic table and are expected to exhibit similar ISHE, but display different temperature dependence of the spin Hall angle in experiments. It was reported that the spin Hall angle of Pt decreases with the decreasing temperature, while in the case of Pd, it increases with the increasing temperature. The electron configurations of Pt and Pd are different, i.e., [Xe] $4f^{14}$ $5d^{9}$ $6s^{1}$ for Pt and [Kr] $4d^{10}$ for Pd. Such difference in the configurations (especially f and d orbital) may induce the different temperature dependence of the spin Hall angle, although precise understanding has not been obtained yet. In fact, the difference of the electron configurations of d-orbitals enables a polarity change of the spin Hall angle as reported by M. Morota et al [21], and we deduce the difference of the electron configuration in Pt and Pd may have induced the unexpected result in this study.

4.3 Conclusion

In this study, the temperature dependence of the spin Hall angle of Pd was quantitively estimated by spin pumping. It was found that θ_{SHE} increased up to 0.020 monotonically as the temperature decreased to 130 K. This approach enables quantitative estimation of the temperature dependence of spin transport properties of Si, graphene, and other materials by combining spin pumping and the ISHE.

References

[1] K. Ando, Y. Kajiwara, S. Takahashi, S. Maekawa, K. Takemoto, M. Takatsu, and E. Saitoh, Phys. Rev. B **78,** 014413 (2008).

[2] C. Kittel, Introduction to Solid State Physics, (Wiley, New York, 2005) 8th ed.

[3] E. Saitoh, M. Ueda, H. Miyajima, and G. Tatara: Appl. Phys. Lett. **88,** (2006) 182509.

[4] K. Ando, S. Takahashi, J. Ieda, Y. Kajiwara, H. Nakayama, T. Yoshino, K. Harii, Y. Fujikawa, M. Matsuo, S. Maekawa, and E. Saitoh, J. Appl. Phys. **109,** 103913 (2011).

[5] K. Ando and E. Saitoh, J. Appl. Phys. **108**, 114925 (2010).

[6] Y. Tserkovnyak and A. Brataas, Phys. Rev. Lett. **88** 117601 (2002).

[7] J. Foros, G. Woltersdorf, B. Heinrich and A. Brataas, J. Appl. Phys. **97,** 10A714 (2005).

[8] H. Kurt, R. Loloee, K. Eid, W. P. Pratt, and J. Bass: Appl. Phys. Lett. **81,** 4787 (2002).

[9] L. Liu, R. A. Buhrman and D. C. Ralph, *arXiv*:1111.3702v3.

[10] L. Vila, T. Kimura and Y. Otani, Phys. Rev. Lett. **99,** 226604 (2007).

[11] G.Y. Guo, S. Murakami, T.-W. Chen and N. Nagaosa, Phys. Rev. Lett. **100** 096401 (2008).

[12] M. Morota, Y. Niimi, K. Ohnishi, D. H. Wei, T. Tanaka, H. Kontani, T. Kimura, and Y. Otani, Phys. Rev. B **83** 174405 (2011).

Chapter 5

Temperature dependence of spin coherence in single-layer graphene

Abstract

Graphene is known as an attractive material for spintronics. The spin coherence in single-layer graphene (SLG) was investigated by the dynamical spin injection method at room temperature in Chapter 3. In this section, the temperature dependence of the spin coherence in single-layer graphene is experimentally investigated by the dynamical spin injection method. A $Ni_{80}Fe_{20}$/Pd bilayer thin film was prepared on CVD-grown SLG, and a pure spin current was dynamically injected into the SLG layer. Spin detection was accomplished by the conversion of the spin current to a charge current in palladium owing to the inverse spin Hall effect. It was found that the spin coherence in SLG is temperature independent. This result is consistent with the results obtained using electrical methods.

5.1 Experimental details

In this study, the sample fabrication process is the same with that were described in Chapter 3. Large size single-layer graphene was fabricated by the CVD method. The samples were grown by the EB evaporation technique with a base pressure of 5×10^{-6} Pa. The patterns of Py and Pd are made onto the SLG layer by EB lithography system. The precise size of the Py and Pd are measured with an atomic force microscope. The gap between Py and Pd is 717.77 nm, and the thicknesses of Pd and Py are 7.5 nm and 31.3 nm, respectively. The measurements are carried out with an ESR equipment (JEOL, JES-FA Series ESR) and the frequency of the microwave is 9.12 GHz. Temperature is controlled from 130 K to room temperature by using liquid nitrogen.

5.2 Results and discussion

5.2.1 Temperature dependence of resonance point

In this section, the temperature dependence of all the measurements discussed in Chapter 3 is carried out. First, we investigated the temperature dependence of the ferromagnetic resonance field as shown in Fig. 5-1. It was found that it decreased with the decreasing temperature. The saturation magnetization is inversely correlated with the ferromagnetic resonance field, due to the resonance

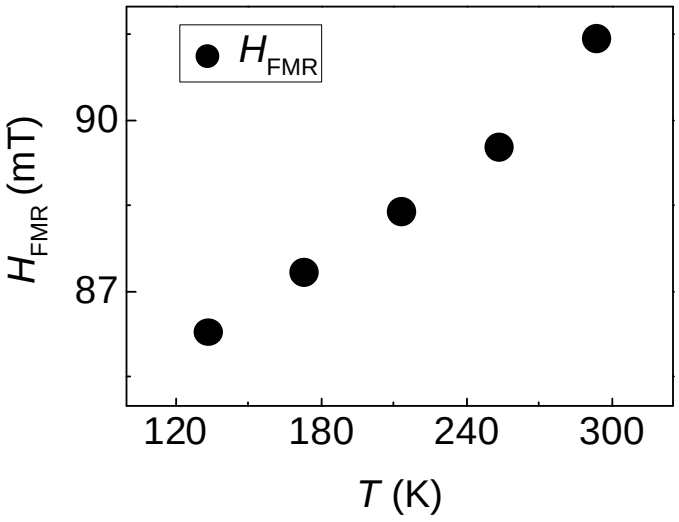

Figure 5-1 Temperature dependence of ferromagnetic resonance field. The decrease of saturation magnetization induces the increase of the ferromagnetic resonance field due to the resonance condition.

condition $\left(\frac{\omega}{\gamma}\right)^2 = H_{FMR}(H_{FMR}+4\pi M_s)$. This is natural, because the saturation magnetization increases with the decreasing temperature, and the thermal disturbance is suppressed at low temperature. This means the saturation magnetization becomes larger at lower temperatures, and it will decrease to zero when the temperature increases to Curie temperature, at which the ferromagnetic material will lose ferromagnetism.

5.2.2 Temperature dependence of other parameters

To observe the other temperature dependence parameters, we carefully measured the temperature dependence of the linewidth of only the Py (W_F) and Py/SLG ($W_{F/N}$) samples. The temperature dependence of

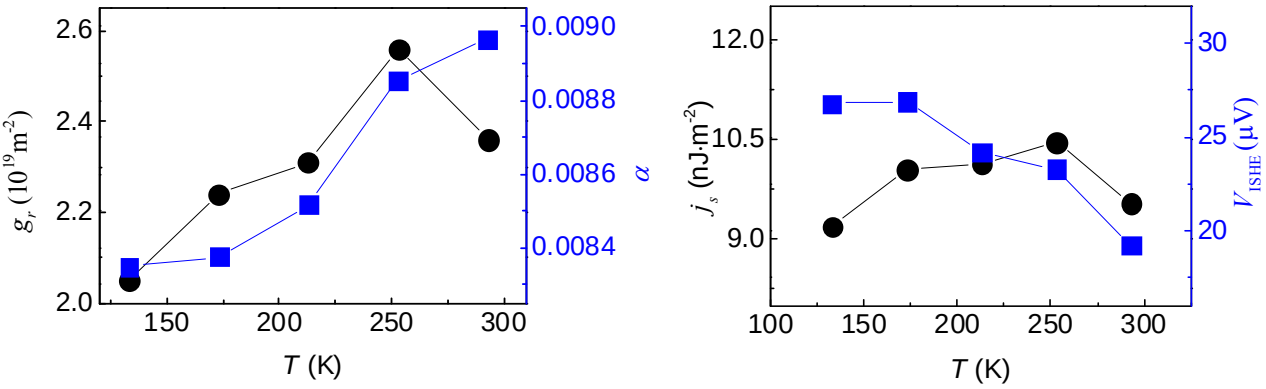

Figure 5-2 (a) Temperature dependence of the real part of mixing conductance and damping constant. (b) Temperature dependence of the spin current density and the calculated output voltage, which was generated from the spin current density without spin dissipation to an output voltage.

the real part of the mixing conductance and the damping constant are shown in Fig. 5-2(a). The mixing conductance slightly changed with temperature, due to the change in saturation magnetization. The damping constant is proportional to the linewidth of the ferromagnetic resonance signal, so it decreases with decreasing temperature. Figure 5-2(b) shows the temperature dependence of spin current density and the calculated output ISHE voltage, which are estimated by Eqs. (3-2) and (3-3) [1], respectively. Then, we compare the output voltage between the measured electromotive force in the Pd wire and the calculated output voltage, by using the

generated spin current density without any spin dissipation in the SLG layer.

5.2.3 Temperature dependence of spin coherence in SLG

Figure 5-3(a) shows the comparison between theoretically calculated and experimentally observed output voltage. The dissipation between the values of the output voltage is due to the exponential decay of spin transport in SLG. Therefore the spin coherence obeys the exponential relation $\frac{V_{exp}}{V_{cal}}=\exp(-\frac{d}{\lambda})$. The final temperature dependence of spin coherence is shown in Fig. 5-3(b). The spin diffusion length is weakly dependent on temperature, i.e., it slightly decreases with increasing temperature, a fact which may be linked to electron-phonon scattering in the SLG/SiO_2 substrate. This result is consistent with previous reports that used the electrical method [2], but further investigations are needed for obtaining more details about the spin relaxation mechanisms in SLG.

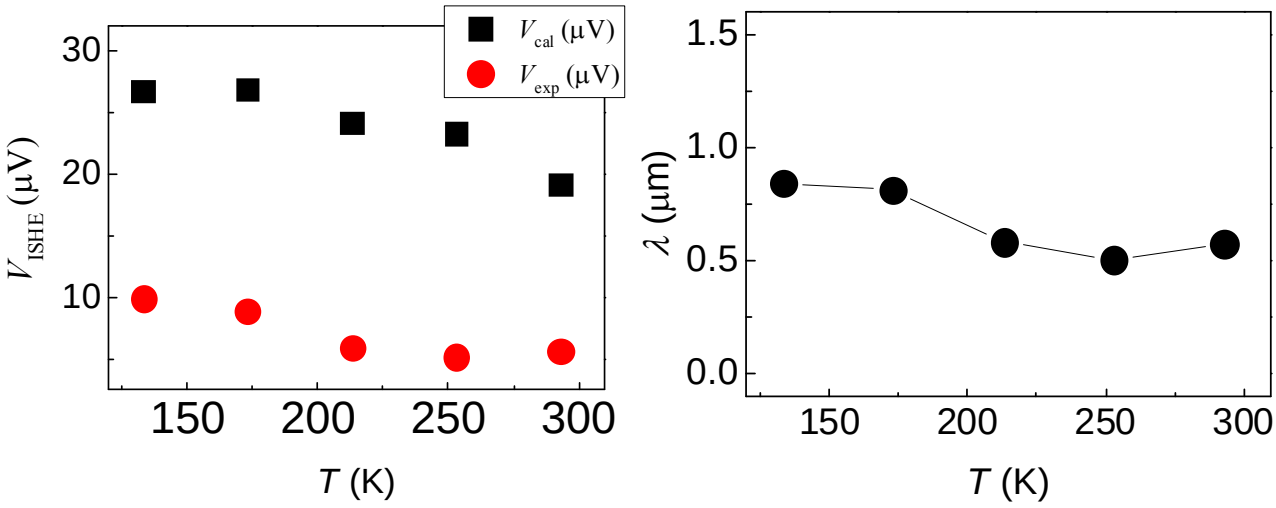

Figure 5-3. (a) The calculated output electromotive force without spin dissipation in SLG and the observed output voltage measured in Pd wire. The difference between these values is due to the decay of spin transport in SLG. (b) The temperature dependence of spin coherence in SLG. The spin diffusion length is very weakly dependent on temperature for SLG.

5.3 Conclusion

In this chapter, I investigated the temperature dependence of spin coherence of SLG by magnetization dynamics. The spin coherence of SLG is almost independent of temperature in spin pumping method, i.e., it slightly decreases with increasing temperature. This may be due to weak electron-phonon scattering in the SLG/SiO_2 substrate. This result is consistent with the previous reports using the electrical method [8], and further investigation is needed for a better understanding of spin relaxation mechanisms in SLG.

References

[1] K. Ando, S. Takahashi, J. Ieda, Y. Kajiwara, H. Nakayama, T. Yoshino, K. Harii, Y. Fujikawa, M. Matsuo, S. Maekawa, E. Saitoh, J. Appl. Phys. **109**, 103913. (2011).

[2] A. Avsar, T.-Y. Yang, S. Bae, J. Balakrishnan, F. Volmer, M. Jaiswal, Z. Yi, S.R. Ali, G. Guentherodt, B. H. Hong, B. Beschoten, B. Ozyilmaz, Nano Lett. **11**, 2363 (2011).

Chapter 6

General conclusion

Firstly, I briefly introduced the history of spintronics. The band structure of graphene was also presented. Next, recent progress in graphene spintronics is reviewed. Finally, I pointed out the purpose of this study, and outline the contents of this thesis in Chapter 1. Next, I discussed the theoretical aspects of the dynamical spin injection theory and the inverse spin Hall effect on spin detection in Chapter 2. The ferromagnetic resonance condition and the applicability of existing models to my study were also discussed. In the second part of Chapter 2, I show the details of the fabrication procedures. In Chapter 3, I summarized all my study in doctoral research. I investigated spin transport in SLG by using a magnetization dynamics. The spin injection method is totally different from the electrical method. The electrical method uses the tunnel barrier to circumvent the impedance mismatch problem. However, this problem can be easily solved with dynamical spin injection using the transfer of spin angular momentum rather than injection of spins with carriers. In this study, the spin coherence in SLG was estimated to be 1.36 μm by magnetization dynamics. The reliable results we obtained indicate that the dynamical spin injection method is largely applicable in graphene spintronics research. This study offers a new standpoint for the study of graphene spintronics. Another contribution of this thesis is the fact that it discusses the issue of temperature dependence of spin coherence in SLG. As a first step towards this investigation, the temperature dependence of the spin Hall angle of Pd is showed that it was investigated in Chapter 4. Results decreased with increasing the temperature from 0.02 at 130 K to 0.01 at 300 K. Finally, I explored the temperature dependence of spin coherence in SLG using the dynamical spin injection method. Results showed that the spin coherence of SLG is almost independent of temperature. The spin coherence of SLG slightly decreases with increasing temperature. Through these studies, I have been able to offer a new viewpoint for the investigation of spin coherence in SLG, and provide new perspectives towards more detailed investigation of spin relaxation mechanisms, which will enable for future graphene applications.

Acknowledgement

First and foremost, I would like to show my deepest gratitude to my supervisor, Prof. Shiraishi, a respectable, responsible and resourceful scholar, who has provided me with valuable guidance in not only every stage of the writing of this thesis but also all in my life and my study in Japan for five years. Five years ago, it was my first time to go abroad alone and studied in a new environment. Prof. Shiraishi gave me lots of useful advice and helped me conquer many difficulties in both my study and my life. I offer my sincere appreciation and gratitude to him for applying for funding for me, and recommending me for future work. Without his enlightening instruction, impressive kindness and patience, I could not have completed my study here and finished my thesis. The slogan in our laboratory is “The important thing is to never stop questioning”, and I found it is really the most important thing in scientific research. Our research field is quite advanced and there are sometimes no reference books for us to use, and sometimes the previous studies may not be reliable, so it is critical to doubt everything in research, to make sure of every step. This is the spirit of scientific research. On the other hand, this is also common in corporations; therefore my experience in the Shiraishi laboratory will also help me in my future life.

I shall extend my thanks to my family for all their kindness and really strong support, even though my parents may never read this part of acknowledgement in English. In China, one family has to raise only one child because of the birth policy, so it is hard for parents to send their only child abroad. Therefore, I really appreciate them for letting me (pushing me) go out to have a look at the world, to experience other cultures. It was really good for me, as a man, to broaden my view and open my vision. I thank them for their love and trust, which will be my greatest power in the future.

I also owe a debt of gratitude to Prof. Suzuki for his kind support and supervision during my master course years. I wish to express my sincere gratitude to Assoc. Prof. Shikoh and Assis. Prof. Ando for providing me with so many suggestions for my doctoral research. I faithfully wish all of them enjoy the work and private

lives.

I am also greatly indebted to Prof. Kawakami and Prof. Tada for their kind help and support. Prof. Kawakami helped me when I stayed in their laboratory for an exchange program. His supervision and his humor impressed me a lot when I was in his group in UCR. I thank Prof. Tada for his help in reviewing my thesis and defense. His helpful suggestions and discussions give me many interesting ideas for my future work and also for my future life. They have helped me directly and indirectly in my studies. Any progress that I have made is the result of their profound concern and selfless devotion.

I would also like to thank all the students and staff members in the Shiraishi laboratory. It was really wonderful for me to make progress among so many friends in my study. With their help and company, I was able to overcome the culture barrier smoothly. On the other hand, their persistence, endurance, patience, hard work, as well as their sense of humor inspired me a lot in my life in Japan. Also, I would like to thank Assoc. Prof. Ago from Kyushu University, who kindly provided me with graphene samples (quite expensive for the public but free for me) for my research, and coauthored one of my research papers.

I am inspired by and thankful to all my friends at Osaka University and all over the world. Although we are pursuing our own dreams in different fields or in different places, your encouragement and friendship in these years have helped me realize my research goals.

List of publications

⊙ Pubilication

1. Z. Tang, E. Shikoh, H. Ago, K. Kawahara, Y. Ando, T. Shinjo and M. Shiraishi

"Dynamically generated pure spin current in single-layer graphene"

Phys. Rev. B 87, 140401(R) (2013)

2. Z. Tang, Y. Kitamura, Y. Ando, T. Shinjo and M. Shiraishi

"Temperature dependence of spin Hall angle of Palladium"

Appl. Phys. Express 6 083001 (2013).

3. Z. Tang, H. Ago, E. Shikoh, Y. Ando, T. Shinjo and M. Shiraishi

"Temperature dependence of spin coherence in single-layer graphene by spin pumping method"

In preparation.

Publication not related with this thesis

4. Z. Tang, S. Tanabe, D. Hatanaka, T. Nozaki, T. Shinjo, S. Mizukami, Y. Ando, Y. Suzuki and M. Shiraishi, "Investigation of spin-dependent transport properties and spin-spin interactions in a CuPc-Co nano-composite system", Jpn. J. Appl. Phys. 49, 33002 (2010).

5. SHU Qi, ZHAO Xiao-Meng, ZHANG Yan, SHENG Peng, TANG Zhen-Yao, NI Gang, "Transition of magnetoresistance in Co/Alq3 granular film on silicon substrate", Chin. Phys. Lett. 26, 077505, (2009).

6. P. Sheng, G. Ni, J.F. Yin, Y. Zhang, Z.Y. Tang, S.M. Zhou, Q.Y. Jin, "Tunneling magnetoresistance effect in Co/TPD granular films.", J. Alloy Comp., 477 pp.32–35, (2009).

⊙ International Presentations

2012.9 International Colloquium on Magnetic Films and Surfaces (ICMFS 2012)

Spin-pumping-induced spin transport in single layer graphene

Oral presentation

2012.9 International Union of Materials Research Societies (IUMRS 2012)

Dynamically-generated pure spin current in single layer graphene

Oral presentation, Young Scientist Award

2012.7 The 2nd International Symposium on Terahertz Nanoscience (TeraNano 2012)

Dynamically-generated pure spin current in single-layer graphene

Oral presentation

2011.11 The 1st International Symposium on Terahertz Nanoscience (TeraNano 2011)

Spin-pumping in single layer graphene

Poster presentation

⊙ **Domestic Presentations**

2013.3 The Japan Society of Applied Physics (JSAP) the 60th Spring Meeting, 2013

Investigation of spin transport in single-layer graphene by using a dynamical method

Poster presentation

2012.9 JSAP the 73rd Autumn Meeting, 2013

Spin-pumping-induced spin transport in single layer graphene

Poster presentation

⊙ **Grant in aid**

Research Fellow of the Japan Society for the Promotion of Science DC1

⊙ **Awards**

2012.8 International Union of Materials Research Societies (IUMRS 2012)

Young Scientists Award